PERFORMANCE EVALUATION AND RETROFITTING OPTIONS FOR AN IMPACT DAMAGED NON-COMPOSITE STEEL GIRDER BRIDGE

by

Mohd Mezanur Rahman

Presented to the Faculty of the Graduate School of The University of Texas at Arlington in

Partial Fulfillment of the requirements for the Degree of

DOCTOR OF PHILOSOPHY

University of Texas at Arlington

December 2021

Acknowledgements

I would want to express my gratitude to God for providing me with the opportunity and patience to accomplish this challenging but rewarding path. Then, I would like to convey my heartfelt gratitude to my adviser, Dr. Nur Yazdani, for his unwavering support and advice during my Ph.D. degree. His unflinching patience, energy, and encouragement aided me in completing my research and dissertation on time. I am indebted to Dr. Shih-Ho Chao, Dr. Ashfaq Adnan, Dr. Samantha Sabatino and Dr. Juan Antonio Balderrama for serving on my dissertation committee and encouraging and supporting me throughout my studies.

I would like to express my gratitude for the Texas Department of Transportation's (TxDOT) financial support. Additionally, I'd want to express my gratitude to Walter Fisher III from TxDOT Dallas District for insightful recommendations.

I am thankful to Dr. Ali Abolmaali, Sara Ridenour, Irma Rose Dodd, Tracy Prior, Kelly R Sederavicius, Dr. Ernest Crosby, and Dr. Gautam Eapi for their administrative assistance and support throughout the research process.

I am grateful to Dr. Eyosias Beneberu for his constant assistance and direction during this journey. I would like to thank Dr. Ikram Efaz, Dr. Towfiqul Quadir, Dr. Zaid Momani, Dr. Tariq Al Jaafreh, Dr. Karzan Habeeb, Dr. Eyad Abdullah Alsuhaibani, Dr. Santosh Timilsina, Dr. Mai Aljaberi, Sean Natelli, Ahmed Al-Ateeq, Jose Levya, Prem Egade, Amy Florius, Jessica Thomas, Dr. Adam K Stien for support and advice during this tenure. I am grateful to my parents and wife (Khadiza Binte Jalal) for their sacrifices and support, without which I would be unable to continue with my PhD studies.

December 2021

Abstract

Performance Evaluation and Retrofitting Options for an Impact Damaged Non-Composite Steel Girder Bridge

Mohd Mezanur Rahman, PhD

The University of Texas at Arlington, 2021

Supervising Professor: Dr. Nur Yazdani

The Federal Highway Administration (FHWA) has rated about 32% of total bridges in US as structurally deficient or functionally obsolete. One of the most frequently encountered issues for this deficiency is the impact created by cars that exceed the posted clearance for a bridge. Impact damage leads to concrete spalling or cracking, exposed or broken reinforcement/prestressing strands, global and local buckling of the structural member or piercing through the steel girder. For Example, St. Francis Bridge (North Bound) carrying St. Francis Avenue over I-30 east of downtown Dallas was impact damaged by an eighteen-wheeler carrying a heavy-duty wrecker on 29th November 2017. A part of the wrecker punched through the steel girders and piercing the concrete deck. Moreover, given the bridge's lifespan of more than 60 years, several potholes and cracks in the concrete deck were detected. To access the current performance of the bridge Non-Destructive Evaluation (NDE) was carried out along with diagnostic load test. Ground Penetrating Radar (GPR) and Impact Echo (IE) were used on the deck as a part Non-Destructive Evaluation (NDE). GPR data revealed that the top rebars cover were at greater extent than stated in the as-built drawings. On the concrete deck, IE study indicated extensive delamination. A diagnostic load test was conducted to determine the bridge's present load carrying capacity. Additionally, diagnostic load test established the presence of non-composite action. A combination of NDE and load testing was utilized to successfully load rate the bridge's girders and deck, demonstrating that both the deck and girders were unable to carry HS-20 load.

Furthermore, a Finite Element Model (FEM) was prepared in ABAQUS CAE by incorporation similar geometry, materials, and boundary condition of St. Francis Bridge. The FE model was calibrated using NDE data and diagnostic load test data to capture the overall response of the bridge. Diverse retrofitting methods were investigated in the model to determine their efficacy. In addition, bridge member rating

was also performed to find out the effectiveness of each proposed retrofitting options. Based on TxDOT's Average Low Bid Unit Prices, a comparative cost analysis was done for these proposed retrofitting methods, and some general recommendations were given for future investigation.

Table of Contents

List of Figures

List of Tables

Chapter 1

INTRODUCTION

1.1 Background

At present, the United States has around 614,387 highway bridges. The Federal Highway Administration (FHWA) has rated almost 200,000 of them as structurally deficient or functionally obsolete. Moreover, more than one–fourth of all bridges are over 50 years old, which is the average design-life of a bridge. According to a CNN (2018) report, nearly 8% of the total bridges need urgent repair. Consequently, the increasing number of structurally or functionally antiquated bridges will require around $123 billion for repair/rehabilitation purposes and is a strain on the nation's budget (ASCE 2017).

Structural deficiencies of the bridges could be due to fire, poor design or construction, time-dependent deterioration, corrosion, or impact of vehicles. One of the common problems is the impact caused by over-height vehicles that exceed the posted clearance for a bridge. In the case of concrete bridges, impact damage includes concrete spalling or cracking, exposed or broken reinforcement/prestressing strands (Figure 1-1a) whereas in steel bridges, this damage includes global and local buckling of the structural member or piercing through the steel girder (Figure 1-1b).

(a)

(b)

Figure 1- 1 Impact damaged: (a) Concrete bridge on IH 75 South ramp to IH-75 South in Tennessee after being struck by an oversized rig (Benton 2020); (b) Steel bridge at the interchange of IH40 and 65 in Nashville after a tractor-trailer hauling a Caterpillar tanker truck struck the bridge (Alison and Buitrago 2018)

Figure 1-2 shows the total number of vehicle impacts to bridges from 2005 to 2008 in different states across the nation.

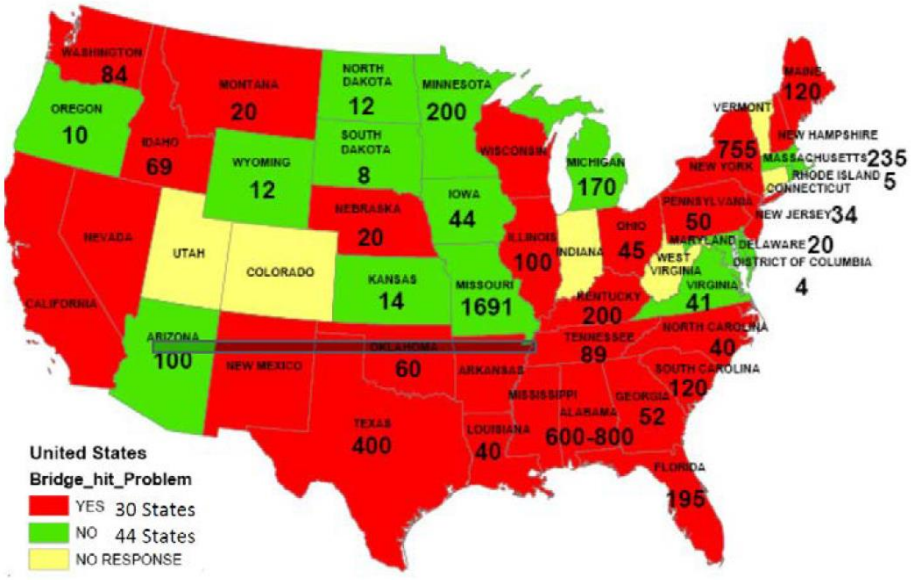

Figure 1- 2 Number of bridges hits between 2005-2008 (Agrawal et al. 2011)

The total number of bridges in Texas is 54,338, and 1.3% of the state's bridges are designated as structurally deficient (TxDOT 2018). Between 1950 and 1970, new bridges were built to develop

the interstate highway system as well as state highway expansion. After 1970, the Texas transportation network experienced rapid growth as many bridges and roads were built in metropolitan and urban areas. Table 1-1 shows the distribution and changes of Texas bridges by age grouping (reporting from the fiscal year 2008-2018). A noticeable trend is that older bridges have been replaced with new structures, and around 57% of all Texas bridges were built after 1970.

Table 1- 1 Change in number of bridges by year built, FY 2008 to FY 2018 (TxDOT 2018)

Year Built	**Number of bridges in 2008**	**Number of bridges in 2018**	**Change in the number of bridges**
Before 1950	8,900	8,017	-883
1950-1970	16,825	15,099	-1726
After 1970	24,847	31,222	6,375
Total	50,572	54,338	3,766

Though Texas has the lowest percentage of structurally deficient bridges in the nation, the state's Department of Transportation (TxDOT) spent roughly $690.5 million in the fiscal year 2018 for bridge rehabilitation, replacement, and construction bridges at new locations. The funds were distributed as follows:

- $357.8 million (52%) for replacement/rehabilitation
- $332.6 million (48%) for bridges built at new locations

As the repair/rehabilitation process is costly and causes traffic disruption and potential safety hazards, transport agencies and researchers are searching for suitable methods and materials to repair and strengthen structurally deficient bridges to minimize load restriction on the bridges (Reed et al. 2005).

Suitable repair and rehabilitation of bridge structures requires detailed condition assessments, such as non-destructive evaluation (NDE) techniques, which are efficient methods for condition assessments of bridge structures. Different NDE techniques have been previously used for bridge inspection and evaluation. For instance, Impact-echo (IE) testing (Sack et al. 1995), Ground Penetrating Radar (GPR) scanning (Hugenschmidt et al. 2006), and Infrared Thermography (Clark et al. 2003) are some of the most common non-destructive techniques for bridge evaluation.

However, these methods are only able to determine local damage and do not assess the overall performance of the bridge structure. To determine a bridge's load-carrying capacity more accurately, one efficient way is to conduct an experimental load test, a more reliable method used for load rating and evaluation of bridges (Schulz 1993).

1.2 Problem Statement

The Federal Highway Administration (FHWA) requires that each bridge be inspected every two years (FHWA 2012). Each bridge component is marked numerically from 0 to 9 based on the current condition of the component. A component rating of 4 or less is considered structurally deficient. Moore et al. (2001) conducted a study on the variability of visual inspection by different inspectors. The same bridges were inspected by 49 different inspectors. The results showed single element was rated four or five different condition ratings.

Visual inspections are considered a significant part of bridge evaluation while the non-destructive evaluation and load test provide more reliable information by presenting actual behavior of the structural elements.

So, the Dallas District Bridge Section contracted a team from the University of Texas at Arlington (UTA) to perform a non-destructive (NDE) and load test evaluation of the St. Francis Bridge. Extensive deterioration was visible on the deck of the bridge, necessitating the in-situ evaluation. Numerous cracks and potholes were observed on the bridge deck upon field visit (Figure 1-3).

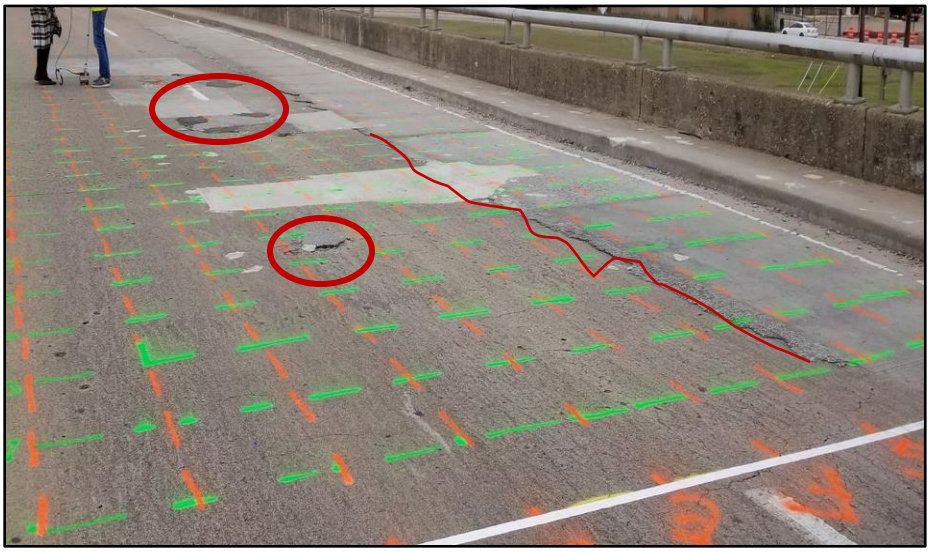

Figure 1- 3 Cracks and repaired potholes on the bridge deck

Due to the bridge's vertical clearance (less than TxDOT's (2020) minimum vertical clearance of 18.5 ft.), the bridge was impact damaged by over-height vehicles on more than one occasion. Figure 1-4 shows the pierced concrete deck by the wrecker, and Figure 1-5 shows where the wrecker punched through the steel beam .

Moreover, the damaged girder performance can be different from the undamaged girder. Hence, it is necessary to understand the overall bridge behavior so efficient and reliable repair and strengthening methods can be applied to damaged bridges in a similar condition.

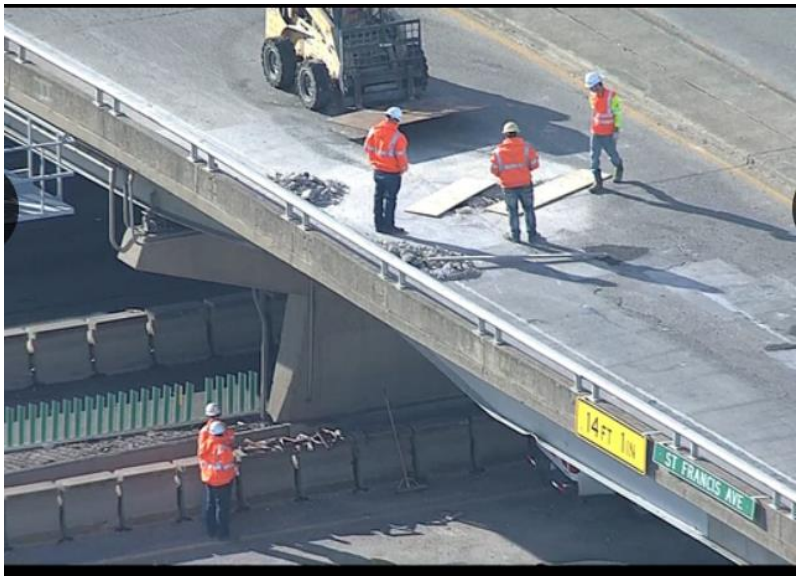

Figure 1- 4 Wrecker pierced through the concrete deck (Fox 4 News 2017)

Figure 1- 5 Wrecker punched through the steel beam (Fox 4 News 2017)

1.3 Objectives

This study focuses on load testing, nondestructive evaluation, non-composite action, load rating FEM modeling, model calibration, suitable retrofitting options, and cost analysis for repair of the St. Francis Bridge. The primary objectives of this study are as follows:

1. Evaluate the performance of an impact damaged bridge through instrumentation and static load testing.

2. Conduct a non-destructive evaluation (NDE) of the deck, using Ground Penetrating Radar (GPR) and Impact Echo (IE), to assess the stability of the deck and identify cracks and delamination.

3. Propose a distinct approach to load rate the non-composite concrete deck over steel girder bridges by incorporating NDE data in load rating procedure.

4. Calculate the unintended composite action of the concrete deck and the steel girders.

5. Understand the overall behavior of the bridge, prepare a realistic 3D finite element model detailing geometrical properties, material properties, and boundary conditions.

6. Calibrate sophisticated three-dimensional finite element models using field/experimental load test data to capture the various behavioral aspects of the bridges.

7. Investigate the possibility of increasing the flexural capacity of the bridge with different retrofitting methods and selection of the most suitable method based on cost-benefit analysis (including the reconstruction of the bridge).

1.4 Organization of the Dissertation

The thesis is broken down into nine chapters, each of which is further split into a number of subtopics. Chapters are outlined and organized as follows:

Chapter 1-Introduction

Background and motivation, problem statements, and objectives are all covered in this chapter.

Chapter 2: Literature Review

History of bridge evaluation, bridge evaluation guidelines, prior research on bridge load tests and load ratings, non-destructive evaluation, and FEM modeling and model calibration are all discussed in this section. Additionally, this part focuses on bridge retrofitting's history.

Chapter 3: Bridge Description

The St. Francis bridge's history, location, materials properties, and as-built details are all covered in this chapter.

Chapter 4: Diagnostic Load Test

In this chapter detailed instrumental plan, load testing procedure are discussed.

Chapter 5: Non-Destructive Evaluation (NDE)

In this chapter nondestructive evaluation of St. Francis bridge deck are discussed. Use of Ground penetration radar (GRP) and Impact Echo (IE) are presented herein.

Chapter 6: Finite Element Modeling

This chapter discusses modeling techniques, such as material characteristics, geometry, boundary conditions, and loading conditions. Furthermore, in this chapter, mesh sensitivity analysis and energy balance are discussed in order to gain confidence in the modeling energy balance.

Chapter 7: Result and Discussions

This chapter discusses the NDE, and load testing, findings in depth. Additionally, this chapter provides a unique method for calculating the load rating of a non-composite steel girder bridge. Furthermore, static calibration of the modeling is covered in this section.

Chapter 8: Bridge Retrofitting

Approaches for retrofitting are discussed in this chapter, including the modeling approaches used, their efficacy, and a cost comparison. Furthermore, a unique load rating procedure is discussed for load rating of bridge member after retrofitting suing ABAQUS CAE and an efficient decision tree is suggested to select the best alternative based on the temporary benefit/cost index.

Chapter 9: Conclusion and Recommendation

The results of the NDE and load testing, load rating, and FEM modeling of the retrofitting techniques are summarized at the end of this chapter. In addition, there are a few general recommendations for further study in this particular field is listed here.

Chapter 2

LITERATURE REVIEW

2.1 History of Bridge Evaluation Guidelines

The AASHTO Manuals for Bridge Maintenance Inspection (AASHTO 1970, 1974, 1978, and 1983) were designed to establish a uniform method for evaluating and rating existing bridge structures. The AASHTO Manual for Bridge Evaluation (MBE) first edition was published in 2008 and was based on the AASHTO Manuals for Bridge Maintenance Inspection. Both the 1998 AASHTO Manual for Bridge Condition Evaluation and the 2005 ASSHTO Guide Manual for Bridge Condition Evaluation and Load and Resistance Factor Rating (LRFR) of Highway Bridges were repealed by the MBE (Albrahemmi 2018).

Manual for Bridge Rating Through Load testing was introduced in 1998 by the National Cooperative Highway Research Program (NCHRP). The manual explains the significance of nondestructive load test for evaluating the live load carrying capacity of bridges. Moreover, this manual also includes a detailed procedure to perform a load test and suggests incorporating the load test results in the load rating calculation. Before the Manual for Bridge Rating through Load Testing, Pinjarker et al. (1990) modified the NCHPR 12-28 (13), "Nondestructive Load Testing for Bridge Evaluation and Rating" and developed guidelines for non-destructive load testing to intensify make the conventional rating procedure more accurate. Lichtenstein (1994) subsequently introduced the concept of two major load tests i.e. diagnostic tests and proof tests in the research project 12-28(13) A, "Bridge Rating Through Nondestructive Load Testing." NCHPR 12-28 (13) A also demonstrates the selection of bridges for load tests, provides a detailed procedure for load testing, incorporates load test results in load rating of bridges (Albrahemmi 2018).

2.2 AASHTO Manual for Bridge Evaluation (2018)

Two types of load testing, diagnostic test and proof test are described in the (2018) third edition of AASHTO Manual for Bridge Evaluation (MBE). Diagnostic tests are performed to determine certain responses of the bridge, including responses to loads, the distribution of loads, and validation of analytic models. Proof tests, however, are used to evaluate the maximum safe load capacity of the bridge, provided that bridge behavior remains within the linear-elastic range

(AASHTO 2018). Load tests can also be classified as static load tests and dynamic load tests. Additionally, unintended composite action, unintended end fixity, the effect of secondary components, non-structural components, and load carried directly by the deck are the main factors that may influence the actual behavior of bridges.

2.3 Factors Affecting Load Carrying Capacity

Diagnostic tests are more commonly used when there is any uncertainty in the bridge performance and response of the bridge under live load. Several factors influence the responses of bridges. A field load test is essential to verify the presence of these factors. Lichtenstien (1994) classified these factors that affect the load capacity of a bridge to primary and secondary factors with a notation when the field inspection or field test is needed for verification (Table 2-1).

Table 2- 1 Factors affecting bridge load capacity (Lichtenstien, 1994)

Variable	Factor Designations
Unintended composite action	P, I/T
Participation of parapets and railings	P, A
Difference between actual & assumed material properties	S, I/T
Participation of bracing and secondary members	S
Differing support characteristics and unintended continuity	S, I/T
Analysis/load distribution effects	P, A
Effect of skew	S, A

*(P = Primary Factor, S = Secondary factor, A = Included in conventional analysis, I/T = Inspection or testing need to verify)

2.4 Nondestructive Testing (NDT)

Non-destructive evaluation (NDE) techniques are efficient ways for condition assessments of bridge structures. Through visual inspection, severe problems can be identified when those problems reached the concrete surface whereas with nondestructive technologies, such as sound waves, the electromagnetic wave can identify the deterioration within the bridge deck. Among

various NDT technologies, Ground Penetrating Radar (GPR) and Impact Echo (IE) are widely used in the structural member assessment.

2.4.1 Ground Penetrating Radar (GPR)

GRP was initially used in 1940 to detect metal objects. The application of GPR in civil engineering was introduced in the 1980s (Zaki et al. 2018). GPR is a useful device for the structural health monitoring system. The radar generates pulses via the geophysical method to gather information of the surveyed surfaces. The working method of GRP is shown in Figure 2-1.

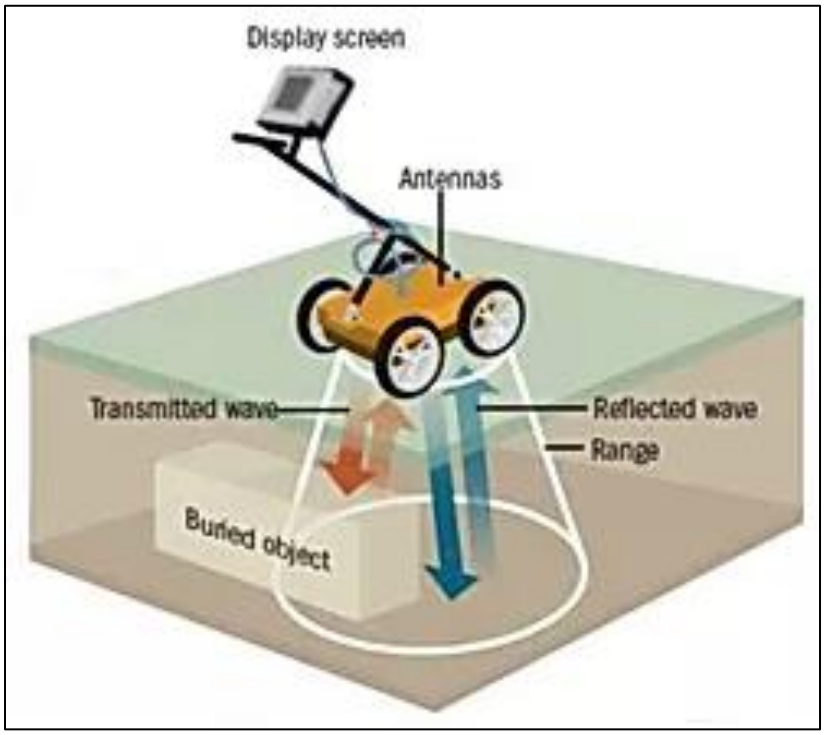

Figure 2- 1 Working theory of GPR

When other NDT techniques, such as ultrasonic testing, infrared testing, and pulse-echo testing cannot be used for limitations i.e., time constraint, expert equipment handler, then GPR techniques will typically be implemented to:

- Measure the thickness of road surfaces
- Conduct forensic evaluation of structures

- Used in military and security purposes
- Extract geological information
- Locate of moisture variations
- Locate presence of voids

Moreover, in bridge structures, GPR can evaluate concrete deck thickness, concrete cover, rebar location and configuration, and potential delamination (Omar et al. 2017). Detection of reinforcing bars in concrete structures is one of the most widespread applications of GPR in Civil Engineering. GPR is also useful for the deterioration mapping of old bridge decks. Hasan and Yazdani (2014) performed a nondestructive evaluation to detect concrete cover of a full-scale four span cast-in place concrete deck using GPR. The contour map (Figure 2-2) of the concrete cover was plotted from GPR data, and the contour map indicated a significant portion (48%) of the bridge deck had inadequate cover. Inadequate rebar cover may cause rebar corrosion and reduce moment capacity due to reduced moment arm.

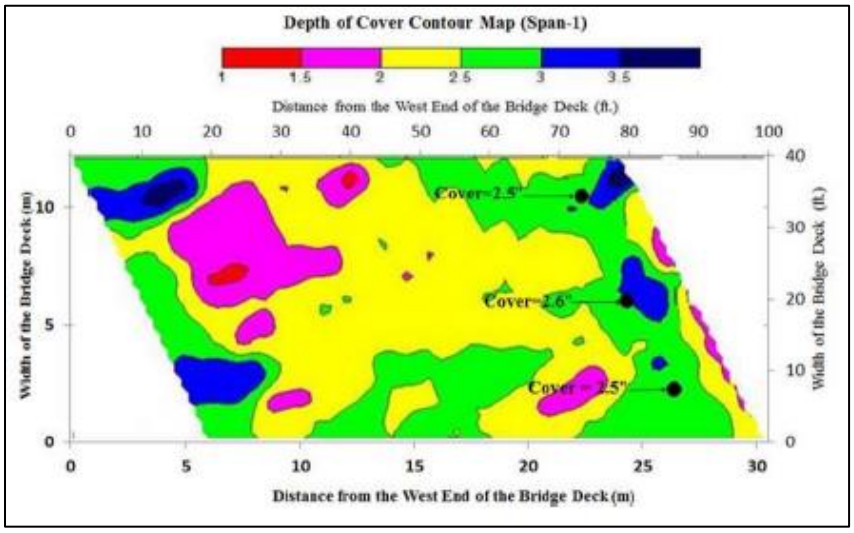

Figure 2- 2 Clear cover contour map from GPR (Hasan and Yazdani, 2014)

Rathod et al. (2019) used a GPR and a rebar detector to evaluate an existing bridge deck and reinforced concrete panel in order to determine the rebar diameter, spacing, and cover depth. In comparison to a rebar detector, GPR offered consistent and precise data for determining rebar

spacing and cover and demonstrated its data processing efficiency. Figure 2-3 presents the rebars gird generated from GPR data.

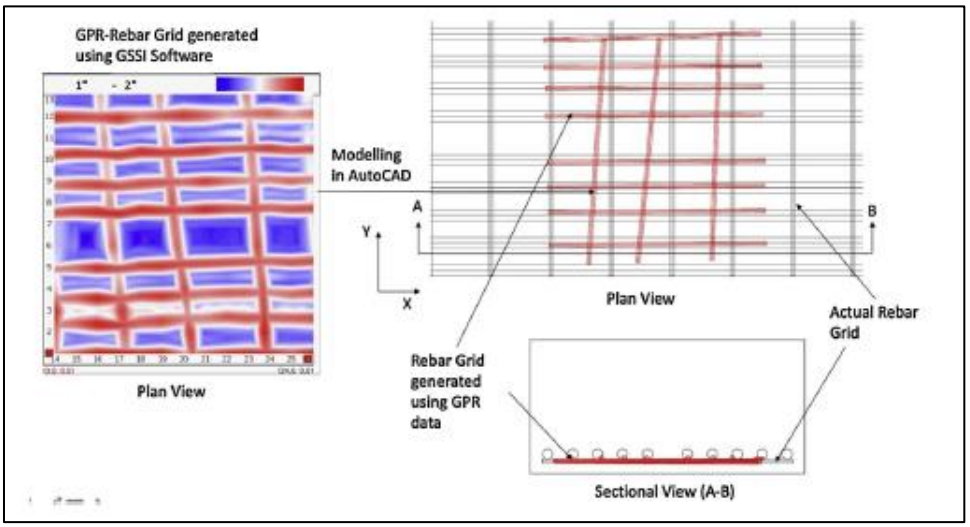

Figure 2- 3 Rebar grid generated from GPR (Rathod et al. 2019)

Wiwatrojanagul et al. 2017 described a method for locating rebars in reinforced concrete structures using GPR and a hyperbolic signature analysis. GRP data from concrete specimens and dry sand simulation tanks implanted with buried items demonstrated that the cover thickness of a dry sand sample exhibited more accuracy than the cover thickness of a concrete specimen. Hyperbolic reflection revealed no variation in the diameters of rebars ranging from 0.23 in. to 1.26 in.
Additionally, Zaki et al. (2018) indicated that GPR may be used to detect the existence of rebar corrosion. The researchers scanned the reinforced slab with a GPR at a frequency of 2 GHz. The results of the a- and b-scans indicated that rebar corrosion may be detected early on, prior to visible damage.

According to Hasan and Yazdani (2015), the relationship between the maximum amplitude of GPR data and the amount of corrosion may be used to estimate the amount of corrosion quantitatively. While the authors employed solely accelerated corrosion of rebars, Raju et al. (2018) utilized accelerated corrosion of rebars embedded in a prototype concrete beam. Additionally, the study indicated that two critical GPR characteristics, the maximum reflected wave amplitude and the

two-way travel time (TWTT), may be quantitatively related to the level of corrosion on embedded rebars in concrete.

2.4.2 Impact Echo (IE)

IE is another widely used non-destructive testing (NDT) method to detect internal defects/delamination within concrete structures. The working method of IE is shown in Figure 2-4. IE produces short-duration mechanical impact and creates a transient pulse that propagates through the solid in the form of three types of stress waves, namely P wave, S wave, and R wave. Both the P and S waves have a spherical wavefront and are associated with normal stress and shear stress, respectively, while the R wave is a surface wave that travels along the surface, away from the impact point (Carino, 2001). The schematic diagram of these waves is shown in Figure 2-5.

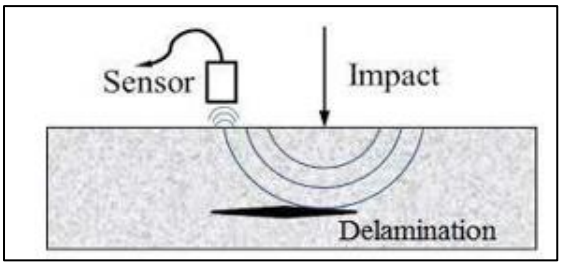

Figure 2- 4 Impact Echo work theory

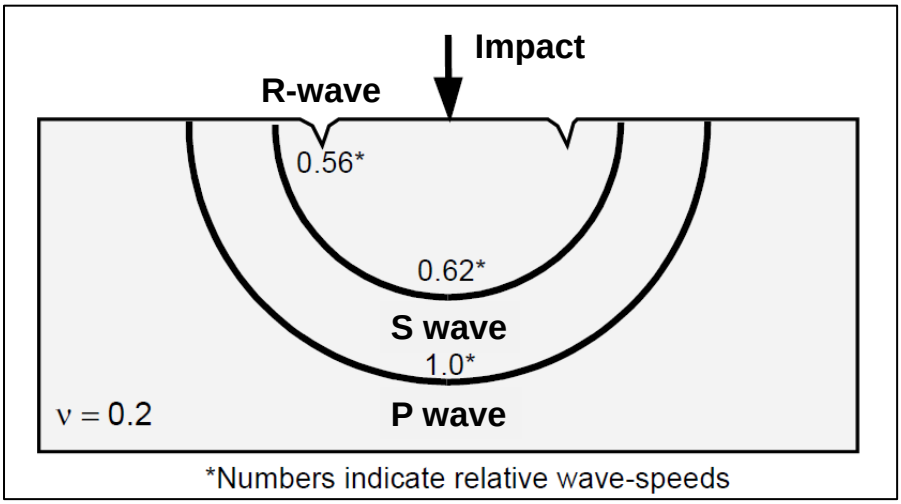

Figure 2- 5 Stress waves in concrete plate due to an impact on the surface (Carino 2001)

Gucunski et al. (2008) enhanced a bridge deck sonar system by combining IE with other ultrasonic seismic sensors. The Phase Array Ultrasonic Testing (PSPA) instrument, for example, may be used

to assess the surface of bridge deck pavement layers. The Carter Creek Bridge's upper condition assessment plot in Figure 2-5 (top) indicates that the deck appeared to be in excellent condition with minimal initial and propagated delamination and a small zone of severe delamination. Figure 2-5(bottom) depicts the Van Buren bridge deck's bottom condition assessment plot, which reveals severe deck degradation and delamination. The deck was subjected to chain drag testing for delamination, and the findings from both the bridge results were compared to the PSPA results. PSPA's improved methodology allows PSPA to identify early delamination, allowing for a more accurate evaluation of the delamination border and precise prediction of future propagation. When mild delamination is discovered before the member is too degraded to be recovered, a more effective rehabilitation method may be adopted.

Guthrie et al. (2019) developed an automated air-coupled impact-echo device that can draw a contour map of delamination over the concrete deck from a continuously moving platform. A map generated from air-coupled IE showed similar results to chain dragging data experimented on the same deck.

Kee et al. (2012) evaluated a full-scale simulated reinforced concrete bridge deck comprising simulated delamination and cracking defects using two separate non-destructive testing (NDT) methodologies, air-coupled IE and infrared (IR) thermography. The researchers found that a combination of air-coupled IE and IR thermography tests may be utilized to assess in situ reinforced concrete bridge decks in a reliable manner.

Scherr and Grosse (2020) validated the identification of delamination obtained from IE data by concrete coring and also stated that IE frequency may be utilized to assess the successful bond between old (prior to repair) and repaired new concrete. Additionally, the researchers studied delamination before (Figure 2-6) and after concrete deck restoration (Figure 2-7). IE data revealed that the bridge deck had been successfully repaired, with far less delamination showed in two scans.

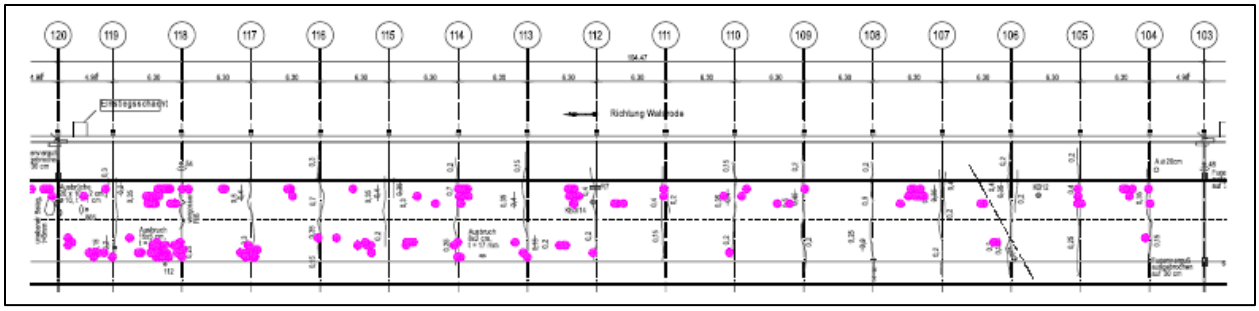

Figure 2- 6 Delamination before repair (Scherr and Grosse 2020)

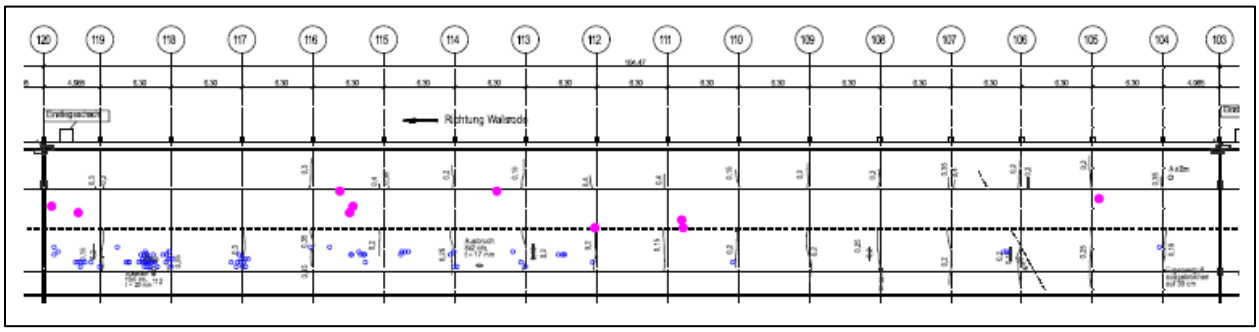

Figure 2- 7 Delamination after repair (Scherr and Grosse 2020)

2.5 Nondestructive Load Testing

While non-destructive testing techniques such as GPR and IE are restricted to detecting localized cracks and delamination in the superstructure, experimental load testing may precisely forecast a bridge's safe load-carrying capacity. Load testing determines how a bridge responds to a controlled and predetermined load. Several DOTs have successfully used diagnostic load testing to check the condition and load rating of existing bridges.

Brena et al. (2012) evaluated a damaged non-composite steel girder through load testing. The bridge was continuous three spans bridge. The researchers calculated Girder moments from the experimental test as well as from the FE model. Load distribution characteristics were then analyzed for the damaged girder. Brena et al. subsequently identified a new load path that was introduced as a result of the damage. Though the bridge was built in the late 1960's, the structure exhibited appropriate composite behavior. The neutral axis observed from the field test was similar to the theoretical composite neutral axis. In the case of finite element modeling, two different models were created assuming different supports conditions: i) roller and pinned supports ii) roller

and fixed supports. Composite action was incorporated in the model using a rigid link. The data from Brena et al's study suggests a good correlation with the experimental results.

Chajes et al. (1997) conducted a load test on a three-span steel girder slab bridge and determined that the girder and deck participated in unintended composite action. Additionally, the researchers determined that the composite action through diagnostic load test is a dependable source.

Barr et al. (2001) conducted a live load test on a prestressed concrete girder bridge and calculated the AASHTO LRFD live load distribution factors (LLDF) for three-spans. Changes in LLDFs due to continuity, skew angle, and load types were determined based on an adjusted finite-element model of the bridge. The AASHTO LRFD live load distribution factors were found to be 28% larger than the LLDFs obtained from the model which shows that AASHTO LRFD specifications are conservative compared to an actual experimental test. Other researchers, including Hodson et al. (2012); Dicleli and Erhan (2009); Yost et al. (2005), and Yousif and Hindi (2007), also agreed on the statement provided by Barr et al. (2001). Live load distribution factors (LLDFs) can provide a reliable assessment of the overall performance of the bridge structure.

Schiebel et al. (2002) performed a diagnostic load test of a repaired bridge to assess the additional capacity after rehabilitation. The bridge had a load posting before being repaired. The test data confirmed the removal of the load posting. Moreover, Yost et al. (2005) conducted an experimental load test and calibrated the finite element model using strain data obtained from the load test. The researchers concluded that the load rating using the FE model was higher than the conventional rating method.

2.6 Load Rating

The main objective of nondestructive load testing is to ascertain a bridge's load rating. Rating processes take into account the state and level of degradation of the bridge's structural components. The load rating of an older bridge should be based on a recent and comprehensive field assessment (AASHTO MBE 2018). The load rating process includes a thorough examination and an accurate calculation of the live load-carrying capability of the vehicle.

Additionally, the bridge load rating serves as a foundation for establishing the bridge's safe load carrying capacity (AASHTO MBE 2018). In the event of load rating, engineering judgment is necessary to ensure the bridge's safe operation while deciding on posting and permits. The exact load ratings are important for posting loads or strengthening bridges, as well as when deciding on overweight vehicle permits. A bridge's load rating is determined by the bridge's present structural condition, material qualities, loads, and traffic circumstances (AASHTO MBE 2018).

A rating value greater than one or higher indicates that the bridge can safely carry the vehicle for which it was rated. Each structural component is rated individually, and the rating of the bridge is controlled by the member with the lowest rating. Furthermore, two different levels of load rating are described in the AASHTO MBE 2018 i.e., inventory level and operating level. Inventory rating level represents the routine live load capacity that the bridge can support over an indefinite period of time. The operating rating level expresses the live load capacity for less-frequent vehicles as well as commonly used to determine the maximum permissible live load.

AASHTO MBE (2018) illustrates three methods for bridge load rating as follows i) Allowable Stress Rating (ASR), ii) Load Factor Rating (LFR), and iii) Load and Resistance Factor Rating (LRFR). Federal Highway Administration Policy demands bridges designed by ASD be rated by LFR or LRFR. This policy also strictly mandated that all bridges designed after October 1, 2007, use LRFD specifications.

Bagheri et al. (2018) additionally proposed a non-destructive method for load rating of reinforced concrete bridge without any structural plan. The proposed load rating approach was validated by performing a field load test of a full-scale bridge. The results of their study suggested that the suggested method was capable of determining structural and material properties in addition to calculating the load rating factors with less than 5 % error, compared to the traditional method.

Sanayei et al. (2015) compared three methods used to load rate a full-scale bridge based on the LRFR approach. The methods in the study included i) conventional rating using simplified line girder analysis, ii) using strain data from load test to adjust design rating for in situ bridge condition, and iii) using a finite element model to observe three dimensional (3D) structural behavior. The bridge in Sanayei et al.'s study was three-span continuous composite bridge with a concrete deck over steel girders. The authors concluded that a conventional bridge rating is conservative and also suggested that structural evaluation using more sophisticated modeling or incorporation of NDT results can provide flexibility when dealing with aging bridges. The bridge rating comparison of three different method is presented in Figure 2-8.

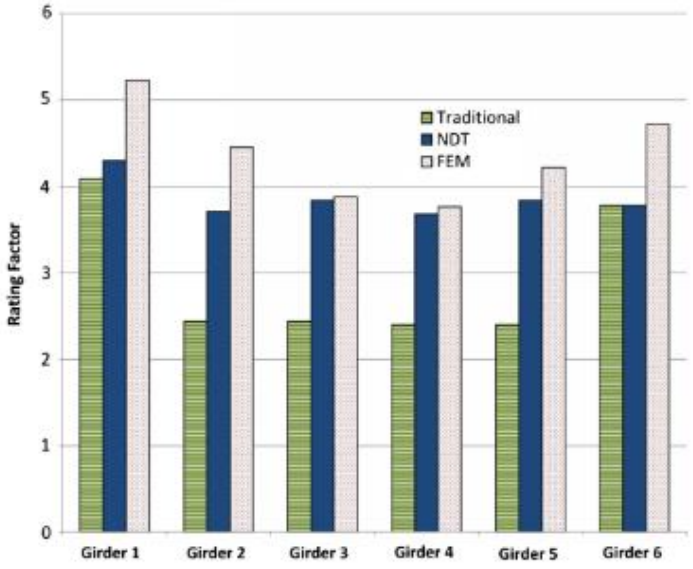

Figure 2- 8 Load rating factor comparison (Sanayei et al. 2015)

2.7 Finite Element Modeling of Load Tested Bridge

Experimental investigations have been conducted to assess structural member performance under a variety of live loading circumstances. While experimental investigations may be used to determine the real performance of structural components, they are often time consuming, costly, and have limits, such as traffic closure or access to the bridge member. As a result, researchers are attempting to develop an effective way for evaluating the structural elements' performance. Finite Element Analysis (FEA) is a method that is often used to investigate the behavior of various structural materials and components. This approach is gaining popularity because to its beneficial

influence on the growth of engineering and computer expertise, as well as the fact that it is quicker and less expensive than experimental methods.

Creating comprehensive three-dimensional finite element models of highway bridges is a practical solution that can be effectively calibrated using experimental data (Sanayei et al. 2012). These calibrated models may be used to conduct further parametric investigations and also serve as a guide for bridge management choices. As a result, it is required to develop a model that precisely simulates the overall structure's geometrical features, material characteristics, boundary conditions, and load distribution. Additionally, a baseline model may be utilized to develop long-term monitoring systems.

Chung and Sotelino (2006) investigated several FEM approaches in order to more precisely model composite bridges. By comparing mid-span strain levels, the researchers found a substantial correlation between FEM and full-scale laboratory measurements. Zhang and Aktan (1997) analyzed a two-dimensional and three-dimensional modeling approach and found that the two-dimensional model may also be utilized for modeling since it takes less computer processing time than a three-dimensional model. Additionally, the researchers showed that a two-dimensional model had a high degree of relative accuracy when compared to observed data. FEMs had lower live load distribution factors than AASHTO and LRFD standards (Mabsout et al. 1997)

Barr et al. (2006) further validated FEM using NDT data to calculate a more accurate load rating factor. Chajes and Shenton (2005) presented a load rating method using NDT data, including investigation of support fixity, composite action, and the effects of secondary members. Jauregui and Barr (2004) used experimental data to validate FEM which was created to refine the original load rating for a prestressed concrete bridge. Moreover, Yost et al. (2005) used experimental data obtained from NDT to calibrate the FE model and concluded that load rating using the FE model provides a higher load rating compared to the conventional method. Based on the load tests and load rating of more than 200 highway bridges, approximately 95% of these bridges obtained higher load ratings when the calibrated FEM approach was implemented. Posted limits could be eliminated on approximately 45% of the bridges tested (Yost et al. 2005).

2.8 Strengthening and Repair of Bridge Structures

Over the last two decades new methods have developed for strengthening bridges to meet the increasing demands placed on the aging infrastructure by daily traffic. In the following subsections, several retrofitting methods for steel non-composite bridges are presented.

2.8.1 Removal of Deck-Top Concrete

Bridges are typically designed to last for 75 years, but bridge decks deteriorate at a faster rate than other structural elements because of the direct contact with day-to-day traffic. Over time concrete deck often begin to show lots of cracks, spalling, and delamination. These cracks and delamination lead to a reduction in the stiffness of the concrete deck. As a result of reduced stiffness, moment capacity of the deck is compromised. The most common and easy way to fix this problem is chipping off the delaminated concrete from the top deck surface and laying of new concrete. As a result of laying new concrete, the stiffness of the deck regains hence increases its load-carrying capacity. Figure 2-9 shows a typical laying of new concrete placement.

Figure 2- 9 Bridge deck rehabilitation on I 695 and Route 702 (Wagman, 2005)

Extensive research was performed by providing a thin layer of ultra-high-performance concrete (UHPC) on top of normal concrete by Bridge Engineering Center (2018). Thermal imaging was used to examine the performance of the overlay, especially at the UHPC interface, to identify any

delamination. Prior to field implementation, a laboratory test was conducted to check the effectiveness of new concrete laying. The results showed that a UHPC overlay in the positive moment region increased the strength by 18%.

2.8.2 Application of Carbon Fiber Reinforced Polymer on Deck Concrete

Carbon Fiber Reinforced Polymer (CFRP) is rapidly gaining popularity as a cost-effective method for strengthening and retrofitting concrete structures. CFRP provides a number of benefits over conventional retrofit techniques, including a high strength-to-weight ratio, greater corrosion resistance, simplicity of installation, and suitability for use in regions with restricted access. Figure 2-10 presents the application of CFRP underneath the deck.

Figure 2- 10 Application of CFRP sheet (Horse Construction)

Strengthening concrete buildings using joined steel plates was a common repair procedure in the late 1980s and early 1990s. Arockiasamy et al. (1995) rehabilitated steel beams using epoxy-bonded steel plates, establishing a precedent for the use of steel plates in repair. During the mid-1980s, the usage of fiber-reinforced polymer (FRP) as a substitute for steel plate gained favor in Germany and Switzerland (Nanni 1995).

Ichimasu et al. (1993) examined the load-bearing capability of a one-way slab externally bonded with carbon fiber reinforced polymer (CFRP). According to the authors, the yield load rose by 30-40%. Additionally, Sheikh (2002) showed that the use of CFRP fabric in one-way slabs may

enhance the ultimate capacity by 148%, while Seim's (2001) research indicated that the ultimate capacity might be raised by 370%, depending on the quantity of CFRP used.

Erki and Heffernan (1995) found that GFRP in a one-way slab system may increase ultimate capacity by 18 percent to 119 percent (Shiek 2002). It is also possible to raise the ultimate capacity from 50% to 100% by using pultruded CFPR strips instead of fabric (Seim 2001). According to Seim, the overall ductility of the system may be compromised as a result of the external use of FRP. Eeki and Heffernan (1995) tested the ultimate capacity two-way slabs using FRP fabrics and concluded that the ultimate capacity of the slabs increased, ranging from 70% to 200%. Mosallam and Mosalam (2003) also supported Erki and Heffernan statement. Additionally, the use of GFPR can increase the ultimate capacity by 19% (Eeki and Heffernan 1995).

Petrou et al. (2008) conducted tests on one-way slab and two-way slab for both monotonically and fatigue behavior. For a one-way slab, a total of five specimens were tested. Three slabs were retrofitted with CFRP strips bonded to their soffits, and two were un-retrofitted control specimens. One un-retrofitted and two retrofit slabs were tested monotonically. Rest slabs were tested under fatigue load. A similar approach was followed in the case of the two-way slab. The monotonically tested one-way slabs showed an increase in the ultimate strength of 18.1% whereas two-way slabs showed a 13.8% increment.

2.8.3 Installation of New Steel Joist/I beam

Rai et al. (2013) analyzed a finite element model using SAP 2000 to verify the application of three rehabilitation schemes before on-field application as follows: i) Installation of new steel joist along the spanning direction, ii) addition of a 4 in. thick concrete slab on the top of the existing deck slab, and iii) repair of the concrete bottom surface by adding a layer of high strength micro concrete. Numerical studies showed steel joists were able to reduce the areas of high stress. Yield moment capacity increased by 70% due to the addition of 4 in. concrete. Abovementioned authors also expected an increase of 380% in moment capacity when the joist was in composite action. Figure 2-11 shows the steel joists underneath the deck slab.

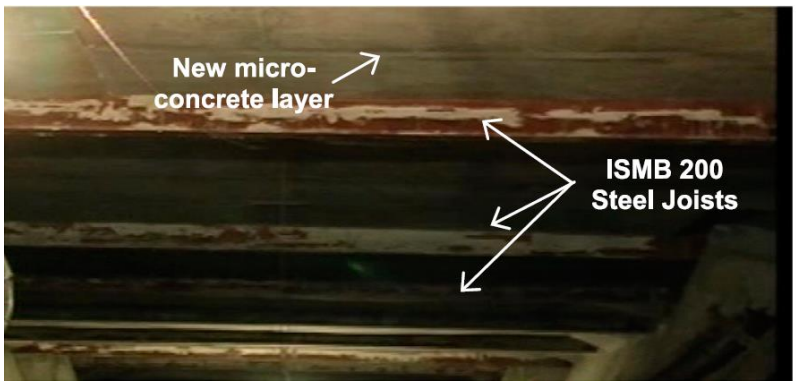

Figure 2- 11 Steel joist underneath the deck (Rai et al. 2013)

2.8.4 Installation of Fiber Reinforced Polymer (FRP) I Beams

Waal et al. (2017) examined the effectiveness of two different FRP strengthening techniques, mostly on flexural capacity and flexural stiffness of 60-year-old prestressed RC deck slabs. Two schemes were i) adhesively bonded carbon FRP (CFRP) pultruded plate underneath the deck and ii) adhesively bonded and mechanically fastened glass FRP (GFRP) I beam and adhesively bonded CFRP pultruded plates. The researchers confirmed that both the systems increase the load at serviceability limit by 10% and 31%, respectively, whereas ultimate strength was increased by 54% and 105%, respectively. Figure 2-12a shows the cross-section of strengthened deck slab with CFRP laminate while Figure 2-12b shows the retrofitting scheme using GFRP I beam. The dimensions of the I beam is shown in Figure 2-12c.

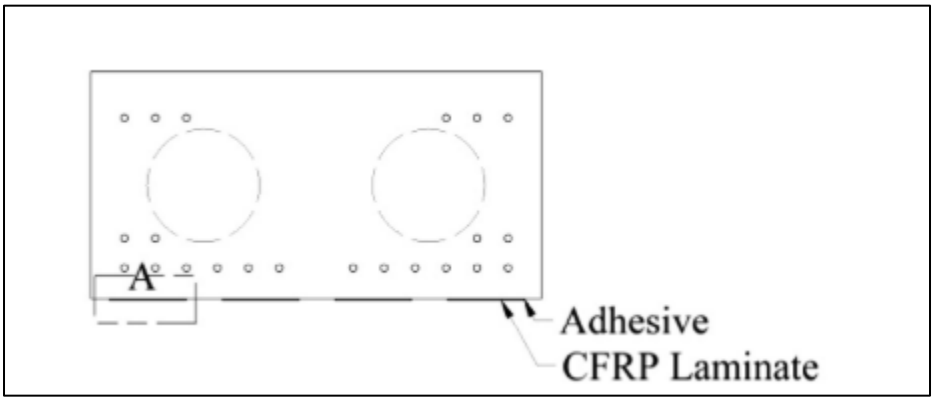

(a)

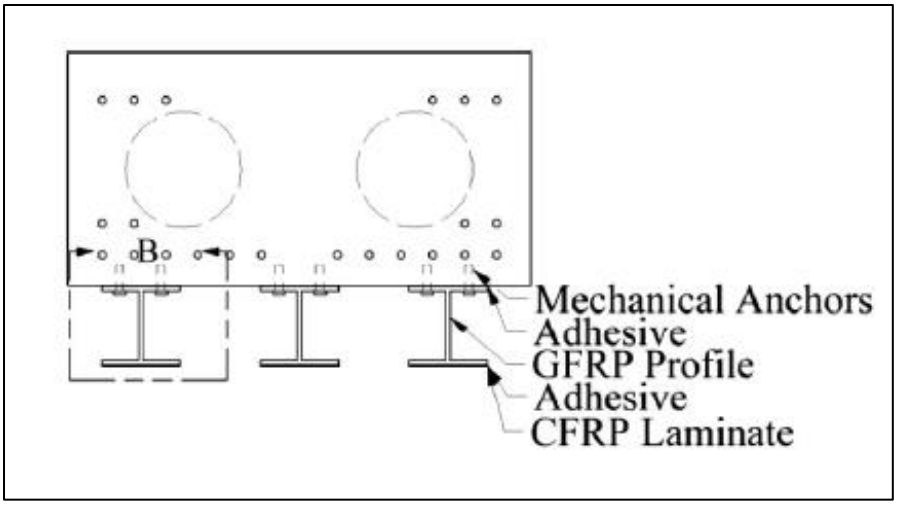

(b)

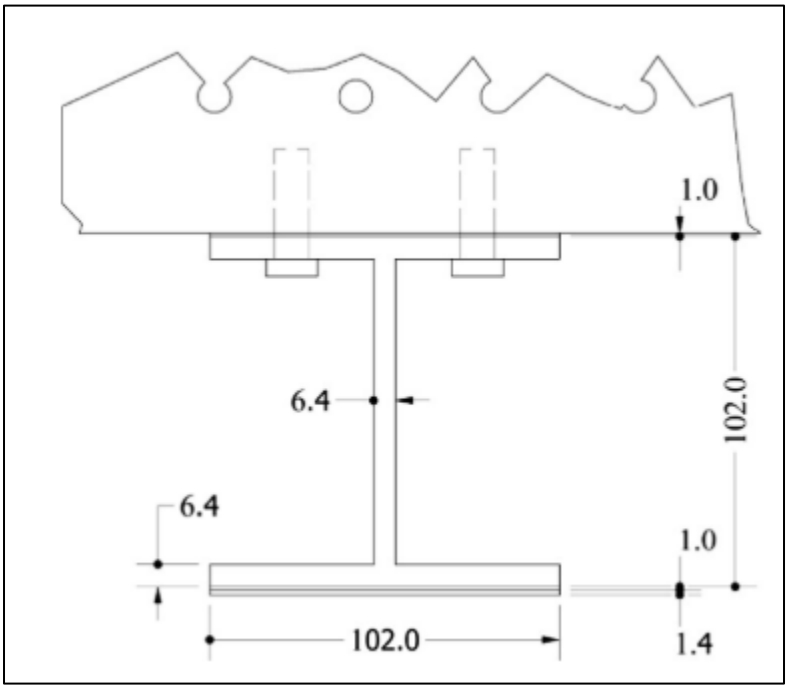

(c)

Figure 2- 12 Strengthened cross-section of deck: (a) with CFRP laminate; (b) with GFRP I beams; (c) dimension of the I beams (Waal et al. 2017).

2.8.5 New Concrete Deck Placement/SPS Deck Installation

Sandwich Plate System (SPS) is a structural composite material comprising two metal plates bonded with a solid polyurethane elastomer core (Figure 2-8). SPS has a low carbon footprint and is 100% reusable and recyclable. The SPS deck technology has less dead load than a comparable concrete deck.

Table 2-2 shows the comparison of weight between concrete and SPS deck system.

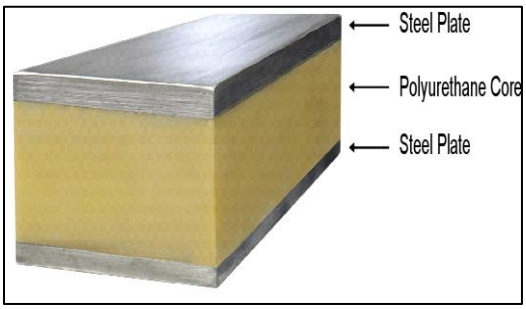

Figure 2- 13 SPS deck components

Table 2- 2 Comparison of SPS deck with concrete deck. (TxDOT)

Material	Weight
Concrete (8 in.)	100 psf
SPS (2 in.)	45 psf

Demolishing the whole deck and installation of a new deck system either with high strength concrete or SPS deck system (Figure 2-14) can increase the load-carrying capacity of the bridge deck. Being lightweight, the SPS deck has an advantage over the new concrete deck.

Figure 2- 14 Deck panel installation (Thomas et al. 2009)

The flexure behavior of the sandwich beam was studied extensively by Sofia et al. (2010). They came to the conclusion that when the temperature rises, the stiffness and strength of the sandwich beam decrease. A small coating of glue or core was used to consider a second steel plate to be on top of the steel deck. Flexural elastic behavior of sandwich beams was investigated using FEA modeling and simulations (FEA).

Thomas et al. (2009) installed a new SPS deck system to replace the old deck system. After installing the SPS system, load testing was conducted on the bridge to evaluate lateral load distribution factors and dynamic load allowance. Results from the study showed that the behavior of an SPS is better than the behavior of conventional systems. In recent years, the United States, Canada, and many countries in Europe and Asia have adopted the SPS deck system. Figure 2-15 shows the new installation of an SPS deck of the Dawson Bridge in Edmonton, Canada. The concrete deck of the bridge was removed prior to SPS deck installation due to extensive delamination.

Figure 2- 15 Re-decking of Dawson Bridge (Dialog 2010)

2.8.6 Application of FRP on Steel Girders

FRPs, specifically CFRP, are being increasingly used in steel structures due to its superior properties like light weight, high strength. Previously, additional steel plates were used to strengthen the steel structures. The retrofitting method that utilizes steel plates, however, requires heavy lifting equipment for the plates and additional dead load to the steel structure while CFRP is a more practical approach with less cumbersome equipment and load requirements (Tawfiq 2010). In Iowa, a bridge was strengthened by installing CFRP plates on the bottom flange of girders in the positive moment regions. Figure 2-16 shows the application of CFRP strips.

Figure 2- 16 Application of CFRP strips on girder (Iowa DOT)

Mertz and Gillespie (1996) strengthened W 8X 10 rolled beams that were 60- 80 in. long and 0.24 in. thick CFRP plates bonded to tension flanges. The beams were tested in four-point loading and showed 20% increase in flexural stiffness and more than 50% increment in strength just before the test was stopped due to buckling of the top flange. Additionally, the researchers conducted a full-scale test of two I girders 24 in. height, 252 in. long collected from a demolished bridge. Mertz and Gillespie concluded that the bottom flange of the girder was severely corroded and that strengthen scheme showed a significant increase in ultimate strength and flexural stiffness.

Salama et al. (2010) investigated the effectiveness of strengthening the steel girder with CFRP laminate. Five composite steel W 8 X 13 beams were tested in their study followed by four points

bending test procedure. The results of Salama et al.'s study showed a maximum flexural capacity increase by 62% after using CFRP laminates.

Tavakkolizadhe and Saadatmanesh (2003) examined the effect of the different number of layers of CFEP sheets to strengthen a steel-concrete composite beam. The beams' size was W 335 X 13.6 while the deck dimension was 3 in. thick and 35 in wide. and a unidirectional CFRP was used to bond to the bottom flange of the steel girder using one, three, and five layers of CFRP. The test results indicated that the ultimate capacity was increased by 44%, 51%, and 76% for one, three, and five layers, respectively.

Sen et al. (2001) conducted tests on six specimens having length of 240 in. long W 8 X 24 wide flange beams. Moreover, the beams were compositely topped with a 4.5 in thick and 28 in wide concrete deck slab. Three of the beams had a yield strength of 45 ksi while the remaining three beams had a yield strength of 53 ksi. Three beams were strengthened with 0.078 in. CFRP plate while the other two specimens were strengthened with a 0.2 in. thick CFRP plate. The result showed the strength of the beams with 45 ksi increased by 21% and 52% for the 0.078 in. and 0.2 in. CFRP plate, respectively. In the case of the beams with 53 ksi strength, the ultimate capacity increased by 9% and 32% for the 0.078 in. and 0.2 in. CFRP plate, respectively.

Shaat et al. (2004) compared the results of two previous studies to investigate the effects of the CFRP reinforcement ratio in flexural strength increment for beams with different yield strengths. The strengthening ratio was considered as the ratio between the total area of the CFRP and the steel section. Shaat et al. determined that there was a higher flexural strength when there was a high reinforcement ratio. Shaat et al. additionally concluded that steel with lower-yielding strength showed a higher increment in flexural strength.

The steel girders of the Interstate 95 bridge were strengthened by Miller et al. (2001). Epoxy was used to attach CFRP laminates to the steel girders soffit. After a small-scale laboratory test extensively tested the viability of the strengthening approach, the technology was employed on this bridge. The results of Miller et al.'s study confirmed that CFRP cover plates can be used to restore reasonable losses of stiffness and strength in deteriorated bridge girders and increases in stiffness of 10–37% were achieved for the corrosion-damaged bridge girders.

2.8.7 External Post-Tensioning (PT) of Beams

External PT increases the stiffness and the load-carrying capacity of the steel beam by adding reinforcing steel/CFRP bars to a segment of the beam. In Iowa, a bridge (Number 3903.0S141) was strengthened with the post-tensioning of CFRP rod. It is located in southwest-central Iowa in Guthrie County approximately 1.6 miles west of Bayard, Iowa, carrying state highway IA 141 over Willow creek. The PT system was installed in the positive moment region of the exterior girders (Terry et al. 2003). Although PT does not significantly reduce live load deflections, it does increase the live load carrying capacity of the bridge by generating strain opposite to the strain produced by dead load and thus allows the bridge to carry additional traffic live loads (Figure 2-17).

Figure 2- 17 Installation of PT system (Terry et al. 2003)

Post-tensioning tendons offer a reasonable way of strengthening the existing deteriorated structures (Krauser 2006). PT can be easily used in the structures to apply vertical forces at the needed points, as shown in Figure 2-18.

Figure 2- 18 Deviated beam strengthening tendons (Krauser, 2006)

Angel and Casas (2000) tested eight externally prestressed concrete beams under pure bending and combination of bending and shear. The authors concluded that reducing the length of the tendons increases the ultimate capacity of the beam by 5%.

Taoum and Holloway (2015) upgraded the steel beam using locally prestressed reinforce bars. The reinforcing steels were welded to beams flange and web at both ends. A manual jack screw was used for prestressing the reinforcing bars. The researchers tested seven different steel beams with different variables until failure under three points bending. Taoum and Holloway concluded that the level of pre-stress, the type of local prestress (internal or external), and the diameter of rebars used affects the beam load carrying capacity and stiffness. The results of their study also indicated that the application of local pre-stressed reinforcing bars in conjunction with a stiffener to prevent buckling could add up to 60% of the load-carrying capacity of the steel I-beams. Moreover, the larger the diameter, the higher beam's stiffness. Figure 2-19 shows the external post-tensioning of the steel beam while Figure 2-20 presents the experimental setup.

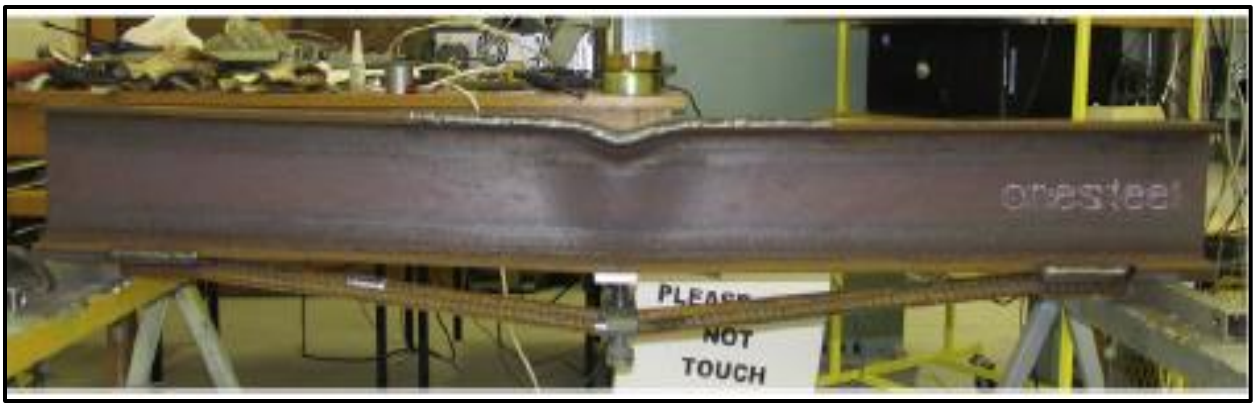

Figure 2- 19 External post-tensioning of steel beam (Taoum and Holloway, 2015)

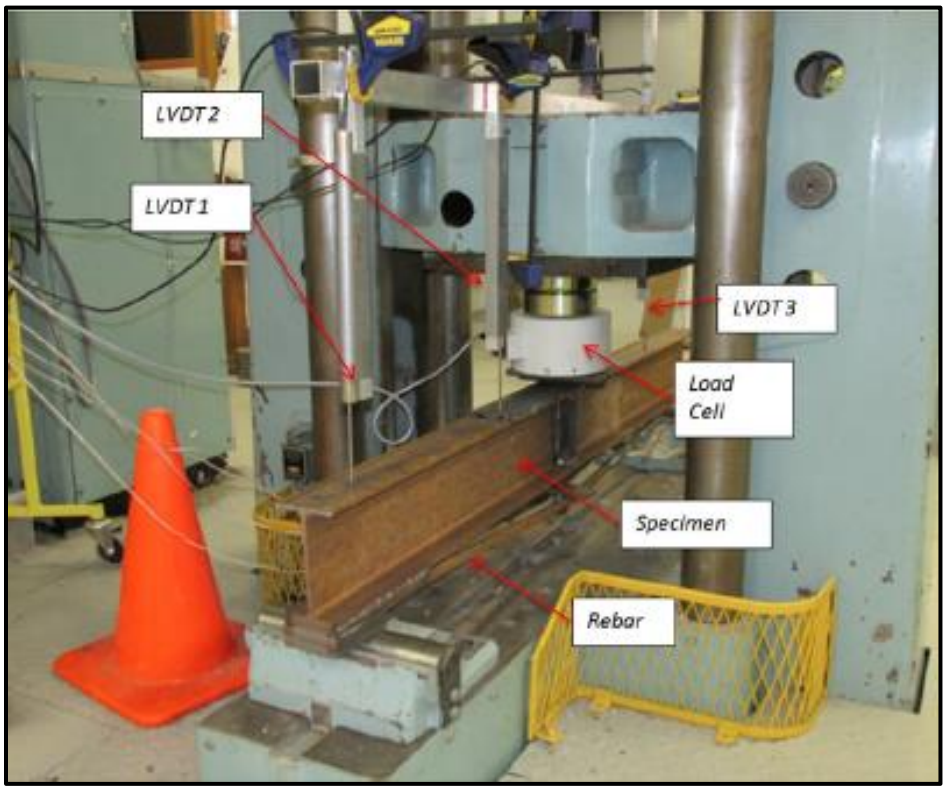

Figure 2- 20 Experimental setup (Taoum and Holloway, 2015)

2.8.8 Shear Connector on the Girder Line

One efficient way to increase the live load carrying capacity for the existing bridges is to develop composite action between the concrete deck and steel girders, allowing steel girders to work with the concrete deck as a one-element and helps to carry more load than non-composite conditions. Collin et al. (2015) removed the concrete on the girder line and welded headed studs to the steel

girder before pouring new concrete. Figure 2-21 shows the welded headed studs on the top of the girder line.

Figure 2- 21 Welded headed studs welded to the steel girder (Collin et al. 2015)

Kwon et. al. (2007) tested large-scale beam specimens retrofitted with post-installed shear connectors, one with double-nut bolts and the other with adhesive anchors. The ultimate strength of the specimen retrofitted with double-nut bolt shear connectors was 42% greater than the baseline non-composite specimen. The ultimate strength of the specimen retrofitted with adhesive anchors was 47% greater than the baseline non-composite specimens. Figure 2-22 shows different shear connectors used to connect the steel girders and concrete deck. The experimental set up of the test is shown in Figure 2-23.

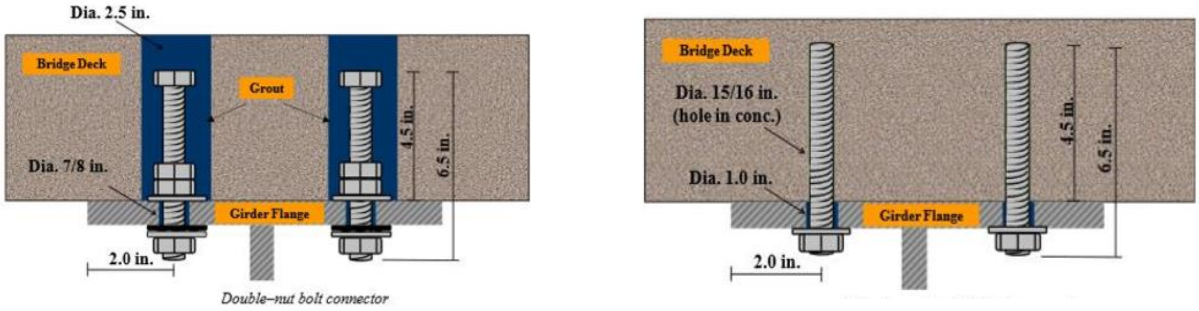

(a) (b)

Figure 2- 22 Examples of shear connectors: (a) Double nut bolt; (b) Adhesive anchor (Kwon et al 2009)

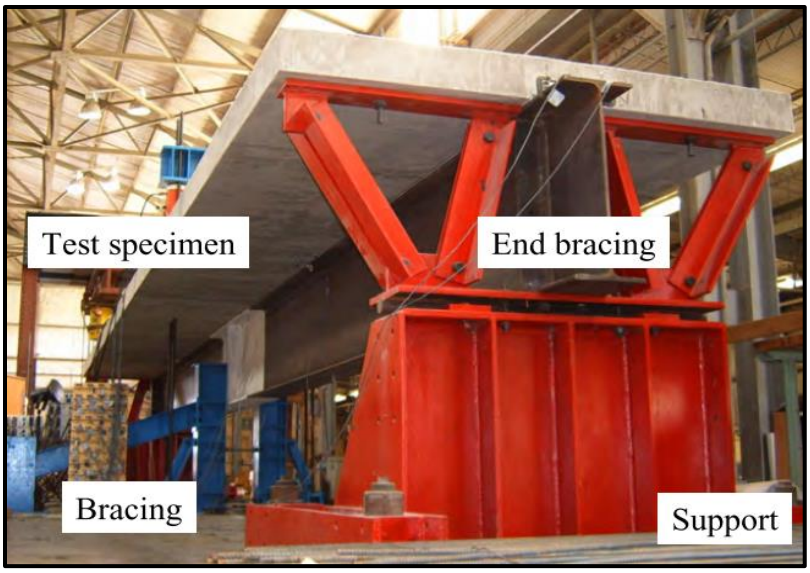

Figure 2- 23 Experimental set up for full-scale test (Kwon et al. 2009)

2.8.9 Shear Connector welded to Plate

Kwon et. al. (2007) presented the effectiveness of shear connector welded to plate and the attached the plate to the girder top flange. Due to the fact that the stud is shop-welded to a separate steel plate, a smaller diameter hole is needed in the slab (Figure 2-24).

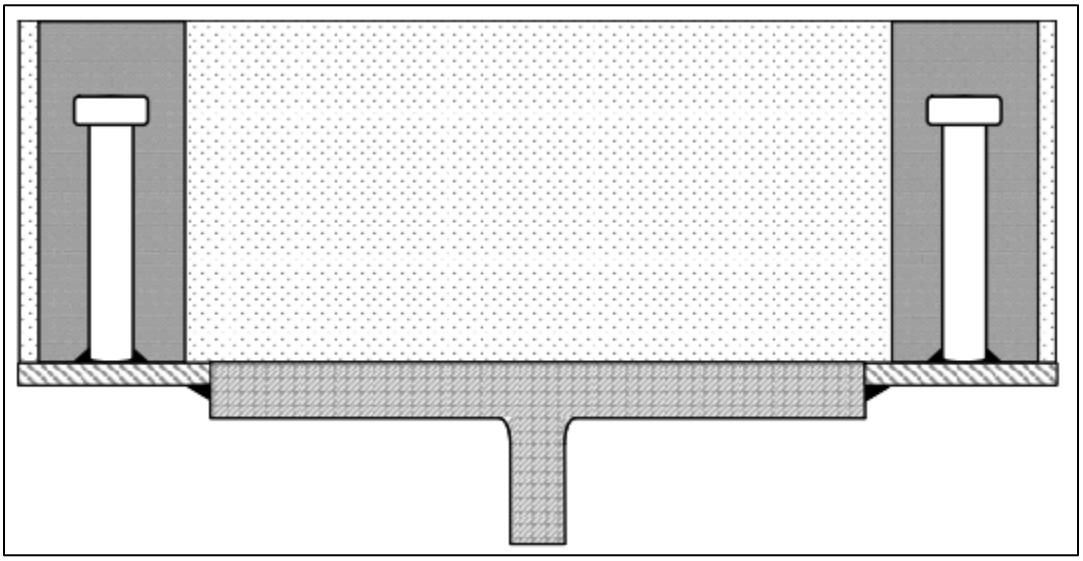

Figure 2- 24 Shear connector welded to plate

2.8.10 Coiled spring pins on the girder flange

Coiled spring pins (Figure 2-25) are cylindrical with no specific shapes and can be force-fitted during installation. The pins can be installed from the bottom of the steel girders without any adhesive or grout with no traffic interruptions. (Craig et al. 2001).

Figure 2- 25 Coiled spring pin (Collin et al. 2015)

In Pitsund Bridge coiled spring pins were used to create the composite action between the deck and steel girder. The installation involved drilling through the steel flange and into the concrete deck from underneath, applying lubricant, and pressing the spring pins into place by using a hydraulic jack. Figure 2-26shows the installation of a spiral pin into a bridge.

Figure 2- 26 Hydraulic jack used for inserting spiral pins into the bridge (Collin et al. 2015)

2.9 Case Study of Impact Damage Repair

TxDOT started using FRP for concrete bridge repair in 1990. The procedure has resulted in significant time and financial savings (Yang et al. 2011). FRP has been utilized to repair concrete structures damaged by corrosion of reinforcing steel, girders damaged by collision from over-height vehicles, and concrete bridges with defective load-rating and shear reinforcements in several instances (Bradberry and Wallace 2003).

A CFRP-repaired impact-damaged beam in Texas is shown in Figure 2–27. After being struck by an over-height car, the outside beam was extensively fractured in two places between two inside diaphragms. The collision severed the prestressing strands. Concrete repair and epoxy injection were used to fix the damaged girder, and then wet lay-up procedures were used to build one ply of continuous CFRP to cover the whole bottom flange and web (Yang et al. 2011).

(a) (b)

Figure 2- 27 Bridge Condition: (a) impact damaged; (b) impact damaged repaired with CFRP (Yang et al. 2011)

Chapter 3 BRIDGE DESCRIPTION

The St. Francis Bridge carrying St. Francis Avenue over I-30 east of Dallas downtown consists of North Bound (NB) and South Bound Bridge (SB) bridges. The National Bridge Inventory (NBI) number of the bridge is 180570000911196. With no skew associated, the bridge is perpendicular to the I-30 highway. Figure 3-1 shows the location of the bridge while Figure 3-2 presents the side view of the bridge.

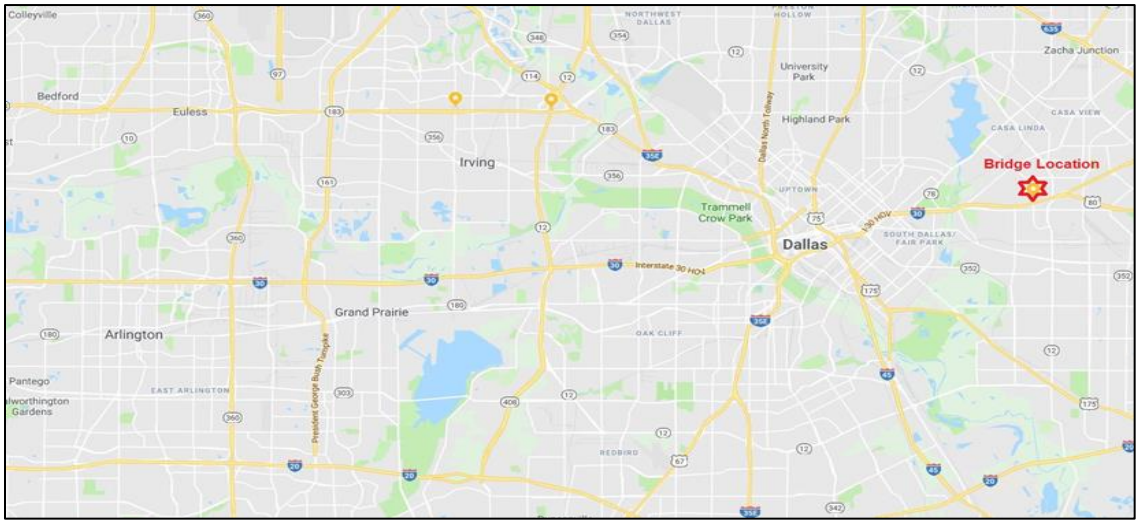

Figure 3- 1 Location of the bridge

Figure 3- 2 Bridge side view (Google Earth)

The St. Francis bridge was built with steel I-girders and a non-composite concrete deck on top. There are six spans symmetrical along the center length of the bridge. The spans are 30 ft., 60 ft., and 70 ft. in length, with the total length of the bridge measuring 320 ft. The 30 ft. span is simply

supported, while the 60 ft., and 70 ft. spans consist of a continuous girder across the bent (Figure 3-2). The deck thickness is 6.5 in., consisting of cast-in-place (CIP) concrete. The bridge superstructure was designed for H20 loading, according to the American Association of State Highway and Transport Officials (AASHTO) Specifications (1953). The concrete deck was designed as Class A. According to Texas Highway Department Standard Specification for Road and Bridge Construction (1950), minimum compressive strength of Class A concrete was 3,000 psi.

The yield strength of the girders was assumed 33 ksi as per the Table 6A.6.2.1-1 from AASHTO MBE (2018) as the bridge was built in 1960. In the case of the rebars, billet or intermediate grade were considered. The yield strength of the rebar was assumed as 40 ksi according to Table 6A.5.2.2.-1 from AASHTO MBE (2018).

The total width of the deck is 29.25 ft. measured from outside of the traffic barriers. The clear roadway width inside the barriers is 22 ft. Table 3-1 shows the width and height of the barriers, median, and curbs.

Table 3- 1 Barriers, medians, and curbs dimensions

From East to West	Width (in)	Height (in)
Barrier	19	32
Sidewalk	42	5.5
Median	36	5.5

The bridge has a total of four steel girders spaced at 8 ft. center-to-center. Per the as-built drawing of the bridge, only simply supported spans have shear connectors. Two different types of steel I-girders were used. Table 3-2 shows the span length and shapes for the girders.

Table 3- 2 Steel girder types*

Girder Designation	**30 ft. Span** (Simply Supported and composite)	**60 ft. and 70 ft. Spans** (Continuous and non-composite)
A	33 WF 130	33 WF 130
B	24 WF 76	33 WF 130
C	24 WF 76	33 WF 130
D	24 WF 76	33 WF 130

**Bridge girders are symmetric about the centerline*

The top view, steel framing plan, and cross-section at mid-span of the bridge are shown in Figures 3-3, 3-4a, and 3-4b, respectively.

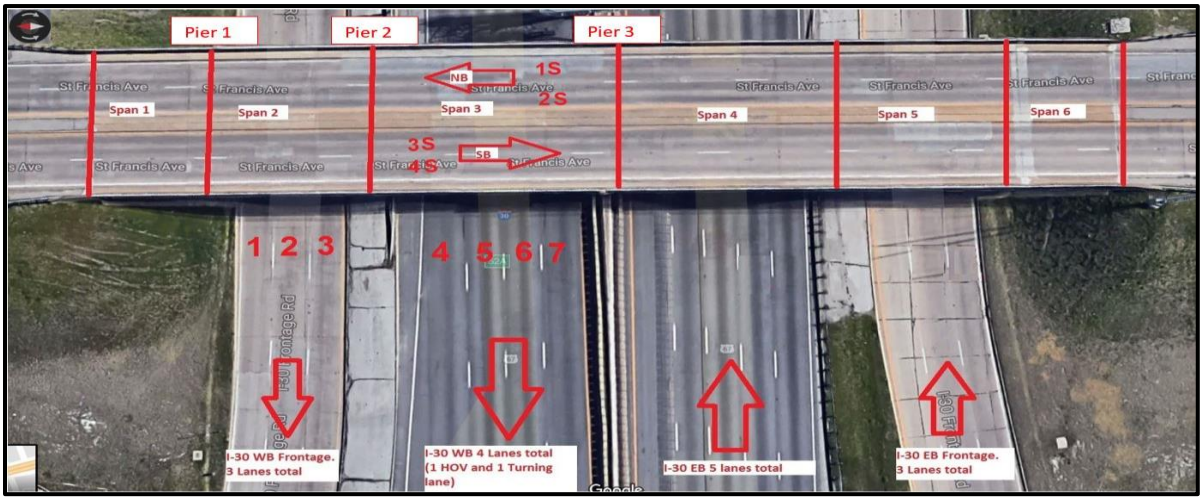

Figure 3- 3 Top view of the bridge

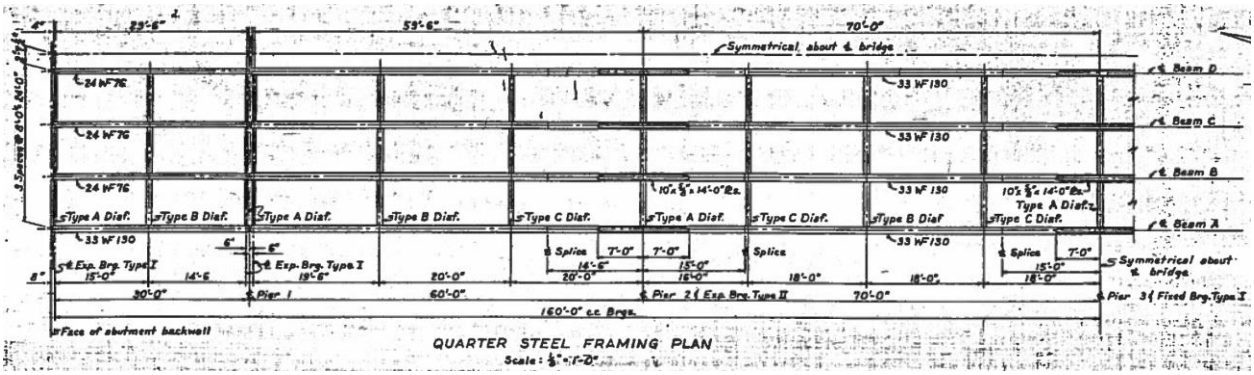

(a)

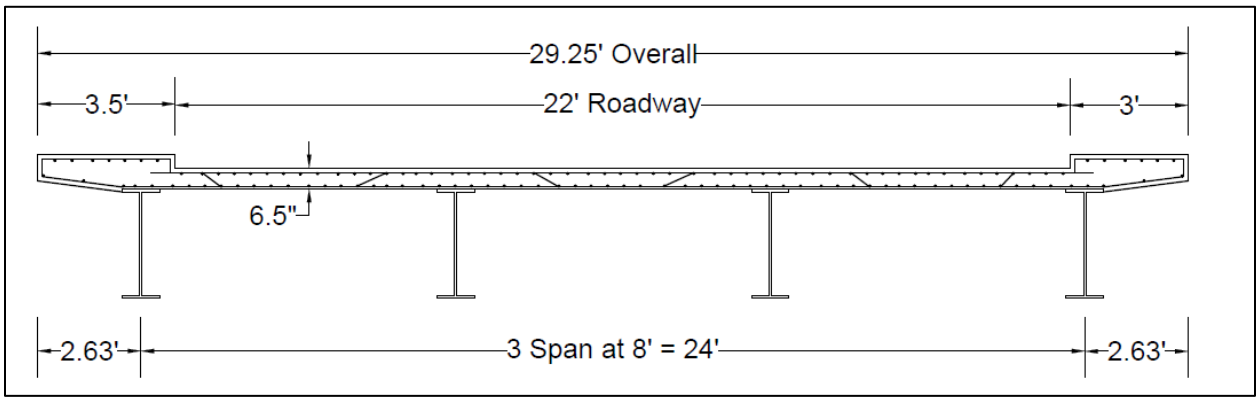

(b)

Figure 3- 4 As-built drawing: (a) Steel framing plan of Spans 1, 2, and 3; (b) Cross-section at mid-span.

The steel girder of the North Bound (NB) bridge was damaged due to traffic impact on November 29, 2017. So, NB bridge was selected for non-destructive evaluation (NDE).

Chapter 4

DIAGNOSTIC LOAD TEST

The load test was performed in November 2018. Strain gages and rotational tiltmeters were used to record the strain data and measure end rotation of the steel girders, respectively.

4.1 Testing Equipment

The equipment used during the diagnostic load test is described in the following subsection.

4.1.1 Strain Gage

Resistance based foil strain gages were used for experimental load testing. A shorter gage length is preferable for steel because of its homogenous nature whereas longer strain gage is preferred for concrete to cover a larger area because of its non-homogenous nature. The strain values were calculated by taking the average strain over the gage length. The Tokyo-Sokki WFLA-6-11-3LDBB strain gage, with a gage length of 0.24 in. and a resistance of 119 Ω, was used to measure steel strain. The strain gage additionally had weather coating. The installation process of strain gages on the steel surface was as follows:

- The gage locations were marked on the inner steel surfaces.
- The steel surface was made smooth by sanding or grinding.
- The area was cleaned by acetone to remove dirt, dust, and other particles. Water was used to clean off the acetone.
- Gages were attached to the steel with CN adhesive (Figure 4-1).
- The wires were run along the inside surfaces of the bottom flanges of the girders and placed on top of the piers.
- In order to secure the wires to the steel surface, a strong setting liquid nail was used.

Figure 4- 1 Strain gage on the steel girder

4.1.2 Data Acquisition (DAQ) Equipment

The Tokyo Sokki DS 50A data logger with 40 channels was used for recording the strain data during the test. Then, a broadband wire was used to transfer data from DAQ to the computer. The data was recorded at a rate of 10 Hz. All the strain gauges were connected to the data logger using calibration factors for each gage (Figure 4-2). The equipment was grounded against electrical interference.

Figure 4- 2 Data acquisition system

4.1.3 Rotational Tiltmeter:

The tiltmeter is an electrolytic tilt sensor and can be used to measure end rotation. Tiltmeters are less sensitive to vibration as a result they are preferable for high-frequency responses. Figure 4-3 shows a typical rotational tiltmeter.

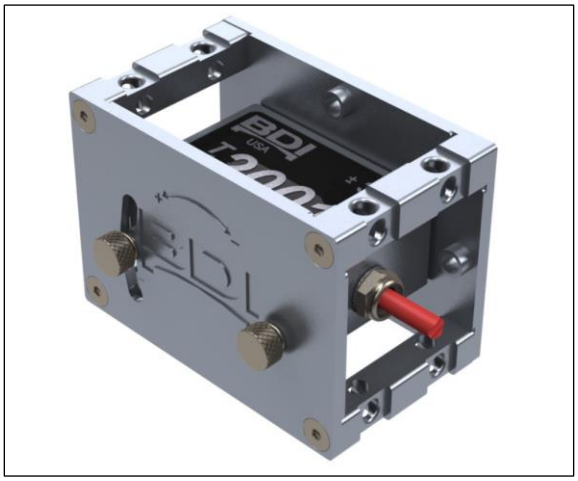

Figure 4- 3 Rotational Tiltmeter

The installation process of the rotational tiltmeter on the steel surface was as follows:

- The tiltmeter locations were marked on the steel surface.
- The steel surface was made smooth by sanding or grinding.
- Strong setting epoxy was used to attach the tiltmeters to the bottom center of the girders.

4.1.4 STS-Wi-Fi Nodes and Base Station

Tiltmeters were connected to STS Wi-Fi node through the wire. Each node can hold up to four tiltmeters. Figure 4-4a shows a typical STS node. STS nodes transferred data through Wi-Fi to the STS Wi-Fi Mobile Base Station (Figure 4-4b),a wireless rechargeable station. A broadband wire was used to transfer data from the STS-Wi-Fi Mobile Base Station to the computer. Figure 4-5 presents the entire Wi-fi network system for tiltmeters. Each node and tiltmeter has a unique identification number, so the software can recognize which tiltmeters are synchronized with which node and which nodes are synchronized to the base station. The rotation responses from the test were collected using a base station at a rate of 10 Hz.

(a) (b)

Figure 4- 4 Components of STS Wi-fi system: (a) STS Node (capacity-4 tiltmeters); (b) STS Wi-Fi mobile base station

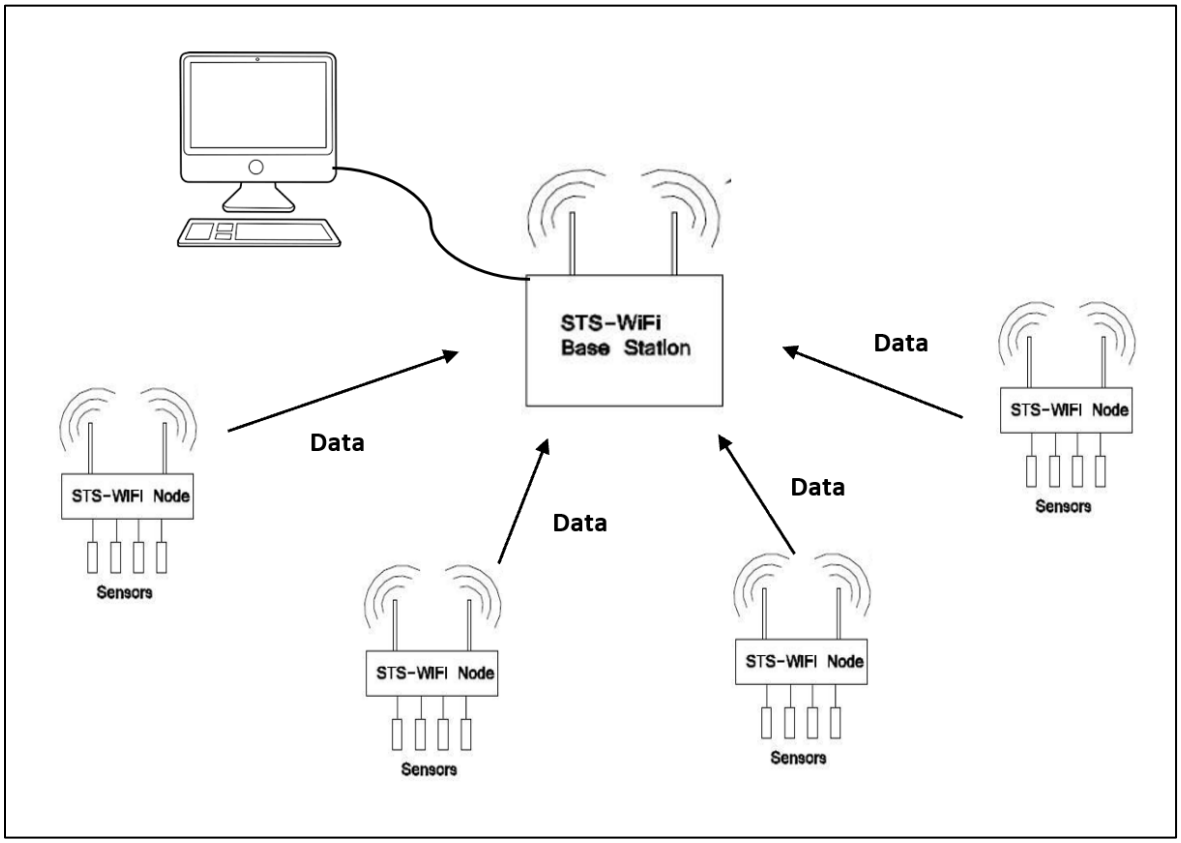

Figure 4- 5 STS Wi-Fi network setup (BDI 2010)

4.2 Instrumentation Plan

The objective of the load test was to evaluate the composite action between the girders and deck, measure the load capacity of the bridge by conducting a load rating. Moreover, the focus of the test was to observe the behavior of damaged girder and undamaged girders.

A detailed plan was prepared for the instrumentation and static load testing of the bridge. Spans 2 and 3 were selected for the load test to optimize instrumentation. Only the superstructure behavior was investigated herein. The exterior girder (west side) was severely damaged.

Instrumentation of the bridge was carried out from 22nd October 2018 to 29th October 2018. A total of 28 strain gages were installed in different critical locations along the steel girders to evaluate the overall behavior of the bridge. Most of the gauges were installed in a pair to record the compression and tension response and evaluate the neutral axis of the beam. Both the spans (Spans 2 and 3) of the bridge were instrumented with strain gages. Gages were attached on the mid-span at the maximum moment region as well as near supports at the negative moment region of the continuous beam. The strain gage, tiltmeter, and the automated data acquisition system (DAQ) locations are shown in Figure 4-6.

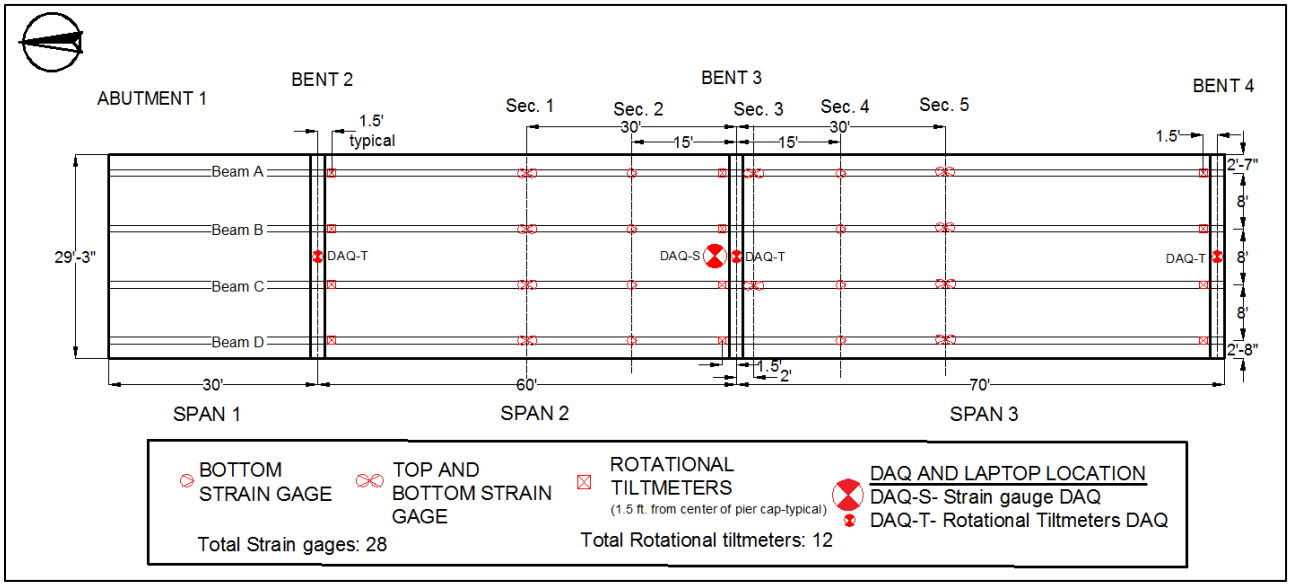

Figure 4- 6 Instrumentation plan for load testing

Girders A, B, C, and D were instrumented with both top and bottom strain gages to determine the actual location of the neutral axis. The bottom strain gages were installed on the top surface of the bottom flange, and the top gages were installed on the bottom surface of the top flange. The strain gage attachment is shown in Figure 4-7. The instrumentation was done in five different sections along the length of the girders. The layout of strain gauge locations in different sections on the bridge can be seen in Figure 4-6. The DAQ was placed on the middle of the bridge under Bent 3 (Figure 4-6). All strain gage wires were run along the length of the girders to the middle of Bent 3 where they were connected to the DAQ. Rotational tiltmeters were installed 2 ft. from the center of the bent cap, as shown in Figure 4-8. The wireless STS-Wi-Fi nodes for the rotational tiltmeters were installed on the top of Bent 2, Bent 3, and Bent 4. All instrumentation was done with the assistance of a towable boom lift, as shown in Figure 4-9.

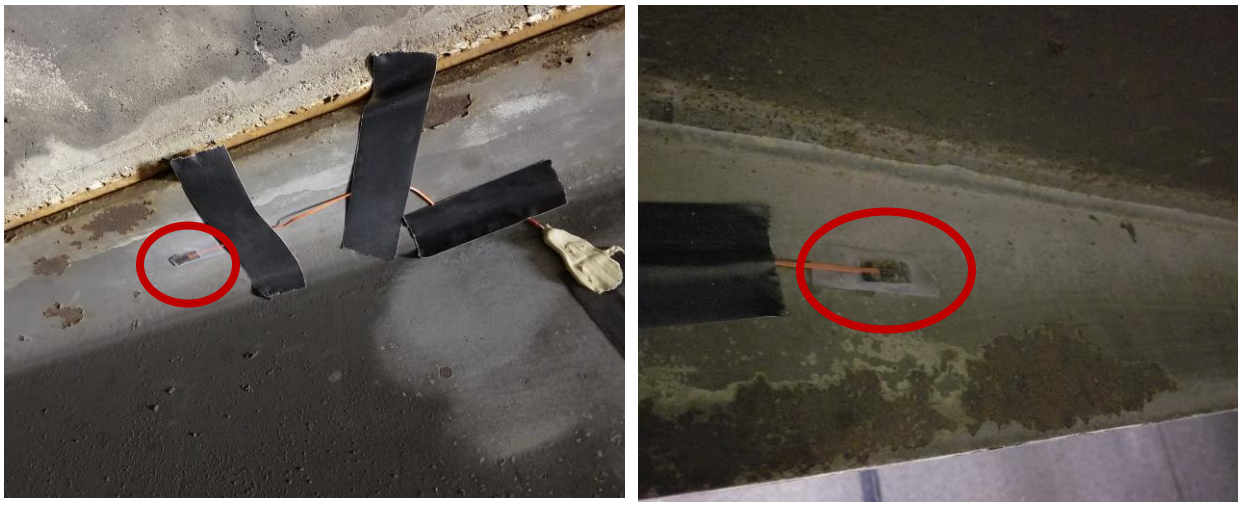

(a) (b)

Figure 4- 7 Attachment of strain gage on steel surface: (a) Bottom surface of the top flange; (b) Top surface of the bottom flange

Figure 4- 8 Rotational tiltmeters at Bent 2

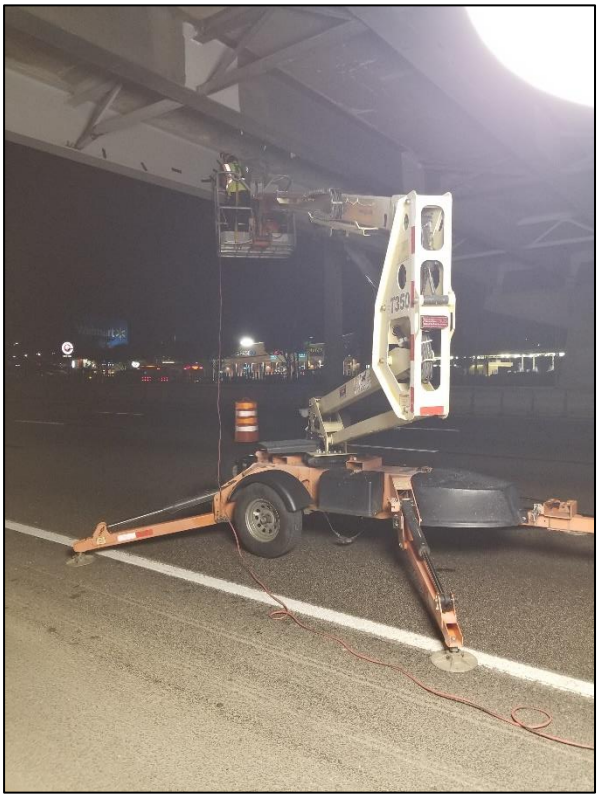

Figure 4- 9 Towable boom lift used for instrumentation

4.3 Testing Vehicle

A static load test was performed on spans 2 and 3 of the bridge. Two identical loaded dump trucks, Truck A and Truck B, were used for this purpose. Both trucks were two tandem three-axle dump trucks that were filled with water and weighed prior to the load test. The distance between the front and the first back wheel axle was 14 ft. while the distance between the two back wheel axles was 4.5 ft. The dimensions of the trucks are shown in Figure 4-10, and the weights of each axle are shown in Table 4-1.

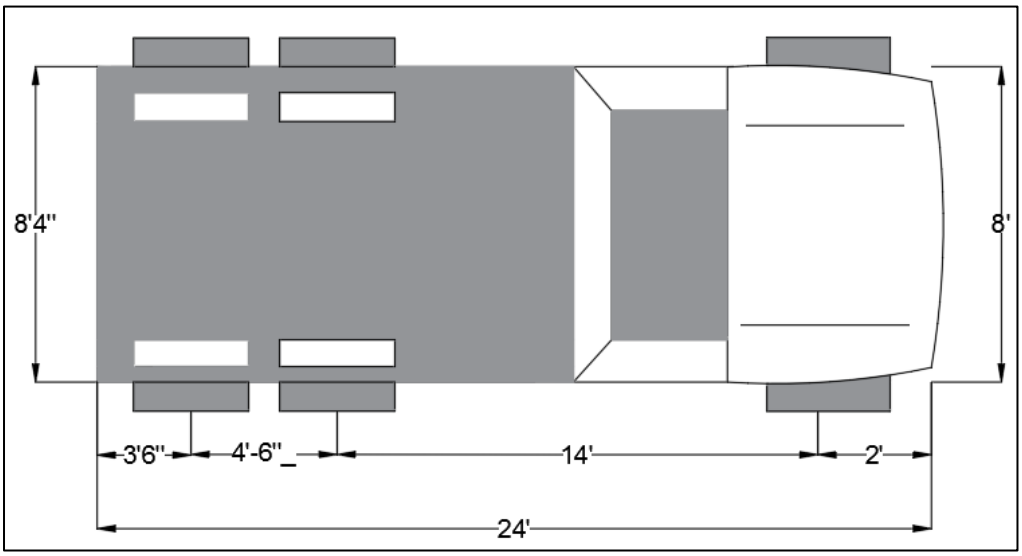

Figure 4- 10 Dimension of the test trucks

Table 4- 1 Truck axle weights for load test

Weights	Truck A (kip)	Truck B (kip)
Gross vehicle weight (GVW)	33.78	33.16
Axle 1(Front) weight	10.6	10.24
Axle 2(Middle) weight	11.59	11.46
Axle 3(Rear) weight	11.59	11.46

4.4 Load Testing Procedure

Marking on top of the bridge was made on the night of the load testing (4th November 2018). The start of the bridge, end of the bridge, and intermediate span locations were marked. The paths for the truck were also marked on the same night using spray paint. Two types of static load tests were performed for the project-crawl speed test and stop location test. Figure 4-11 shows different paths for the crawl speed test and stop location test. Path P1, Path P2, and Path P3 the denote crawl speed test while Path P4 shows the stop location test.

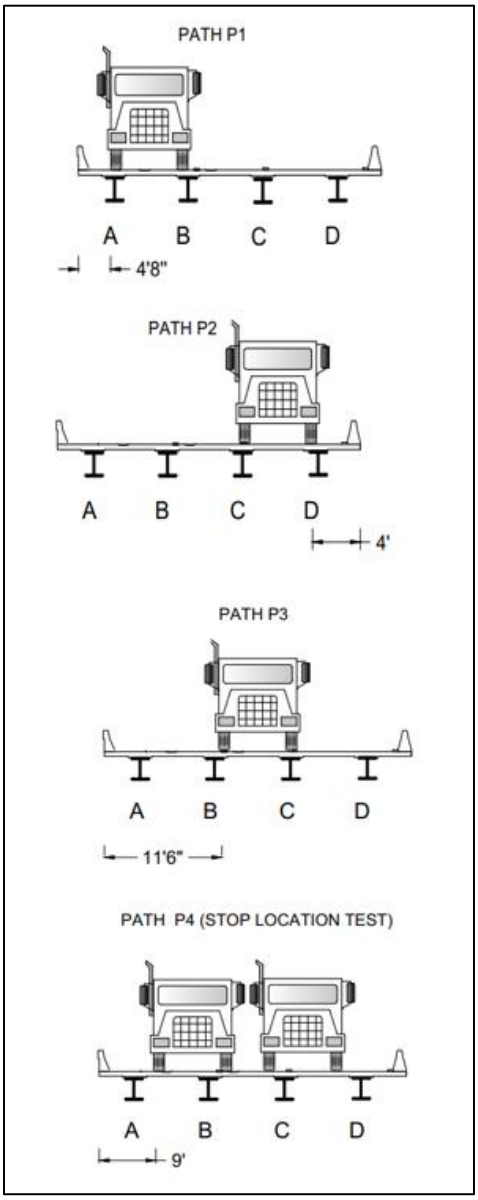

Figure 4- 11 Load test paths

Path P1 and Path P2 were selected based on the desired maximum response on the exterior girders, A and D, respectively, whereas Path P3 was chosen to get the maximum response of the interior girders B and C.

Crawl speed tests were carried out where the trucks moved at a constant speed of 5 mph in three predetermined paths. The truck's speed was kept low to prevent the effects of vibration-induced during the load test. The lower speed also helps to prevent dynamic effects on the bridge. The tests were repeated for each path (Run 1 and Run 2) to verify the accuracy of the data. The truck started from the mid-span of span 4 and went up to mid-span of span 1. Figure 4-12a shows the load test path P2 during the experimental load test, and Figure 4-12b presents the Path P3.

(a)

(b)

Figure 4- 12 Load test path: (a) Path P2; (b) Path P3 (crawl speed test)

For the stop location test, the trucks were stopped at a predetermined location (mid-span) on the bridge for observation of the responses of the bridge. The stop locations were specifically chosen so the vehicles could produce the maximum moment on the bridge girders. The trucks were moved along the paths and made stops at the specified stop location for 20 seconds so that the reading could be taken, and no dynamic effects were induced (AASHTO MBE 2018). Figure 4-13 shows dump trucks during the stop location test.

Figure 4- 13 Dump truck on Path P4 (stop location test)

Chapter 5

NON-DESTRUCTIVE EVALUATION (NDE)

5.1 NDE Equipment

The following equipment was used for the Non-Destructive Evaluation (NDE):

1. Ground Penetrating Radar (GPR)
2. Impact Echo (IE)

5.1.1 Ground Penetrating Radar (GPR)

Antennae with higher frequency (e.g., 2.6 GHz) was used for low depth analysis (0-12 in.), while lower frequency (e.g., 270 MHz) was used for higher depth evaluation (0-18 ft.). Figures 5-2a and 5-2b show a truck-mounted GPR and 2.6 GHz antenna with a hand scanner, respectively.

(a)

(b)

Figure 5- 1 Ground penetrating radar (GPR): (a) truck mounted GPR; (b) 2.6 GHz antenna

Cart-Mounted GPR

A GSSI SIR-30 brand GPR was utilized herein. The cart mounted GPR with a single 2.6 GHz antenna was used (Figure 5-2) in order to gain a more precise reading of the deck. Pushing the cart at a speed of less than 3 mph while using a high-frequency antenna resulted in higher resolution images than the truck-mounted option. This method is preferred for shorter spans to increase the quality of the scans.

Figure 5- 2 Cart-mounted GPR

5.1.2 Impact Echo (IE) Device

Unlike the GPR, Impact Echo (IE) is a spot scanning device used to scan discrete data points in a pre-determined grid on concrete deck surfaces. Figure 5-3 shows the Impact Echo device that was used in the study.

Figure 5- 3 IE Device

5.2 NDE Procedure

- First, traffic on top of the bridge was closed to facilitate the NDE work on Spans 2 and 3.
- Square grids measuring 2 ft. spacing were marked on the deck surface for both the IE and GPR scans. For GPR scanning, parallel grid lines spaced at 2 ft. were used. For IE scanning, square grids with 2 ft. spacing were used.
- IE and GPR were used to scan the top of the bridge deck along the grid lines. IE scan was taken at each grid point individually, while the GPR scan was performed by line scanning using the cart mount (with one 2.6 GHz antenna, as shown in Figure 5-4).
- Scanning was performed over one full day, 22nd October, 2018. Lanes 1s and 2s (Figure 3-3) on Spans 2 and 3 were accordingly scanned.
- The data were analyzed according to the grid locations to test for any cover variations and possible delamination.

Figure 5- 4 Scanning with Cart-Mounted GPR and IE.

5.2.1 GPR Scanning

GPR scanning was performed in parallel lines every 2 ft. in the direction of traffic. Figure 5-5 shows the GPR scanning grids and the directions of scanning.

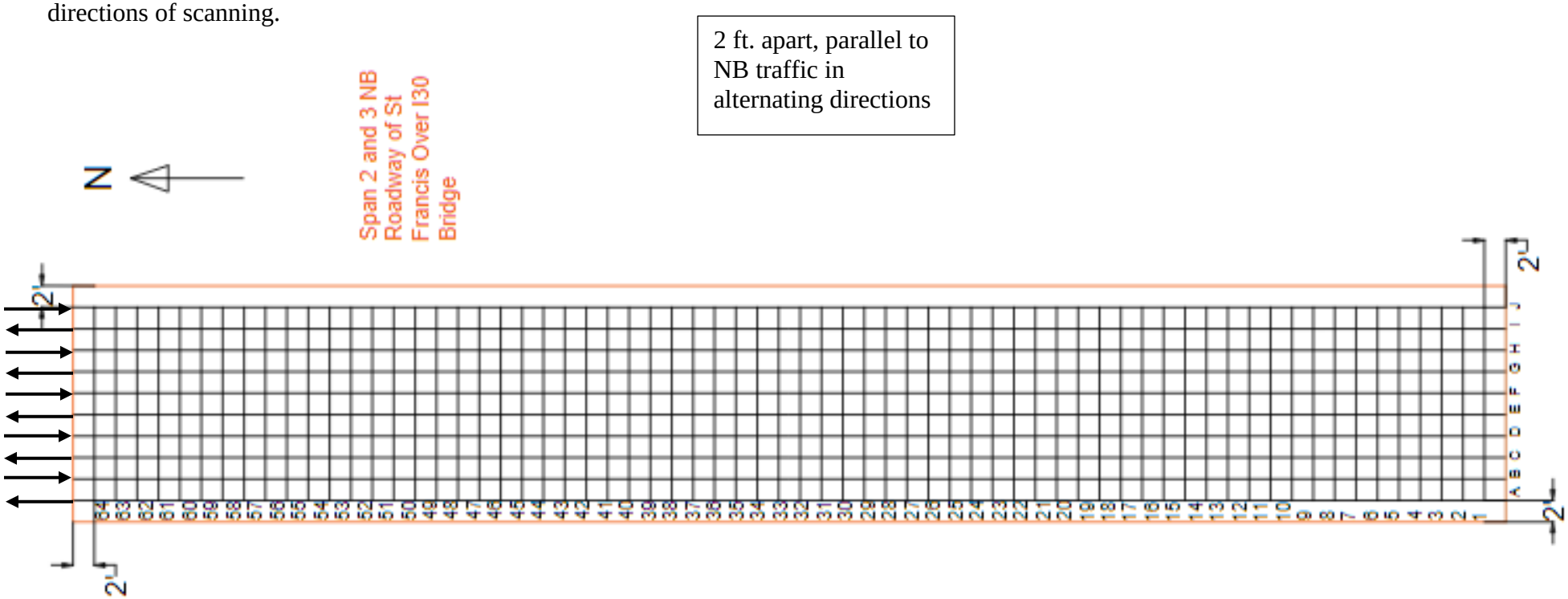

Figure 5- 5 GPR scanning grids

5.2.2 IE Scanning

The Impact Echo (IE) device measured the possible presence of delamination by creating an impact on the bridge deck surface. The IE data were collected at discrete points on a pre-selected 2 ft. spaced grid pattern. Results of the IE data are valid for delamination deeper than 4 in. within the surface. IE data was taken at each point to provide the state of delamination. The IE scanning grid with the data points is shown in Figure 5-6.

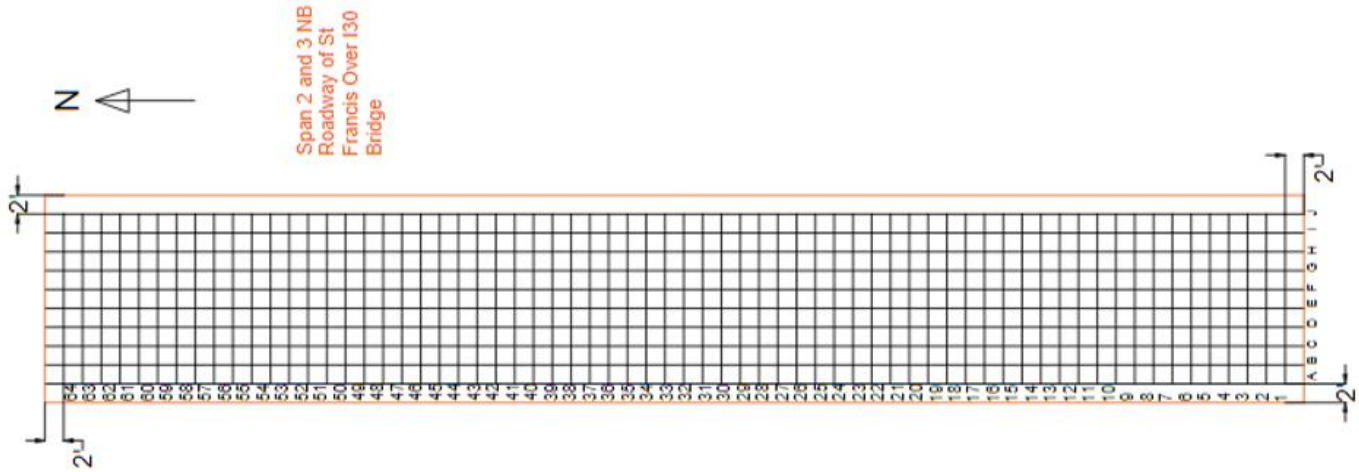

Figure 5- 6 Working grid for IE scanning

Chapter 6

FINITE ELEMENT MODELING

A Finite Element Model (FEM) of the entire St. Francis bridge NB was created in ABAQUS CAE (ABAQUS 2017) to simulate the overall response of the bridge under live loading. Few assumptions were made to simplify the model and reduce computational time.

6.1 Material properties

6.1.1 Concrete

The deck concrete was designated a Class A (3000 psi). To model the behavior of concrete, there are numerous constitutive models available including, the smeared crack model and the plastic damage model, which are the two most commonly used methods. In the present study, a concrete damage plasticity model was used to define concrete compressive and tensile properties. The CDP model is based on the suggested envelope curve by Carreira and Chu (1985). The model assumes that concrete has two failure modes: compressive crushing and tensile cracking. The response of concrete in compression is shown in Figure 6-1. The general equation of compressive stress is expressed by

$$\sigma_c = \frac{f'_c\,\gamma(\varepsilon_c/\varepsilon'_c)}{\gamma-1+(\varepsilon_c/\varepsilon'_c)^{\gamma}} \qquad (6\text{-}1)$$

where:

σ_c = compressive stress

ε_c = compressive strain

f'_c = concrete compressive strength

ε'_c = corresponding strain

γ is a parameter that depends on the stress-strain diagram shape and is expressed as follows:

$\gamma = \gamma_1 = [1.02 - 1.17\,(E_t / E_c)]^{-0.74}$ if $\varepsilon_c \le \varepsilon'_c$ (6-2)

$\gamma = \gamma_2 = \gamma_1 + (a + 28b)$ if $\varepsilon_c \ge \varepsilon'_c$ (6-3)

where:

$a = 3.5\ [12.4 - 0.0166\ f'_c]^{-0.46}$ (6-4)

$b = 0.83 \exp\left(\frac{-911}{f'_c}\right)$ (6-5)

$E_t = \frac{f'_c}{\varepsilon'_c}$ (6-6)

$E_c = 3320\ \sqrt{f'_c} + 6900$ (6-7)

As for the tension behavior, the stress-strain response (Figure 6-2) is assumed to be linear under uniaxial loading until concrete cracking. the behavior is subsequently assumed to be perfectly plastic as expressed in the following equation:

$$\sigma_t = \frac{f_t\ \beta(\varepsilon_t/\varepsilon'_t)}{\beta - 1 + (\varepsilon_t/\varepsilon'_t)^{\beta}} \quad (6\text{-}8)$$

where:

σ_t = tensile stress

ε_c =tensile strain

f_t = concrete tensile strength

ε'_c = corresponding strain

β is a parameter that depends on the stress-strain diagram shape and is expressed by:

$$\beta = \frac{1}{1 - (f_t\ /(\varepsilon'_t E_t)} \quad (6\text{-}9)$$

where:

Et = initial tangent modulus.

The CDP parameters were set as follow: Dilation Angle of 350, eccentricity of 0.1, fb0/fc0= 1.16, K = 0.667 and the viscosity parameter was 0.01. The mass density was set at 2.4 X 10-9 kg/mm3 with Poisson's ratio of 0.15.

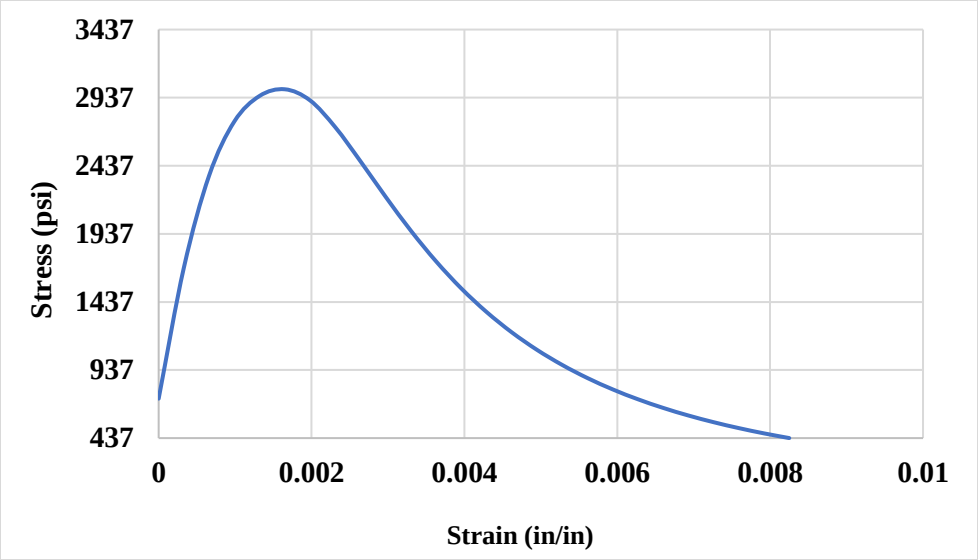

Figure 6- 1 Compression stress-strain relationship for concrete

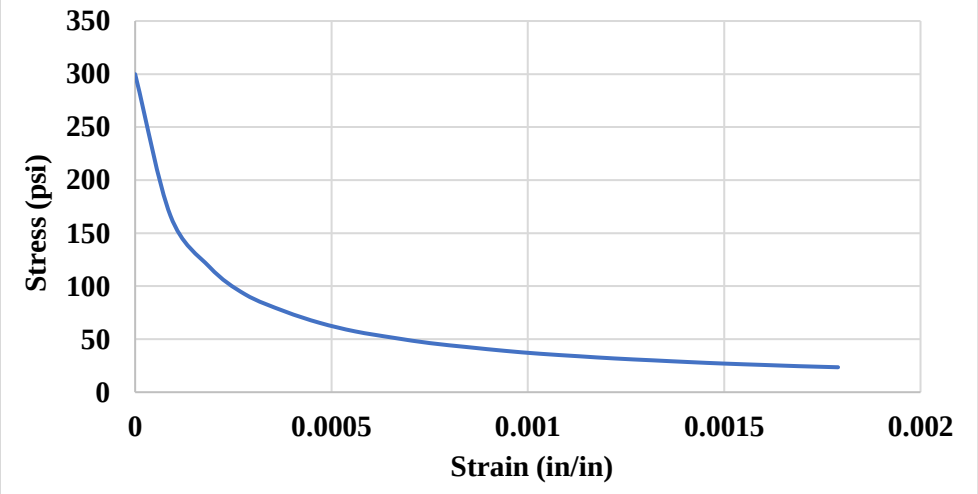

Figure 6- 2 Tensile stress-strain relationship for concrete

6.1.2 Reinforcing steel

Elastic-perfectly plastic material was used to define the steel rebar with an equal behavior in tension and compression (Figure 6-3) where the steel initially showed elastic behavior up to the yield point (f_y); a further yielding then occurred until fracture. A mechanical elastic isotropic behavior was set with Young's Modulus of 29,000,000 psi and Poisson's ratio of 0.3. Additionally, a mechanical plastic isotropic behavior was set with a yield stress of 40,000 psi at zero plastic strain.

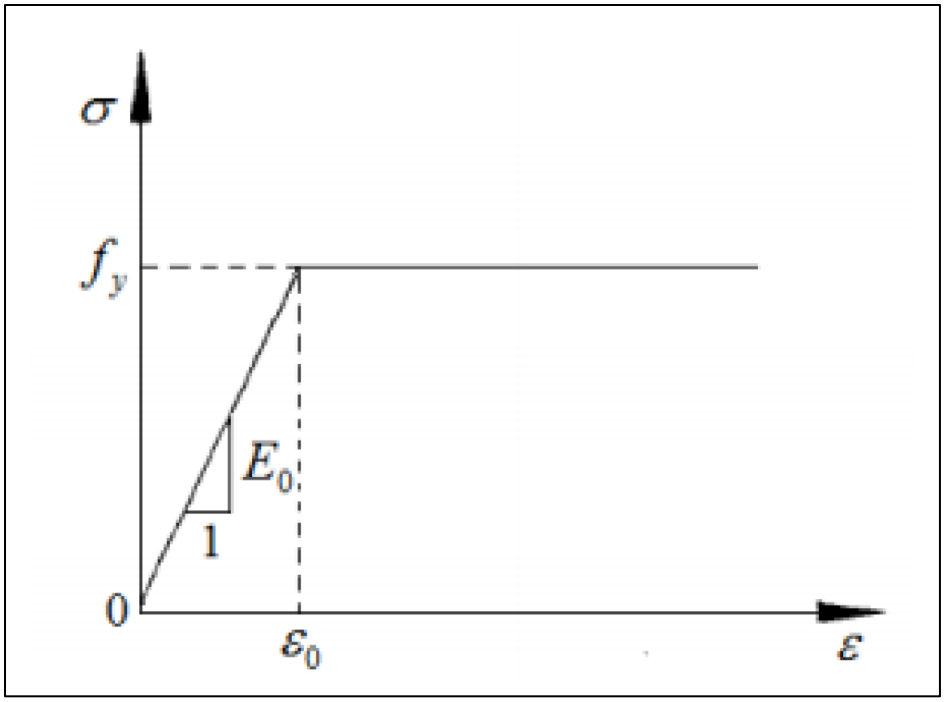

Figure 6- 3 Elastic- Perfectly plastic model

6.1.3 Structural Steel (Steel Girder)

The similar elastic-perfectly plastic material was considered to define the steel properties of the girder. Young's Modulus and Poison's ratio was considered as 29000,000 psi and 0.3, respectively. A mechanical plastic isotropic behavior was moreover set with a yield stress of 33000 psi at zero plastic strain.

6.2 Bridge Model

The numerical analysis of the bridge was conducted to establish a calibrated bridge model that represents the on-site bridge's geometry, condition, and in-service condition. The base model was created in ABAQUS using the original geometric and boundary conditions. Interactions were also taken from as-built drawings.

6.2.1 Element types

The element selected for the deck, girders, barrier, and patch area (application of live load) of the model was 8-node brick element. ABAQUS uses C3D8R brick element, which incorporate reduced integration and hourglass control along with translational degrees of freedom in three global directions of each node. Concrete and structural steel was modeled using C3D8R element. A 2-node linear three-dimensional truss element (T3D2) was then used to reinforce the steel. An FRP was modeled as finite membrane strain (SC8R) shell elements, as the dimension of one direction and the thickness, is significantly larger than the other dimensions. Figure 6-4 shows the different types of elements in ABAQUS CAE.

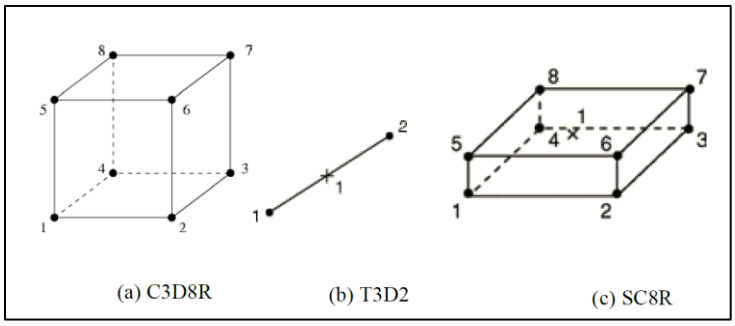

Figure 6- 4 Element types

6.2.2. Model Assembly and Type of Analysis

The bridge components were assembled to create a model similar to real bridge structures. Figure 6-5 shows the model assembly. The rebar layout is shown in Figure 6-6. A static-general step was created in order to start the analysis with the default time period of 1, initial increment size of 0.001, minimum of 1E-08, and maximum of 1. The default ABAQUS solver with default incrementation was also employed.

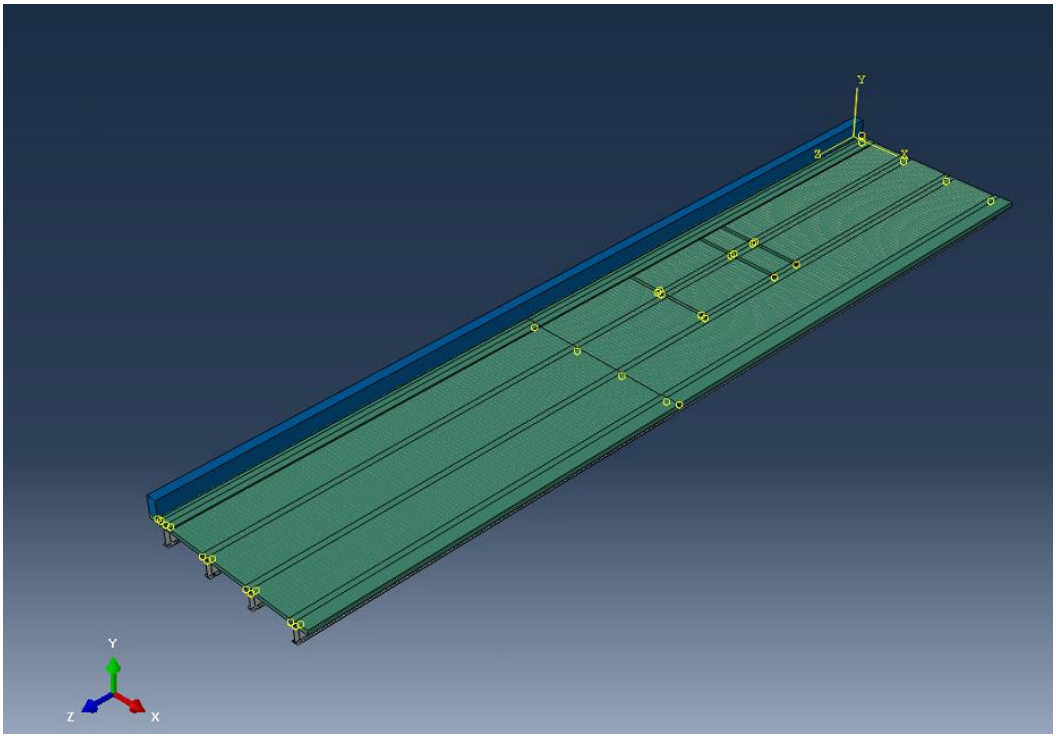

Figure 6- 5 Bridge assembly

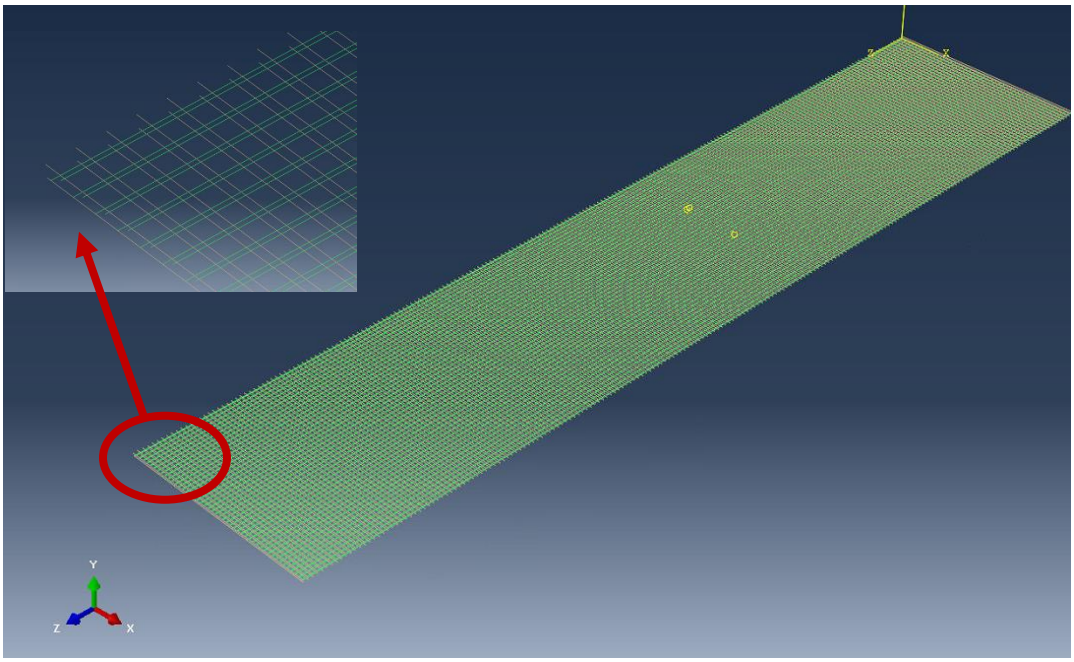

Figure 6- 6 Orientation of rebars in the cast in place deck

6.2.3 Constraints and Interaction

After assembling the components, interactions between the element surfaces were applied. Different surface-to-surface contacts were used to ensure a realistic model that captures the actual behavior of the bridge as follows:

i) Surface-to-surface tie constraints were used to connect the concrete deck and barrier to replicate the monolithic connection.

ii) Cohesive contact properties were used to model the non-composite concrete deck over steel girders. Small sliding was allowed between the two surfaces.

iii) All the rebars were also modeled as truss elements and embedded into the deck cross-section.

6.2.4 Meshing of Parts

Proper meshing and the element selection are an essential part of FEM to ensure a balance between convergence, the accuracy of the model, and run time. To mesh each component, the ABAQUS software package was used. AASHTO recommended that the aspect ratio of the finite element and grid panels not exceed 5.0. Partitioning was effectively applied to achieve uniform meshing and uniform nodes distribution in the bridge components, especially the parts that were in contact. The concrete deck, steel girder, and rebars were meshed with element size 6 in. while the patch area (patch load) was 2 in. mesh size.

6.2.5 Boundary Conditions and Loads

All three supports of continuous Spans 2 and 3 were considered as pinned/hinged support. In the model, all the supports were treated as pins with the restriction of the vertical and horizontal displacement.

The live load from the truck wheels were applied as patch loads. AASHTO LRFD (2017) suggests that the wheel load can be approximated for distribution over the area of the wheel contact surface. The wheel contact surface was calculated to be 6 in. based on the pressure of the tires, the radius of tires, and the total load of the truck. The width of the tires was measured at10 in. The load was applied through a planer surface with a thickness of1 in. and the same material properties as the deck. The wheel load is shown in Figure 6-7.

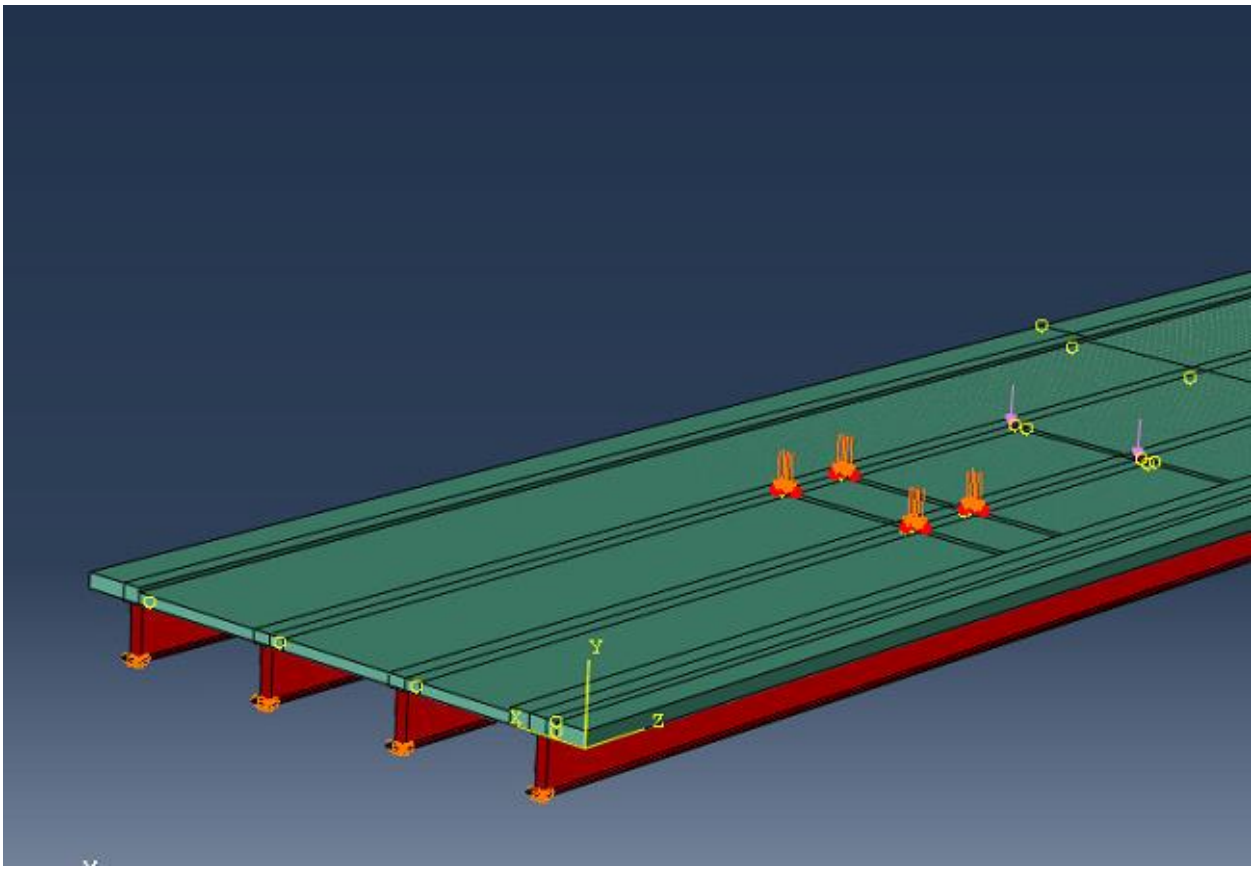

Figure 6- 7 Patch loads in ABAQUS interface

6.2.6 Mesh Sensitivity Analysis

To achieve confidence in the modeling output a mesh refinement study was performed to identify acceptable mesh size. Richardson's extrapolation equation was used to identify standard mesh size. The extrapolation equation is shown in Eq. 6-10

$$\Phi_\infty = \frac{\Phi_1 h_2^q - \Phi_2 h_1^q}{h_2^q - h_1^q} \quad (6\text{-}10)$$

Where:

$\phi\infty$ = Quantity from infinite mesh

ϕ_1 = Quantity of stress or deflection from 1st mesh

h_1 = Characteristic length of 1st mesh = $\sqrt{{M_n}^2 + {M_n}^2}$

ϕ_2 = Quantity of stress or deflection from 2nd mesh

h_2 = Characteristic length of 2nd mesh

Three different mesh size 20 in., 10 in., and 6 in. was selected for this analysis. The size of the mesh represents length of one side of each element. Deflection (φ) was plotted against the characteristic length (h) increased to the q power. The value of q was varied until a straight line was plotted against h^q (Figure 6-8).

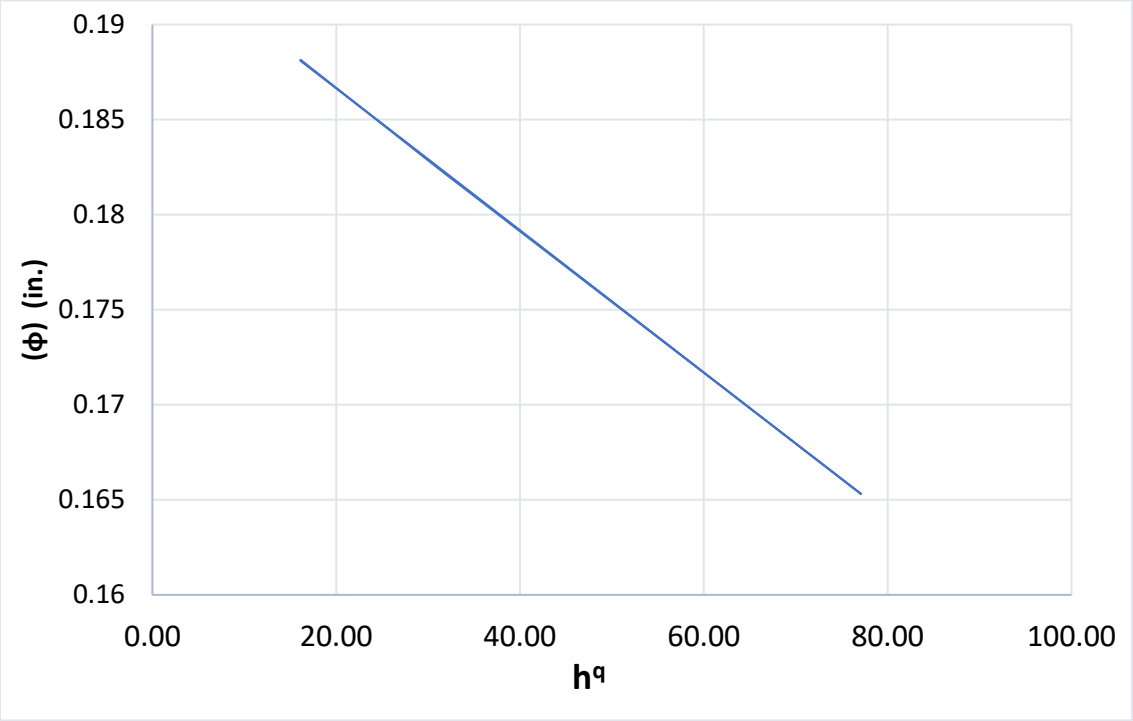

Figure 6- 8 h^q vs. φ plot

To assess the model's correctness, the difference error between the extrapolated displacement and the model with the 6 in. elements was determined. Eq. 6-11 was used to determine the percentage of error.

$$e_2 = \frac{\phi_1 - \phi\infty}{\phi\infty} \text{ X } 100 \qquad (6\text{-}11)$$

where:

e_2 = Error in 2nd mesh

ϕ_1 = Deflection from 2nd mesh

$\phi\infty$ = Deflection from infinite mesh

6 in. elements and an infinitely fine mesh had a 2.5 % error in computed inaccuracy. The model's operating duration would be extended by an additional five hours if its size were further lowered. Consequently, a 6-inch mesh was used for the FEM study because of a time and memory restriction.

6.2.7 Energy Balance

Checking the components of energy balance is necessary to ensure the accuracy in modeling. The most general means of evaluating the accuracy of response in FEA involves studying various model energies. The energy balance equation in ABAQUS (2014) is shown in equation 6-12.

$$E_I+E_V+E_{FD}+E_{KE}+E_{IHE}-E_W-E_{PW}-E_{CW}-E_{MW}-E_{HF}= E_{Total}= \text{Constant} \quad (6\text{-}12)$$

Where,

E_I= Internal energy,

E_V= Viscous energy dissipated,

E_{FD}= Frictional energy dissipated,

E_{KE}= Kinetic energy,

E_{IHE}= Internal heat energy,

E_W= Work done by the externally applied force,

E_{PW}= Work done by contact penalties,

E_{CW}= Work done by constraint penalties,

E_{MW}= Work done by propelling added mass,

E_{HF}= External heat energy through external fluxes,

E_{Total}= Total energy.

In the numerical model, the total energy is only approximately constant, generally with an error of less than 1%.

To extract components of Eq. 6-10, a history output request was created. After the successful execution of the history output, components of the energy equation were plotted against time in ABAQUS. Figure 6-9 shows the internal energy (E_I) vs time plot, and Figure 6-10 shows the work done by the externally applied forces (E_W) compared to the time plot in ABAQUS.

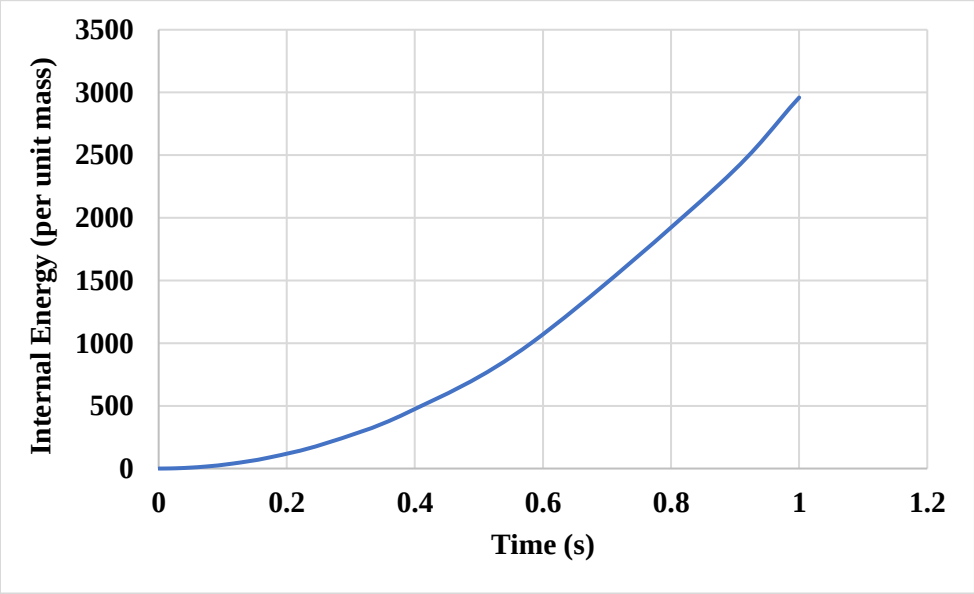

Figure 6- 9 Internal energy (E_I) vs time

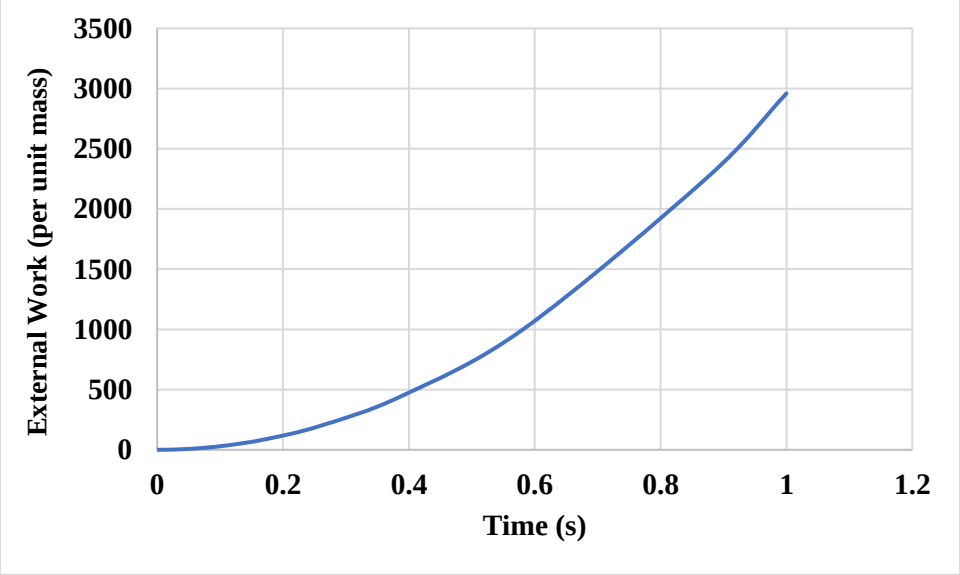

Figure 6- 10 Work done by the externally applied forces (E_W)

E_{PW} and E_{CW} were zero since the model was not involved with any contact/constraint penalty or propelling added mass. Moreover, E_V, E_{FD}, and E_{KE} were also zero since the model did not have any viscous fluid, frictional co-efficient, or dynamic properties. Figure 6-11 shows the total energy of the whole model (E_{Total}) versus the time plot in ABAQUS.

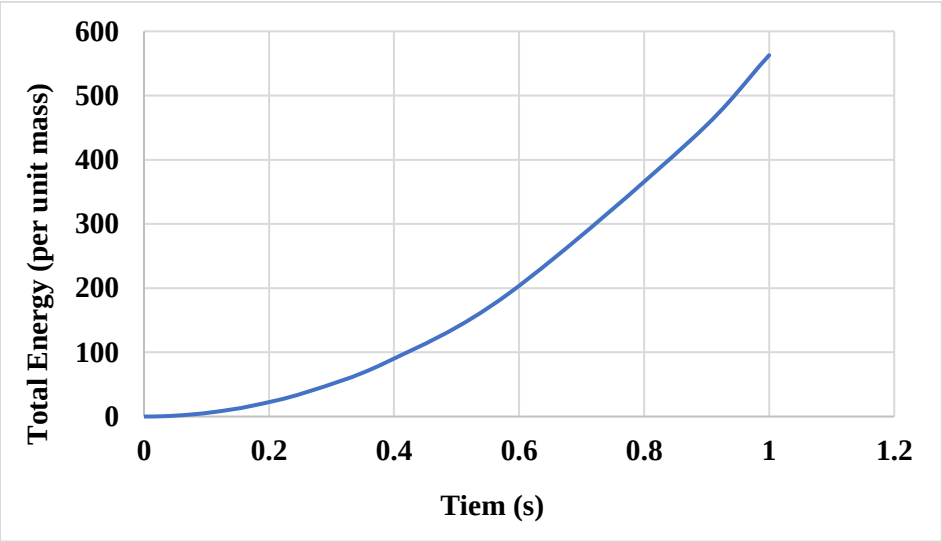

Figure 6- 11 Total energy of the model (E_{Total})

The total energy of the model was greater than 1%. To investigate the cause, all components of the history output were analyzed. The difference between internal and external energy was zero. It was found that the problem was associated with contact constraint discontinuity work (ALLCCDW). The numerical output of the ALLCCDW was the same as the total energy's numerical output, but with opposite signs. Figure 6-12 presents the ALLCCDW plot.

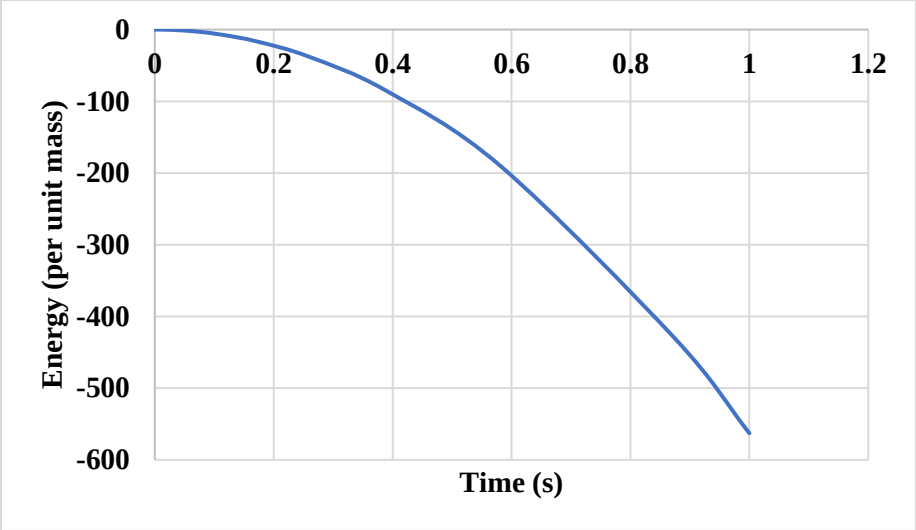

Figure 6- 12 Constraint discontinuity work

The output variable ALLCCDW accounts for the remaining work done by contact forces (ABAQUS Example Problems Guide 2016). ALLCCDW can be positive or negative, and it may be counterintuitive.

Chapter 7

RESULTS & DISCUSSIONS

7.1 Experimental Results

The strain gage and the rotational tiltmeter data were analyzed to evaluate the load response of the St. Francis bridge. The data obtained from the DAQ was analyzed using Microsoft Excel. Although the readings were balanced to zero before the test, some strain gages responded with a minor initial reading. These initial readings were adjusted to zero by applying an initial offset to all the readings by subtracting the initial readings from all data points. The initial plot of the data showed that the strain and tiltmeter readings started at zero and returned approximately to zero at the end of the test, indicating that the response of the bridge was within linear elastic range, and no non-linearity was observed.

The strain response exhibited little noise and vibration when the trucks passed across the bridge. The strain values were refined by calculating the moving average between 10 data points to remove the noise and vibration in the measured data. The refinement provides one data point for every second, which was accurate enough for all evaluation purposes. Negative strain readings additionally indicate compression while positive strain readings indicate tension.

7.1.1 Strain Responses

The name of strain gages was assigned in a way that the first number denotes the section (1-5), the second letter expresses the girder (A, B, C, and D), and the last letter shows the location (T-top or B-bottom). For example, 1BB expresses the strain response at section 1 of girder B in the bottom flange. Figure 7-1 shows the raw strain responses of girder B at section 1.

Figures 7-2, and 7-3 show the strain versus time history for Run 1 and Run 2, respectively, from Path P1. The trucks were moved across Spans 2 and 3 at a uniform speed. According to Barr et al. (2001) and Gheitasi and Harris (2014), the girder that is directly under the truckload resists the majority of the load, and the load continues to decrease on the girders further away. For the repeated run, the girders showed almost the same responses, which ensure data accuracy and reliability on the load test data.

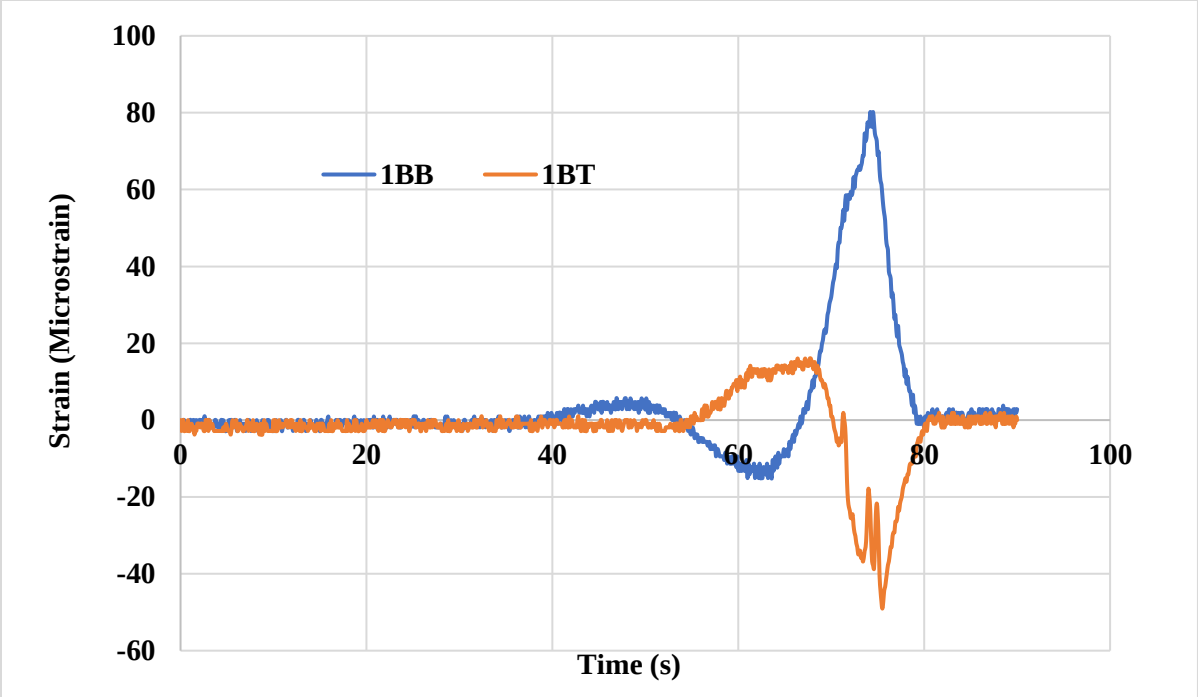

Figure 7- 1 Raw strain data for Path P1 Run 1 (Section 1, Span 2 of Girder B).

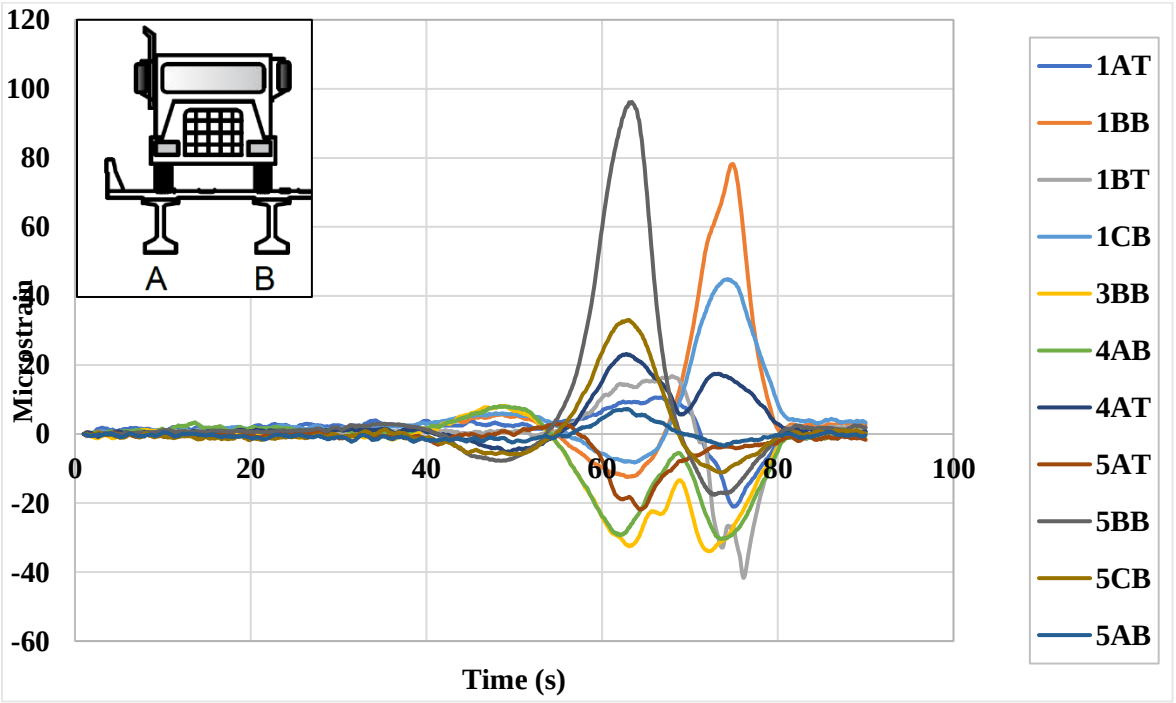

Figure 7- 2 Strain vs time diagram for Path 1 Run 1

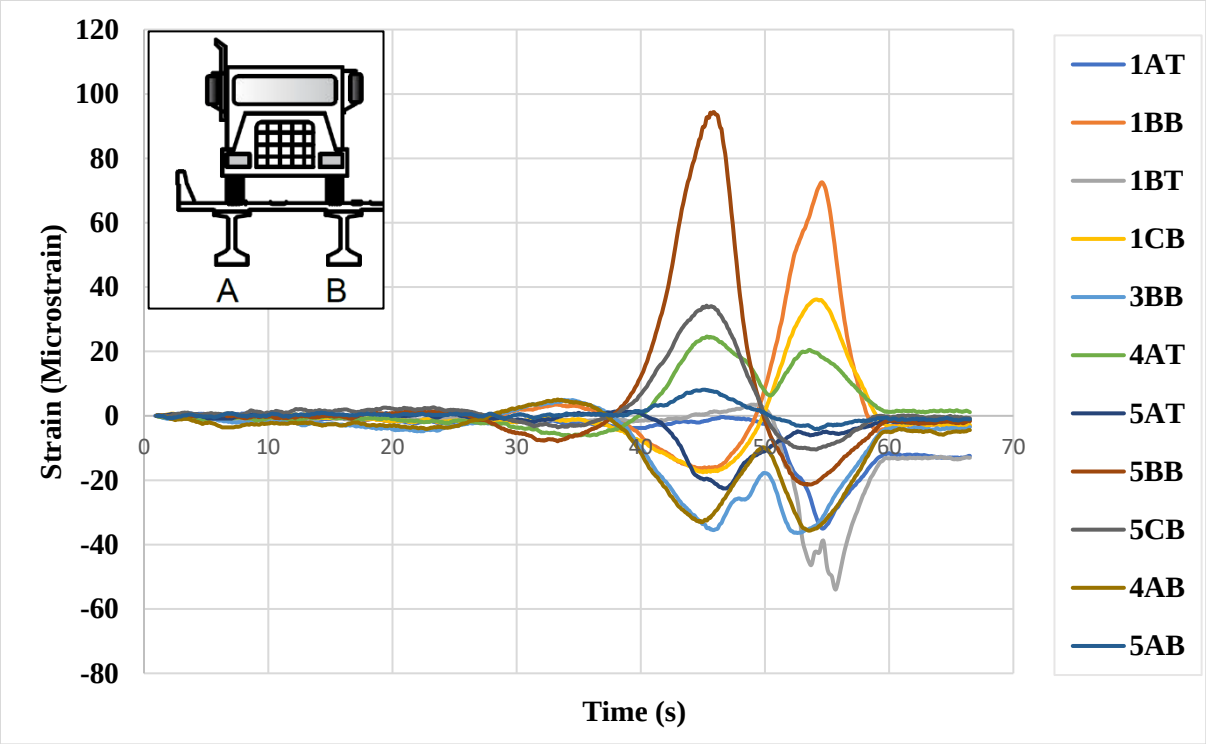

Figure 7- 3 Strain vs Time Diagram for Path 1 Run 2

According to Barr et al. (2001), the response of girders A and B should be higher for Path 1 Run1 and Path 1 Run 2, but the data indicated that the response of girder B was higher than expected while girder A did not respond as expected. Figure 7-4 shows the comparison of strain response of girder A and B at section 1 while Figure 7-5 shows the comparison of strain response of girder A and B at section 5. The peak strain of the damaged and replaced section of girder A is lower compared to the undamaged girders B for Path P1 run R1. The girder A was damaged and repaired and replaced several times in the past. According to TxDOT representative the available heavier section for repairing purposes. As a heavier section was used to repair the damaged portion, the stiffness of the girder may have increased. Another probable cause for lower strain than girder B might be the contact problem or due to the improper contact between the steel girder and concrete deck as there was no composite action (due to friction). In addition, local buckling of the girder in some places was noticed during the load testing, potentially affecting the strain distribution as well.

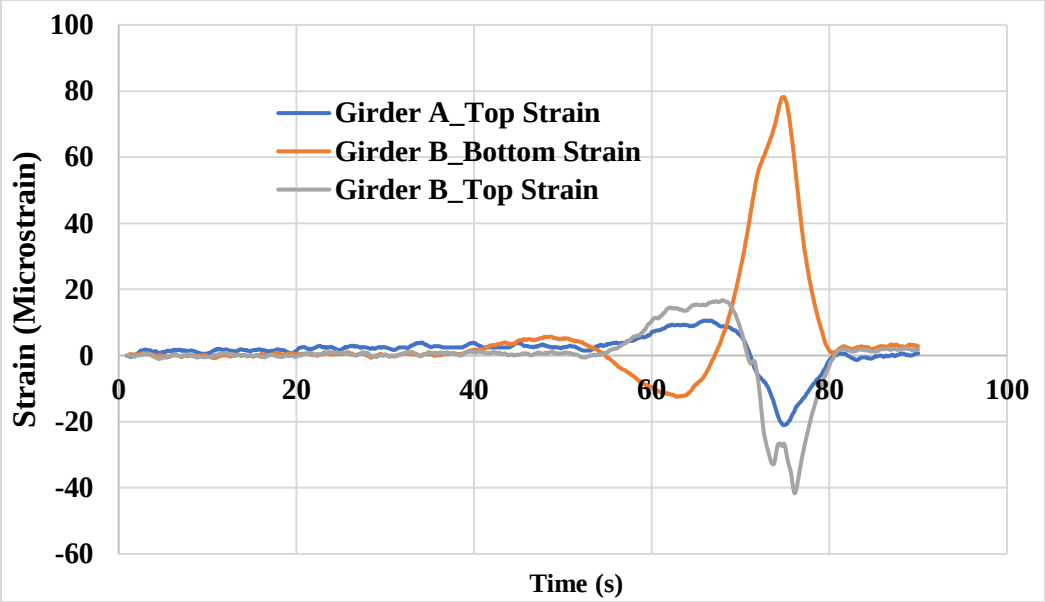

Figure 7- 4 Strain comparison of girder A and B at section 1

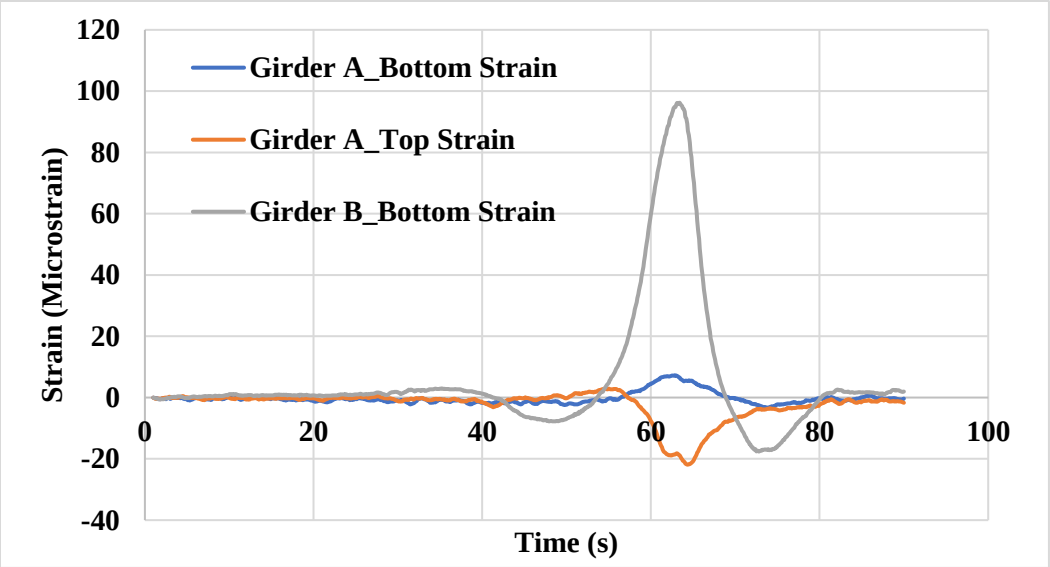

Figure 7- 5 Strain comparison of girder A and B at section 5

Figure 7-6 shows the strain time history for Run 1 from Path P2. The strain responses at girders C and D were maximum, as expected, when the truck was on Path P2. The strain across other girders gradually decreased with distance from the truck tires.

Figure 7-7 presets the strain time history for Run 1 from Path P3. The strain responses at girders B and C were maximum (as expected) when the truck was on Path P3.

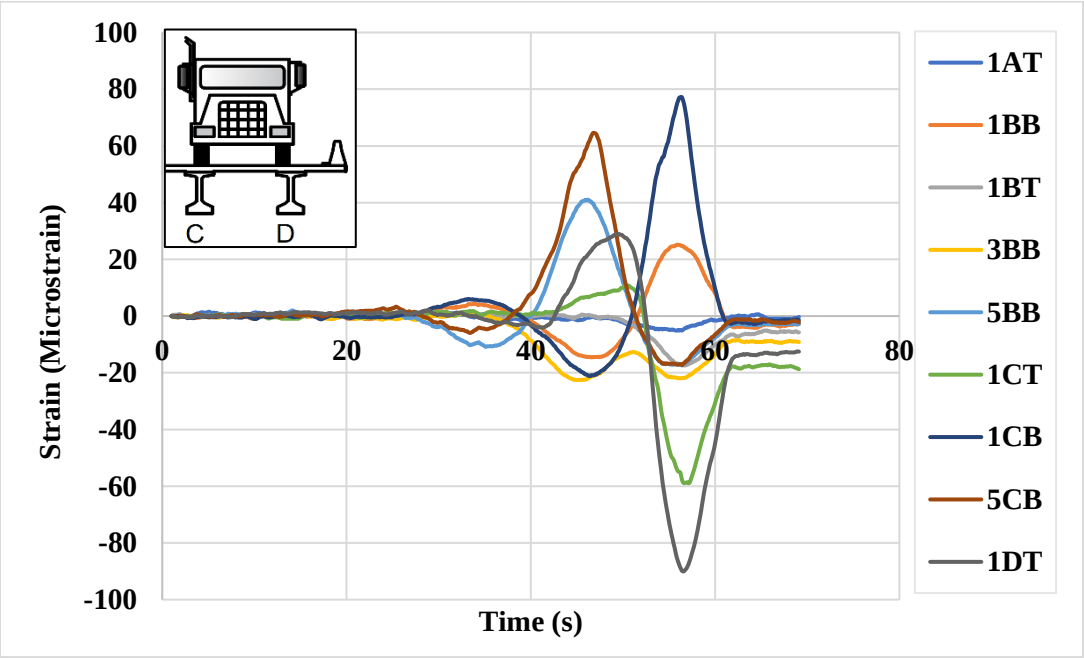

Figure 7- 6 Strain vs time diagram for Path 2 Run 1

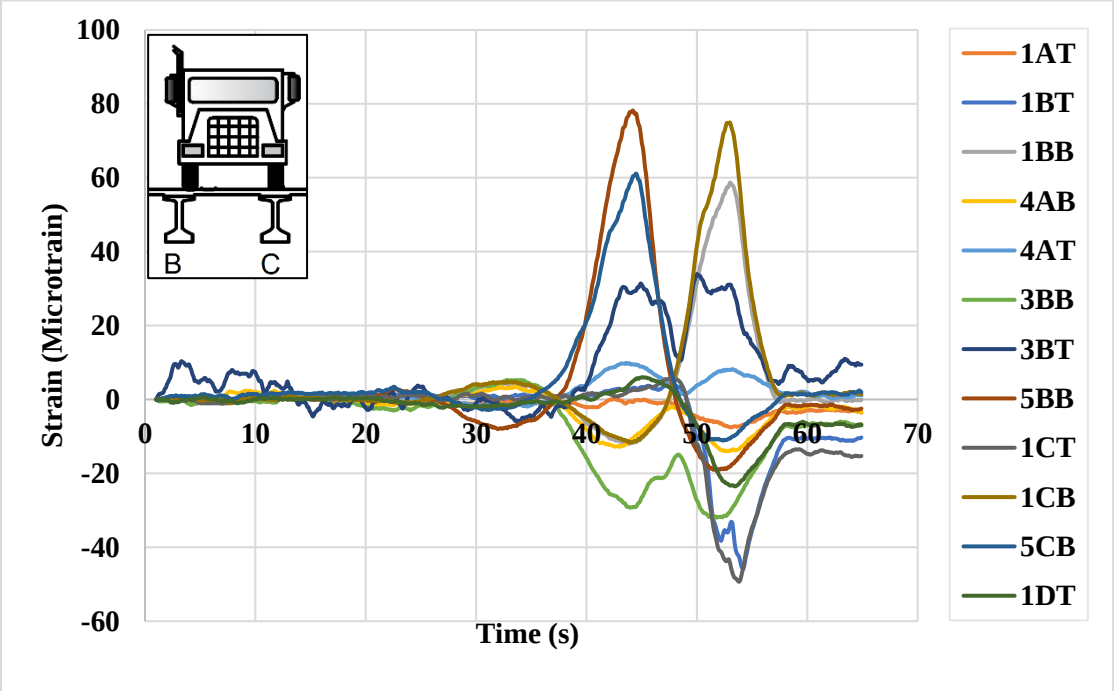

Figure 7- 7 Strain vs time Diagram for Path 3 Run 1

Figure 7-8 shows the stop location test. As both the trucks were used for stopping location, the strain values are higher than other path runs.

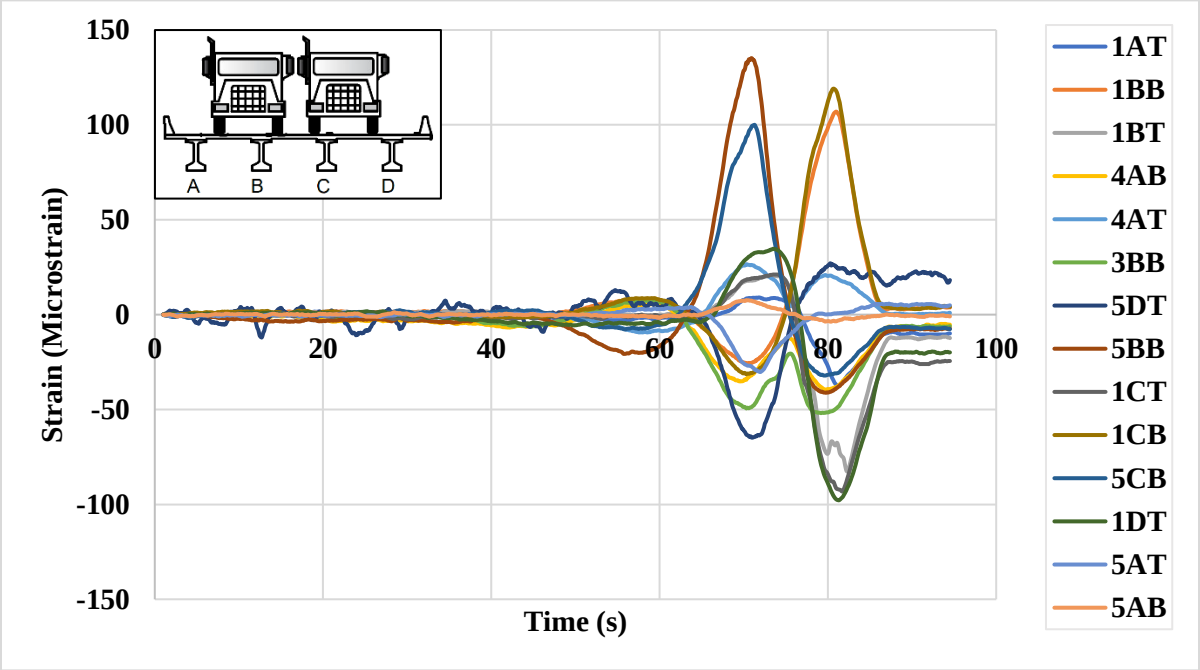

Figure 7- 8 Strain responses during stop the location test

Though girder D is also an exterior girder, the strain response of girder D is higher than the strain response of girder A in regard to the designated path run for girder D (Path 2). In the case of the stop location test, the response of girder D shown higher response as expected compared to other girders (girders B and C).

7.1.2 Unintended Composite Action

Some degree of composite action may exist even with the absence of shear connectors between concrete deck over steel girders. (Breña et al. 2012; Stallings and Yoo 1993). Some unintentional deck-girder composite action may exist due to the self-weight of the curb, railing, and deck, creating adhesion or friction. Yost et al. (2005) and Kwasniewski et al. (2000) concluded that the unintended composite action should not be considered during strength calculation in the ultimate state. Due to the reliability issue, if composite action is observed in the diagnostic load test, it

should not be considered in strength calculation until composite action is proved by proof load test (NCHRP 1998).

To check any presence of composite action, the neutral axis of the girder section was calculated from the measured top and bottom strain data, assuming a linear strain profile along the cross-section of the girder. The calculations for the experimental neutral axis were performed using equation 7-1 as shown by the process in Figure 7-9.

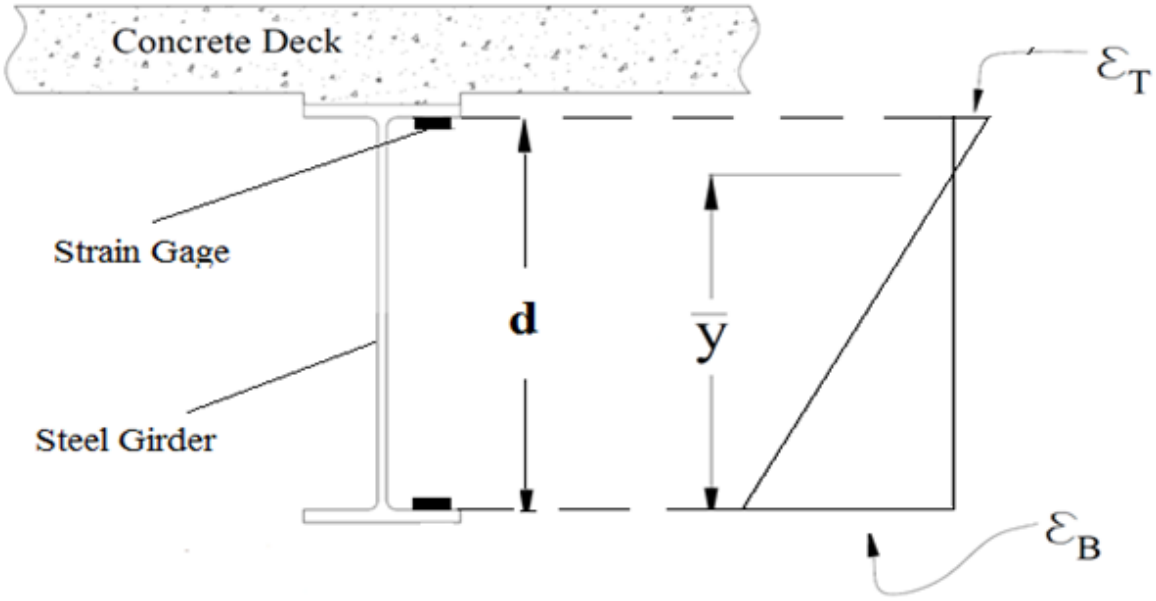

Figure 7- 9 Neutral axis calculation

The strain gage location from the bottom of the girder can be calculated using equation 7-1:

$$\overline{y} = \frac{\varepsilon_B d}{\varepsilon_B + \varepsilon_T} \qquad (7\text{-}1)$$

where:

$\overline{y}$ = Neutral axis location from the bottom (in)

d = distance between the top and bottom gauges (in)

ε_B = Strain in bottom gauge ($\mu\varepsilon$) (Absolute value)

ε_T = Strain in top gauge ($\mu\varepsilon$) (Absolute value)

The analysis of the data from strain gages indicates that the neutral axis shifts below the theoretical neutral axis for the damaged section of the affected girder (girder A, section 5) (Figure 7-10). Figure 7-11 presents the neutral axis location at section 4 for girder A. Section 4 is in a negative moment zone. The neutral axis at section 4 for girder A fluctuating over the theoretical neutral axis. The orange line shows the theoretical location of the neutral axis for the figures.

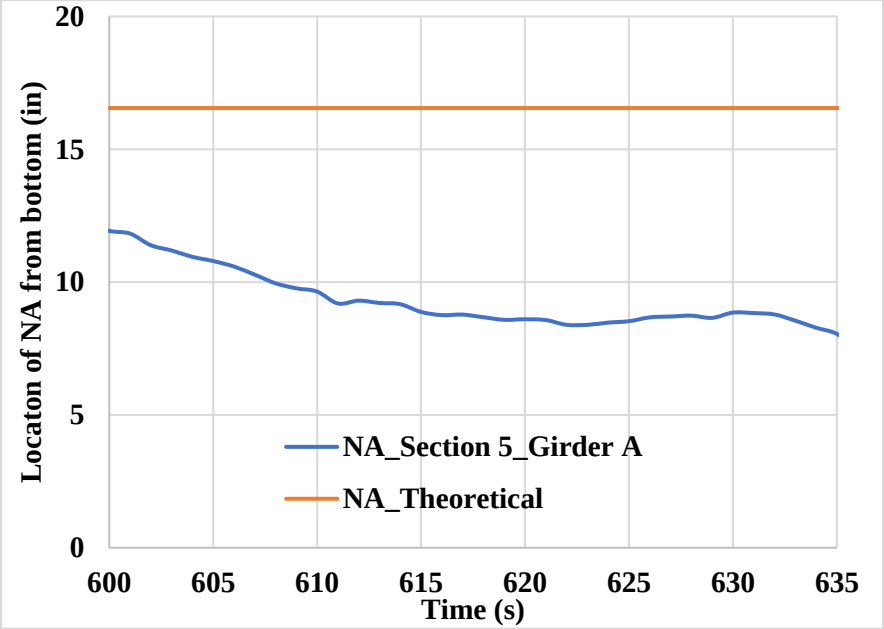

Figure 7- 10 NA location of girder A at section 5

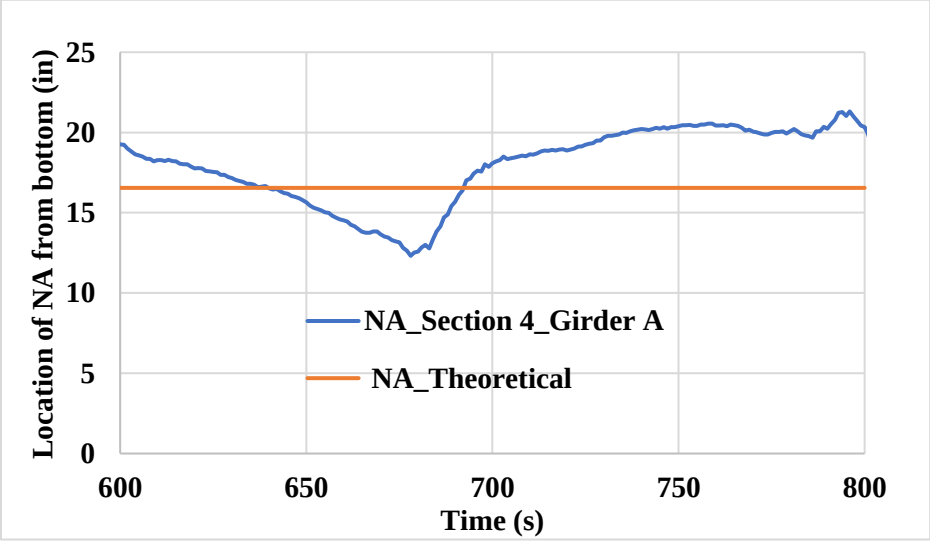

Figure 7- 11 NA location of girder A at section 4

Figures 7-12 and 7-13 show the location of the neutral axis for an unaffected girder (girder B) at section 1 and section 3, respectively. Figure 7-14 shows the neutral axis location of girder C at section 1. Section 3 also lies in the negative moment zone. Table 7-1 shows a summary of the neutral axis obtained from the load test.

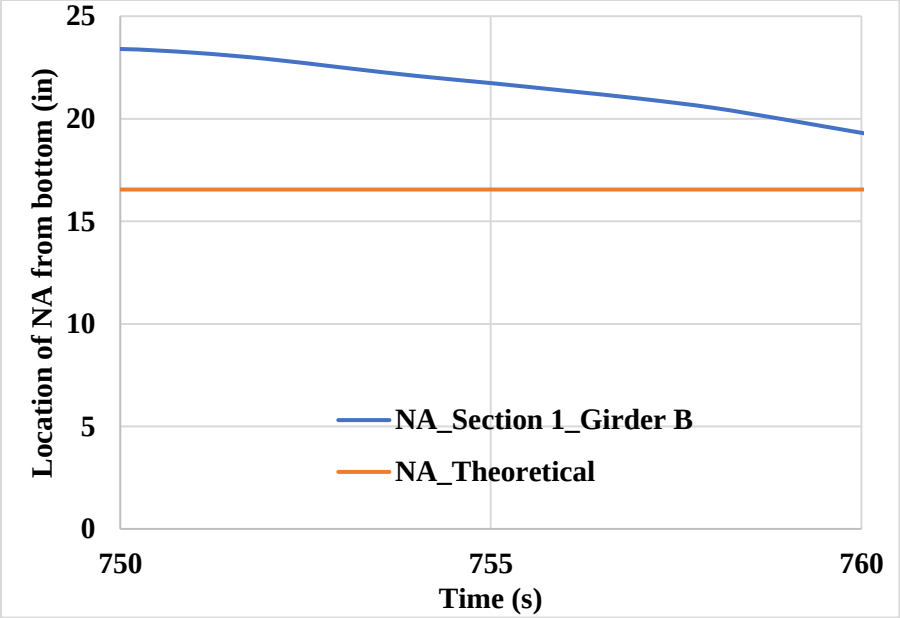

Figure 7- 12 NA location of girder B at section 1

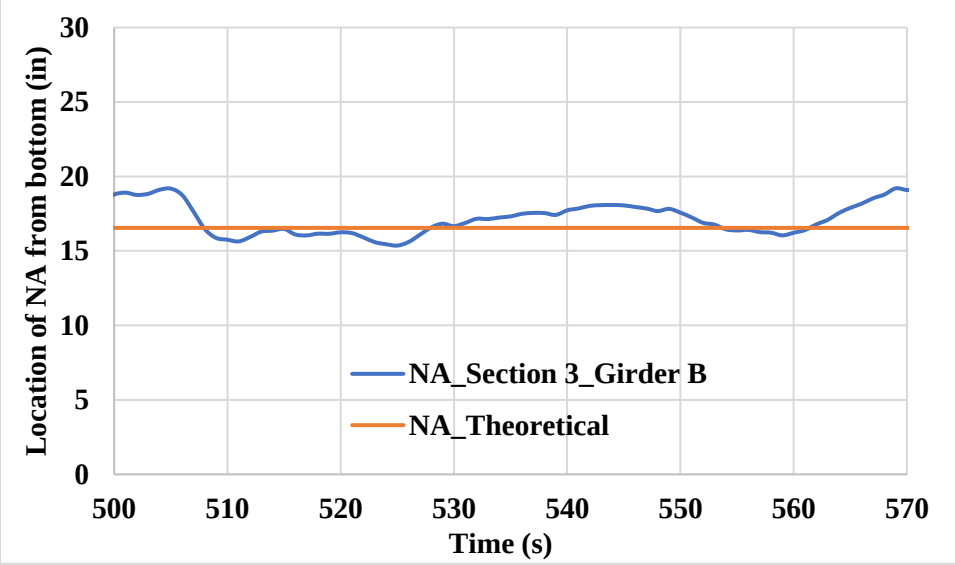

Figure 7- 13 NA location of girder B at section 3

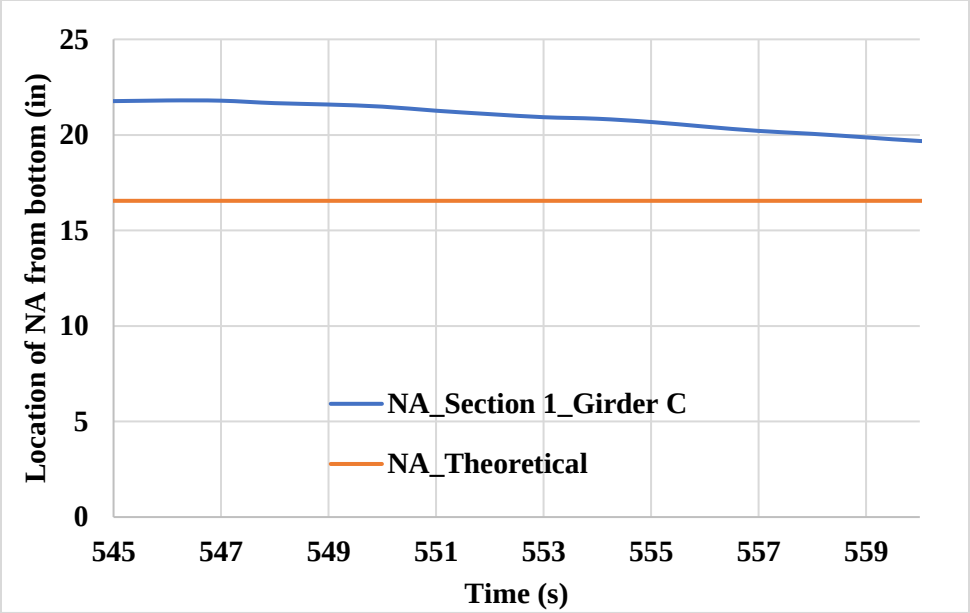

Figure 7- 14 NA location of girder C at section 1

Table 7- 1 Summary of the neutral axis

Girder Designation	Section	Distance (ft)	NA depth from the bottom flange (in.)
A	4	15 ft. right from bent 3 (span 3)	17.94
A	5	30 ft. right from bent 3 (span 3)	8.65
B	1	30 ft. left from bent 3 (span 2)	21.23
B	3	15 ft. left from bent 3 (span 2)	18.17
C	1	30 ft. left from bent 3 (span 2)	17.70

The location of the theoretical non-composite and composite neutral axis for the girder was calculated as 16.55 in and 29.26 in from the bottom flange, respectively. The neutral axis location for the unaffected girders was roughly 17-22 in. The difference in NA location was probably caused by unintentional deck-girder composite action due to the self-weight of the curb, railing, and deck creating adhesion or friction. From the analysis of the neutral axis, an average of 15% unintentional composite action was observed. Neutral axis location of 16.55 in (non-composite) and 29.26 in (composite) from the bottom flange denotes 0% and 100% composite action, respectively. The neutral axis for the deformed section of the affected girder was calculated at

around 9 in. from the bottom flange, potentially resulting in a reduced capacity for the section where the girder A was impact damaged.

7.1.3 Rotation Data

The rotational tiltmeters provided the end rotations of the girders. Figure 7-15 shows raw data of rotation versus. time diagram for girder A due to loading on Path P3 Run 1. The designation of tiltmeters was represented in a way that the first letter and second digit express a bent number (bent 2, bent 3, bent 4), and the third letter shows the girder name (girder A, B, C, and D). Data showed a lot of noise and vibration. This noise might be caused due to the vibration of the bridge during live load movement. The rotation data was then refined using the moving average between 10 points similar to the strain results. Figures 7-16a, 7-16b,7-16c, and 7-16d show the refined rotation data for girders A, B, C, and D, respectively, for Path P3 Run 1.

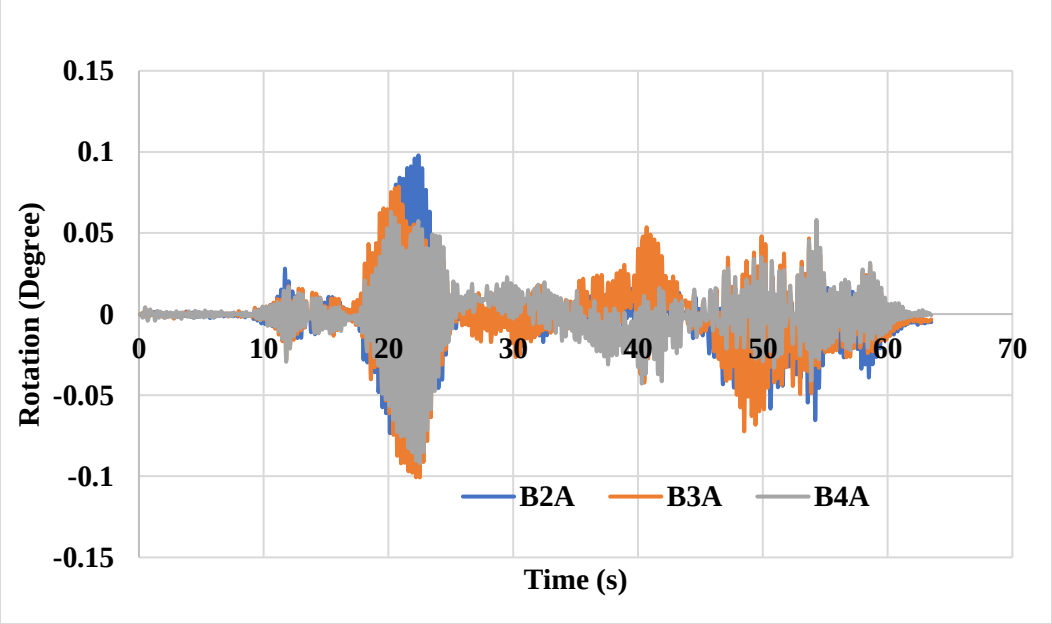

Figure 7- 15 Raw rotation data for Path P3 Run 1 (Girder A)

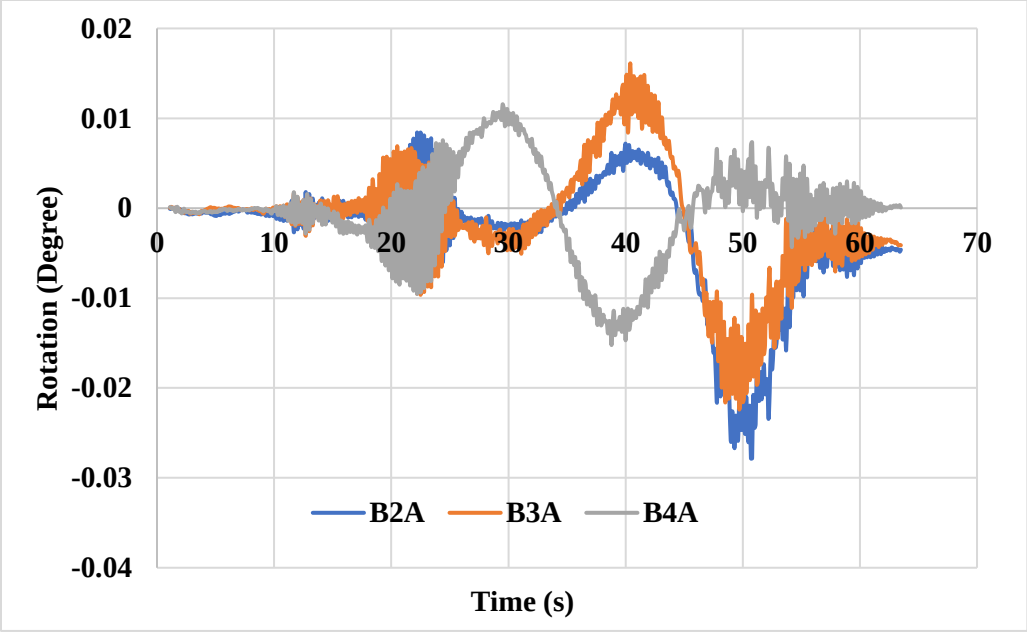
0.02
0.01
0
-0.01
-0.02
-0.03
-0.04
0
10
20
30
40
50
60
70
Rotation (Degree)
Time (s)
B2A
B3A
B4A

(a)

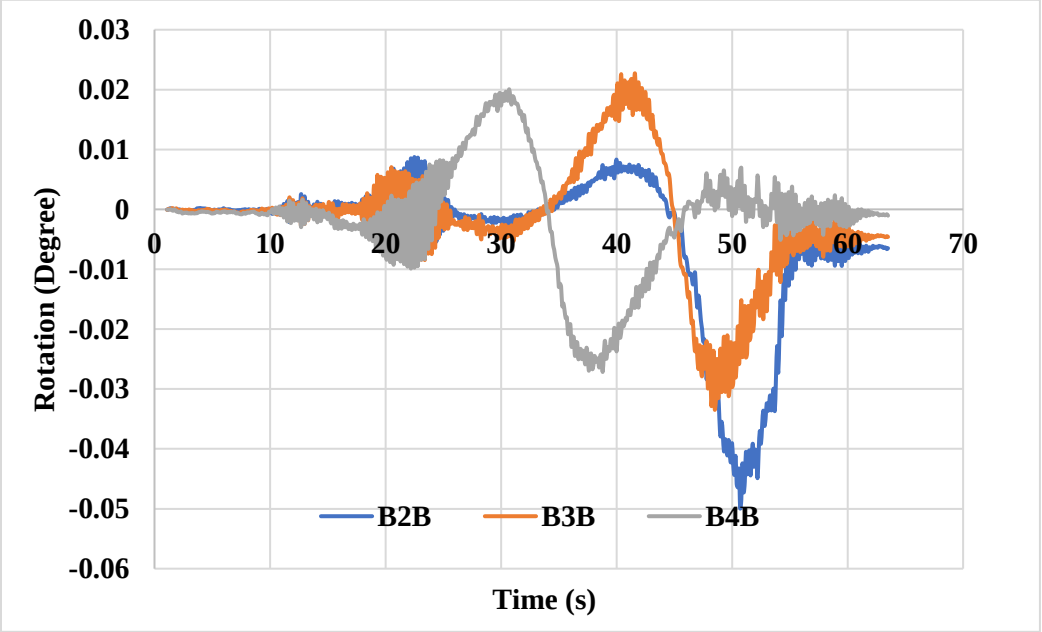
0.03
0.02
0.01
0
-0.01
-0.02
-0.03
-0.04
-0.05
-0.06
0
10
20
30
40
50
60
70
Rotation (Degree)
Time (s)
B2B
B3B
B4B

(b)

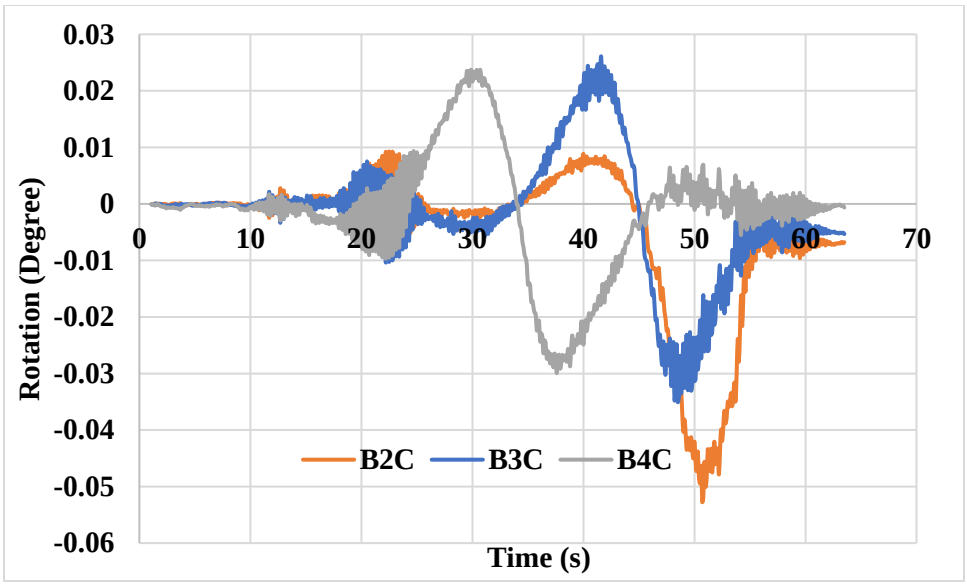

(c)

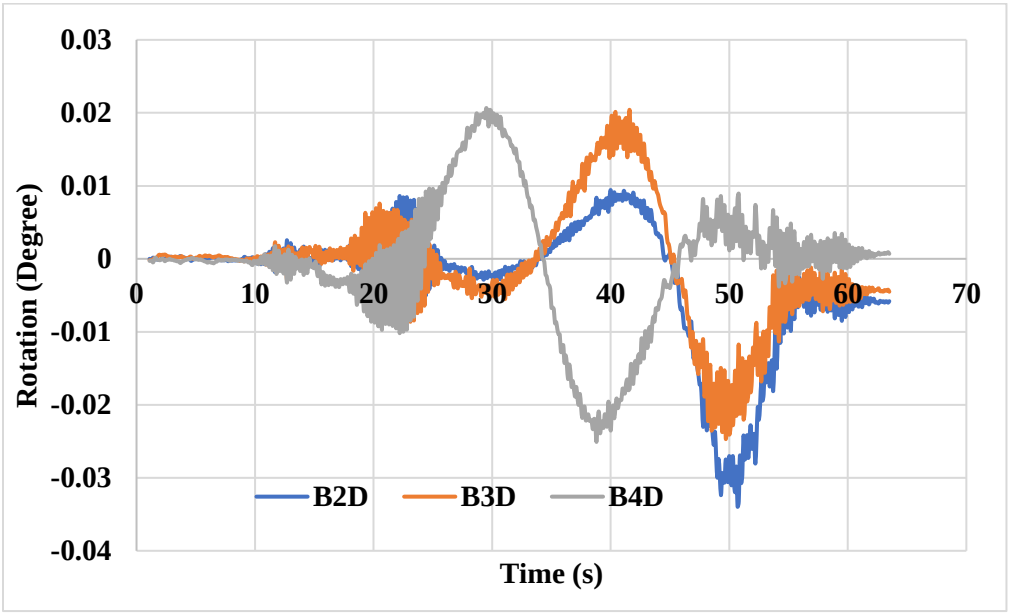

(d)

Figure 7- 16 Rotation vs. time for Path P3 Run 1: (a) girder A; (a) girder B; (a) girder C; (a) girder D

Finite element analysis gained more credibility once rotation and strain data were utilized to calibrate the model (FEM).

7.2 NDE Results

7.2.1 GPR Results

The GPR scans were post-processed and analyzed with the GPR-SLICE (2018) software. No delamination could be observed from the GPR scans. One possible reason is that the cracks, voids, or delamination should be at least 0.25 in. wide to be visible in the B-scans obtained from the GPR. However, the reinforcement profile was clearly visible. A 2-D contour plot prepared from the top reinforcement cover depths found through the GPR scans is presented in Figure 7-17.

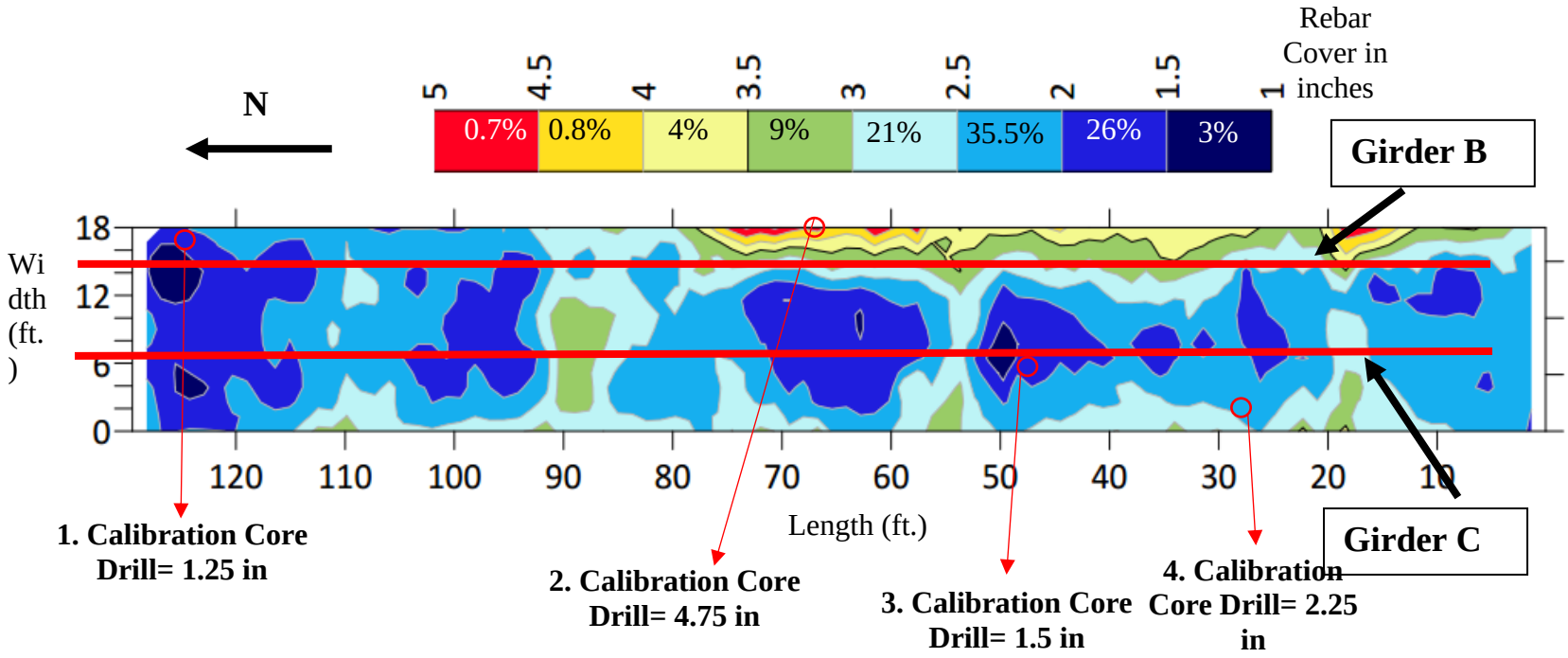

(Note: The color legends indicate the area of different cover depth ranges. The percentage of the area at different cover depth ranges is shown.)

Figure 7- 17 The 2-D contour plan of span 2 and 3 showing the top reinforcement cover depths

The results presented herein are in the form of continuous contour maps where linear interpolation was used between the data points. The cover value achieved from the GPR data has a tolerance of ± 0.25 in.

According to the bridge drawing provided by TxDOT, the minimum clear cover for top layer rebars in the deck was 1.5 in. The contour plot indicates a lower cover depth ranging from 1-2 in. at 29% of the total deck area. Conversely, about 14% of the deck area has top rebar concrete covers over 3 in or greater.

Four small cores were drilled to calibrate the GPR scanned contour plots, and the core depths matched the contour plot depths. The locations of the cores are highlighted using red circles (Figure 7-17) in the contour plan. The drilled core depths are shown in Figure 7-18, verifying the accuracy of the GPR readings.

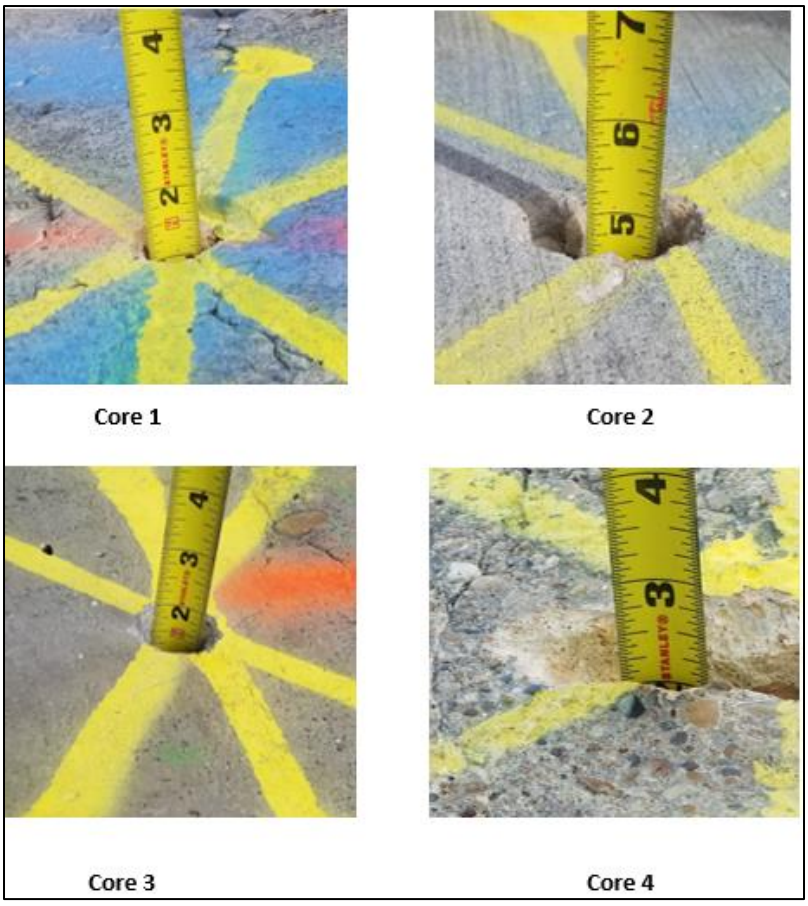

Figure 7- 18 Calibration core drill depths

Based on their findings, Omar et al. (2017) concluded that GPR can locate the rebar location and spacing. According to as-built drawings, the rebar spacing was approximately 7.5 in. center-to-center (c/c), but from GPR scanning, different spacing was observed on the girder line of girder B and girder C. Table 7-2 shows the spacing of the rebars along the girder line. The girders lines are then shown in Figure 7-17.

Table 7- 2 Rebars spacing along the girder line

Spacing along girder line C	**Spacing along girder line B**
6.384	7.056
5.736	6.744
6.024	6.36
6.696	6
5.736	6.096
6.744	7.704
7.704	6.072
5.736	6.768
5.688	6.672
8.712	7.008
4.728	7.104
6.672	6.336
6.432	5.088
6.048	5.352
6.72	7.8
6.72	6.72
6.384	6
7.056	6.384
6.384	7.056
7.776	6.72
5.328	7.08
6.072	6.36
6.696	6

5.664	5.76
7.44	6
6.36	6.432
7.08	6.768
7.08	6.672
5.016	6.768
6.384	6.336
8.064	5.424
7.416	8.016
5.016	7.344
7.344	4.08
7.44	9.36
8.4	7.776
5.712	3.984
7.368	9.792
5.736	5.328
7.104	6.768
5.328	5.712
6.672	6.72
6.768	6
6.672	7.44
5.76	6.36
7.08	5.736
7.68	8.064
7.752	7.392
5.688	5.328
4.728	6.12
8.112	7.032
6.336	5.688
5.424	6.072

4.992	7.368
6.048	5.736
6.048	5.424
8.112	7.008
6.336	7.032
7.104	7.08
7.32	7.44
6.12	6.336
6	4.704
7.08	7.392
6.36	7.368
6	5.064
5.424	6.096
8.016	7.008
6.096	8.112
6.384	3.648
5.376	7.752
8.064	7.368
5.04	6.432
7.08	6.336
5.016	6.024
7.704	6.408
6.072	7.032
8.088	7.416
5.352	5.664
7.368	6.432
7.08	6.048
4.32	5.376
4.416	7.704
9.024	6.408

7.44	5.352
6	8.088
6.72	5.352
8.16	8.088
5.64	5.352
6.36	8.088
5.76	5.712
7.68	6.72
4.08	5.04
7.68	6.384
7.08	7.776
7.44	6.336
7.032	6.024
7.368	8.76
4.08	4.32
8.76	7.776
2.976	5.064
5.664	6.36
8.112	5.76
8.448	7.68
4.656	6.36
6.744	5.736
5.64	7.104
6.72	6.672
6.72	6.048
6.48	6.72
6	6
7.44	6.768
6	5.712
7.08	6.72

6	7.08
7.08	6.36
6	6.72
6.48	7.392
6	6.408
7.08	5.688
7.08	5.712
5.04	6.72
8.04	7.08
6.36	6.36
6.36	8.04
7.08	6.744
5.4	5.736
7.08	5.352
6.36	7.368
7.32	6.744
6.72	6.696
4.752	6.072
7.728	7.008
4.704	6.096
7.416	5.664
6.696	7.104
7.344	6.696
5.088	5.736
7.032	7.344
7.08	6.432
6.36	6.048
5.4	7.392
7.08	6.048
6.36	6.72

7.08	6.72
7.032	6.384
6.048	6.696
6.384	6.072
6.336	5.688
6.096	5.4
7.704	6.36
6.408	7.752
5.712	6.768
6.384	7.008
6.696	5.712
6.072	5.712
7.008	6.768
6.096	6.336
6.744	7.104
4.68	6
7.08	6.36
7.032	6.408
7.728	7.752
5.04	2.664
7.68	9.456
6.72	6.672
3.36	10.416
7.776	8.352
6.024	6.096
8.088	6.384
5.712	6.36
7.08	5.76
6.36	7.68
6	6.36

6.72	6.72
5.04	5.04
7.44	6.48
6.72	7.008
7.08	8.352
4.68	4.752
6.384	8.088
7.776	6.36
6.36	8.4
8.376	3.696
5.664	10.416
6.432	4.368
6.408	6.384
6.72	6.696
6	6.12
6.12	5.64
7.32	8.088
6.072	5.352
7.728	6.744
6.36	7.056
5.064	4.704
7.776	8.376
5.664	5.064
7.416	7.056
6.024	6.384
5.736	6.336
8.376	8.448
7.344	4.752
4.416	7.68
8.064	6

5.04	5.424
6.36	6.336
6.744	8.112
6.336	5.328
7.44	7.44
4.704	5.76
9.744	7.68
5.712	6
7.392	5.4
4.728	6.72
6.696	7.44
7.104	6.72
6.336	6.36
6.384	7.392
5.712	5.688
7.368	6.408
5.064	4.752
7.056	8.4
7.68	6.72
7.8	6
5.016	7.68
5.424	5.76
8.04	7.44
5.4	5.64
6.72	6.36
4.32	6.72
9.12	7.08
6.36	5.4
7.08	8.04
4.68	4.44

7.32	7.32
6.12	6.12
5.64	6.36
5.4	7.32

7.2.2 IE Results

The IE results on discrete data grids were then plotted on 2-D contour maps, as shown in Figure 7-19. A table summary of the delamination is shown below in Table 7-3. On the contour maps, red indicates a very high possibility of the presence of concrete delamination. The blue areas indicate sound concrete without any possible debonding or delamination. The delamination depths are expected to be within 4 in from the top surface.

Table 7- 3 Summary of Delamination

Levels of Delamination		
Type	**Lane 1**	**Lane 2**
No Delamination	19.4 %	12.24%
Fair Delamination	36.6%	49.88%
Severe Delamination	44.0%	37.88%

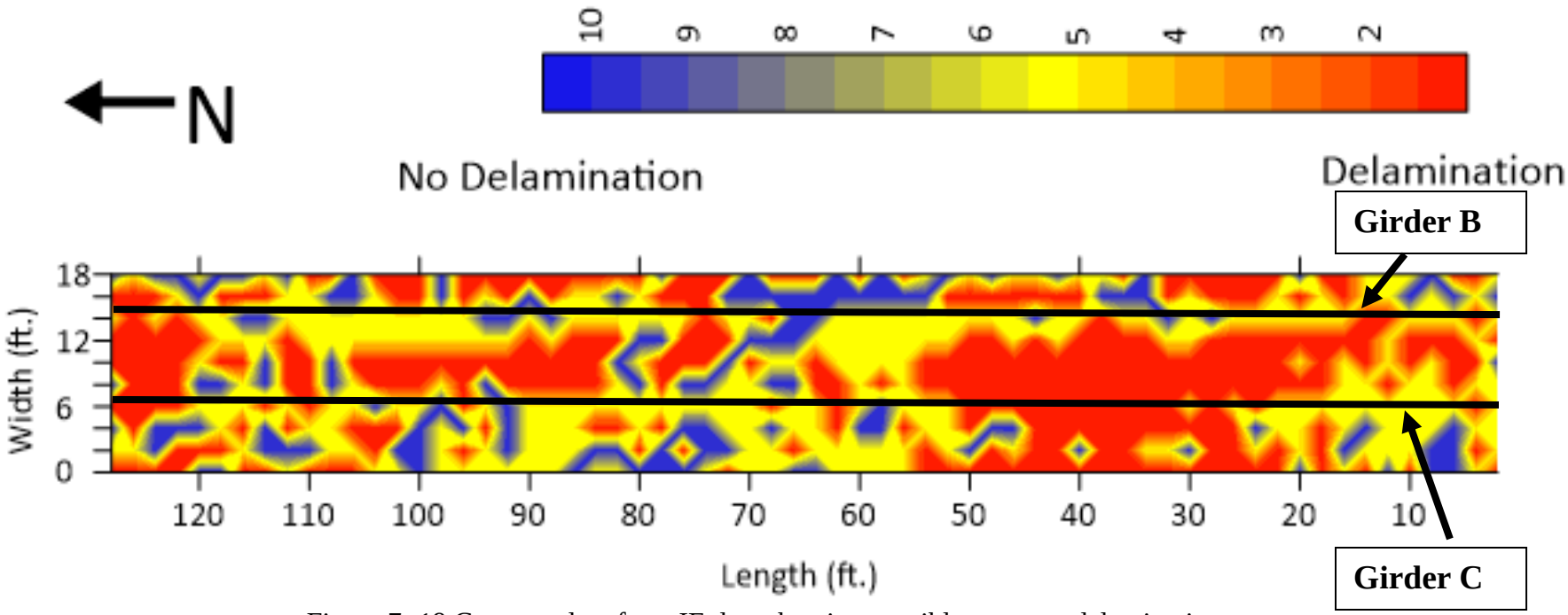

Figure 7- 19 Contour plots from IE data showing possible concrete delamination

7.3 Live Load Distribution Factor

Live load distribution factor (LLDF) determines the percentage of live load carried by individual girder under a certain load condition. To calculate live load distribution factor the ratio of maximum strain (ε) of a girder to sum of the strains of all girders of a particular section at a particular instance was considered as shown in Eq. 7-2.

$$\mathrm{g} = \frac{\varepsilon_i}{\sum_1^n \varepsilon_i} \tag{7-2}$$

The distribution factor was calculated for the Paths and the largest values are presented in Table 1 along with theoretical distribution factor. Theoretical distributed was calculated for two or more lane loaded traffic according to AASHTO Standard Specification for Highway Bridges. Eq. 7-3 and Eq. 7-4 shows the LLDF formula for interior and exterior girders respectively.

$$\text{LLDF interior beam} = \frac{S}{5.5} \tag{7-3}$$

$$\text{LLDF interior beam} = \frac{S}{8} + \frac{Ln}{8} \tag{7-4}$$

Where: S= girder spacing, Ln= No. of lanes on the bridge.

As compared with exterior girder D and girder B and C, girder A's distribution factor was lower. It is possible that the load path has been altered since the girder A was damaged and repaired several times. The theoretical distribution factor was conservative compared to the experimental values. The final analysis considered the experimental values.

Table 7- 4 Live load distribution factor

Girder Designation	Experimental LLDF	Theoretical LLDF
A	0.12	1.25
B	0.61	1.45
C	0.37	1.45
D	0.47	1.25

7.4 Load Rating

Two cases were considered herein for the load rating of the bridge:

1. Deck capacity alone in the transverse bridge direction.
2. Girder capacity alone in the longitudinal girder span direction. In this case, an assumption was made that the deck is 100% non-composite with the girder.

Case 1: Deck Capacity

The deck capacity of the bridge was calculated using the GPR and IE data, following the procedure outlined below:

1. The material properties used to calculate deck capacity were mentioned in the material properties section of the report. The rebar size and spacing were found from the as-built drawing and listed in Table 7-5. Due to the inability of GRP data to verify rebar diameter, the diameter of rebar was determined using as-built drawings. Moreover, due to the uncertain level of corrosion, capacity calculations were made using a complete rebar cross section.

Table 7- 5 Rebar properties

Rebar Location	**Rebar size and spacing**
Bottom mat	#5@ 6.5'' o. c.
Top mat	#5@ 6.5'' o. c.

- The moment capacities of the deck were calculated for a 12 in. wide strip along the length of the girder. The length of the strip was measured at 8 ft., which is similar to the spacing of the girders.
- GPR data was used to find the cover for the negative deck steel near the girder lines. The negative region was found to be 2.21 ft. from both sides of the centerline of the girder. This length was determined by calculating the point of contra flexure of a continuous beam. The detailed calculation, which was also verified using SAP2000 (2016), is provided in Appendix A. In approximately 77% of the negative region area, the top cover was found to be 2 in from the GPR data analysis, which was used in the negative moment calculation. Figure 7-20 shows the girder line edges (yellow lines) and the analyzed negative moment

region (hatched area) on a portion of the GPR data from where the average top cover of 2 in. was found.

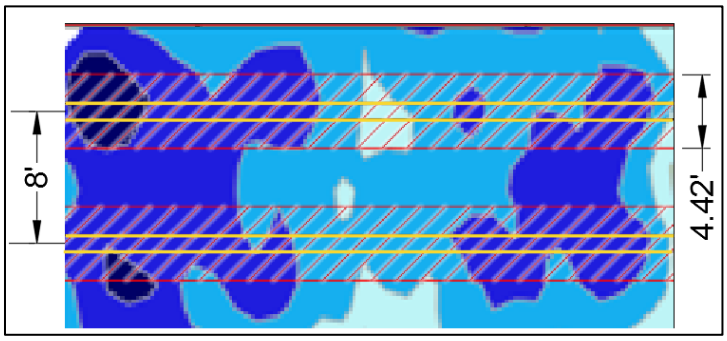

Figure 7- 20 Negative moment region (hatched area) and girder line edges (yellow) on a portion of GPR contour

- Positive moment capacity i.e., positive moment region rebar cover couldn't be managed by GPR data due to heavy traffic under the bridge on I-30. GPR detected only the top rebars which contribute to the negative moment capacity only. The positive cover was measured at 1.5 in, according to the drawing.
- The nominal moment capacity of the deck was calculated using Ø = 0.9 since the section was tension controlled.
- From the Impact Echo (IE) data, the percentage of delamination for both the negative and positive moment regions were measured at 2.21 ft. from both sides of the centerline of the girder and 3.58 ft, respectively. The distances were calculated using the same method used to find the negative moment region from the GPR contour (Appendix-A). Figure 7-21 shows the positive and negative moment region (hatched area) and the girder line edges (black lines) from where the percentage delamination was extracted.

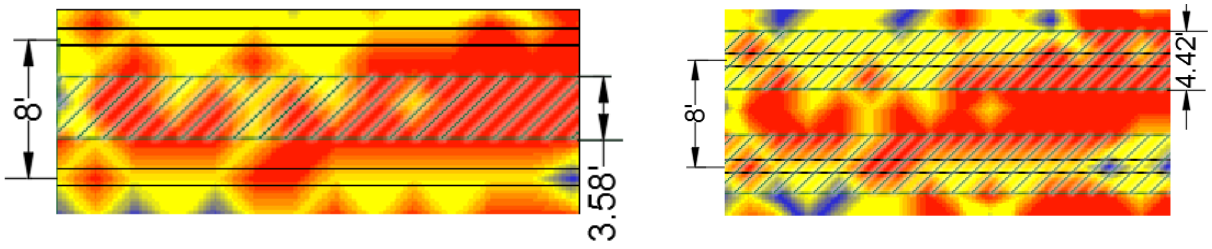

(a) (b)

Figure 7- 21 IE data: (a) Positive moment region (b) Negative moment region

- The percentage of delamination for the positive region and negative region were found to be 50% and 31%, respectively. It should be noted that the 2-dimensional IE contour cannot verify the depth of delamination. Since the depth of delamination is unknown, it is difficult to determine whether the delamination is in the positive region or negative region. To be conservative, an average between the delamination of both regions (40%) was applied to reduce the positive and negative moment capacity. Table 7-6 shows the moment capacities of the deck calculated from GPR and IE data.
- Contribution of compression rebar in the concrete deck was not considered.

Table 7- 6 Deck moment capacity of the bridge

Moment Type	**Moment Capacity (k-ft./ft.) (From GPR data)** **Mn= Asfy (d-$\frac{a}{2}$)**	**Design Moment Capacity (k-ft./ft.) (From GPR data)** **ØMn**	**Average Percentage delamination for positive/negative region**	**Modified Moment Capacity (k- ft./ft.) (From IE)**	**Moment Capacity (k-ft./ft.) Only suing IE data**
Positive	8.82	7.94	40%	4.8	5.3
Negative	7.30	6.57	40%	3.9	4.4

From the AASHTO Manual for Bridge Evaluation (2018), the moment rating factor of concrete components can be calculated using Eq. 7-5.

Moment Rating Factor,

$$RF= \frac{Moment\ Capacity - A1\ X\ Dead\ load\ Moment}{A2\ X\ (Live\ load\ Moment + Impact)} \qquad (7-5)$$

Moment Capacities used in moment rating are listed in Table 7-4 for both positive and negative moment. Negative moment governed for rating. A1 and A2 are rating factors, and A1=1.3 and A2 vary depending on the rating level desired. (A2=2.17 for inventory level and 1.3 for operating level). The live load moment was determined using HS-20 loading, including an impact factor of 1.3. The detailed hand calculation is provided in Appendix-B (provided upon request). Table 7-7

and Table 7-8 show a summary of deck load ratings based on the Load Factor Rating Method (LFR) for both positive and negative moment respectively.

Table 7- 7 Summary of deck rating for positive moment

Rating Level	**Rating Factor (RF) (40% delamination+ Ø Mn)**	**Rating Factor (RF) (40% delamination)**	**Bridge member rating (lb.) (40% delamination+ Ø Mn)**	**Bridge member rating (lb.) (40% delamination)**
Inventory level	0.36	0.41	25,920	29,520
Operating level	0.61	0.68	43,920	48,960

Table 7- 8 Summary of deck rating for negative moment

Rating Level	**Rating Factor (RF) (40% delamination+ Ø Mn)**	**Rating Factor (RF) (40% delamination)**	**Bridge member rating (lb.) (40% delamination+ Ø Mn)**	**Bridge member rating (lb.) (40% delamination)**
Inventory level	0.3	0.33	21,600	23,760
Operating level	0.48	0.55	34,560	39,600

Member rating = $W\ X\ RF$ $(7-6)$

Where W= Weight of the nominal truck used in determining the live load effects.

Case 2: Girder Capacity

The load rating of the girder was conducted based on the experimental data load test using the LFR method (AASHTO 2018). Girder load rating was performed assuming non-composite action. The rating equation and factors were considered the same as equation 7-2. A detailed calculation is presented in Appendix-C. Table 7-9 and Table 7-10 show the summary of girder ratings based on the Load Factor Rating Method using both conventional method and modified method

(incorporating load test data). The basic difference between these two methods was the difference in live load distribution factor.

Table 7- 9 Summary of girder rating by conventional procedure

Girder Designation	Rating Level	Rating Factor (RF) assuming non-composite	Bridge Member Rating (lb.) assuming non-composite
A	Inventory level	0.55	39,600
	Operating level	0.92	66,240
B	Inventory level	0.48	34,560
	Operating level	0.80	57,600
C	Inventory level	0.48	34,560
	Operating level	0.80	57,600
D	Inventory level	0.55	39,600
	Operating level	0.92	66,240

Table 7- 10 Summary of girder rating by modified method

Girder Designation	Rating Level	Rating Factor (RF) assuming non-composite	Bridge Member Rating (lb.) assuming non-composite
A	Inventory level	2.88	207,360
	Operating level	4.8	345,600
B	Inventory level	0.57	41,040
	Operating level	0.95	68,400
C	Inventory level	0.87	62,640
	Operating level	1.45	104,400
D	Inventory level	0.81	58,320
	Operating level	1.35	97,200

7.5 Model Calibration

Manual model updating is an effective method of obtaining an accurate FE model that can capture all aspects of structural behavior and represent the structural performance of the bridge. A successfully incorporated calibration procedure can reduces the modeling errors of an initial FE model.

With age, the concrete compressive strength continues to increase. This increment is related to other material characteristics, such as tensile strength, modulus of elasticity, and time-dependent effects. AASHTO LRFD specifications do not address these incremental issues. The Comite Euro-Intermationale du Beton/Federation International de la Precontrainte (CEB-FIP) Model Code (1990) (FHWA 2016) provides a relationship for the change in concrete compressive strength over time, as shown in Eq. 7-7 and 7-8:

$$f_{cm}(t) = \beta_{cc}(t) \cdot f_{cm} \quad (7\text{-}7)$$

$$\beta_{cc}(t) = \exp\{s\,[1-(\frac{28}{\frac{t}{t1}})^{0.5}]\} \quad (7\text{-}8)$$

where:

f_{cm} = 28-day compressive strength

$f_{cm}(t)$ = concrete compressive strength at time t

β_{cc} = time-dependent coefficient, dependent on age of concrete

t = age of concrete at which $f_{cm}(t)$ is computed (days)

t_1 = 1 day

s = cement rate of hardening coefficient (0.20 for rapid hardening high strength concrete, 0.25 for normal and rapid hardening concrete, 0.38 for slow-hardening concrete)

Figure 7-22 shows a plot of the ratio of concrete compressive strength to 28-day vs age of concrete.

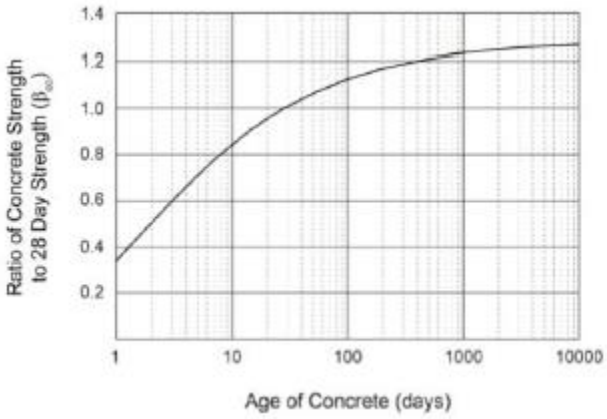

Figure 7- 22 Increase of concrete strength over time

The uncalibrated model of a three-span continuous composite bridge consisting of concrete deck over steel girders was modified according to Sanayei et al. (2012). The first modification was implemented to increase the concrete compressive strength to reflect the cylinder test results. The second modification was meant to reduce concrete stiffness in the negative bending area to reflect concrete cracking.

Even though adjusting the moment of inertia (to reduce concrete stiffness) of a partially composite /non-composite concrete deck over steel girders in the Finite Element Method (FEM) is complex, the modulus of elasticity of concrete can be more easily modified, leading to the same results Sanayei et al. (2015).

From the IE data, delamination for both the negative and positive moment regions in the deck was observed. It should be noted that the 2-D contours cannot verify the depth of delamination. In the first phase of modeling, for calibration purposes, two modifications were performed in the uncalibrated model. The first modification included a reduction of the shear stiffness coefficient between the deck and the girder interface (contact property) while the second modification included a reduction of concrete stiffness in traffic lanes. The theoretical modulus of elasticity (E_c) of concrete was reduced. Figure 7-23 (green area) shows the modified region.

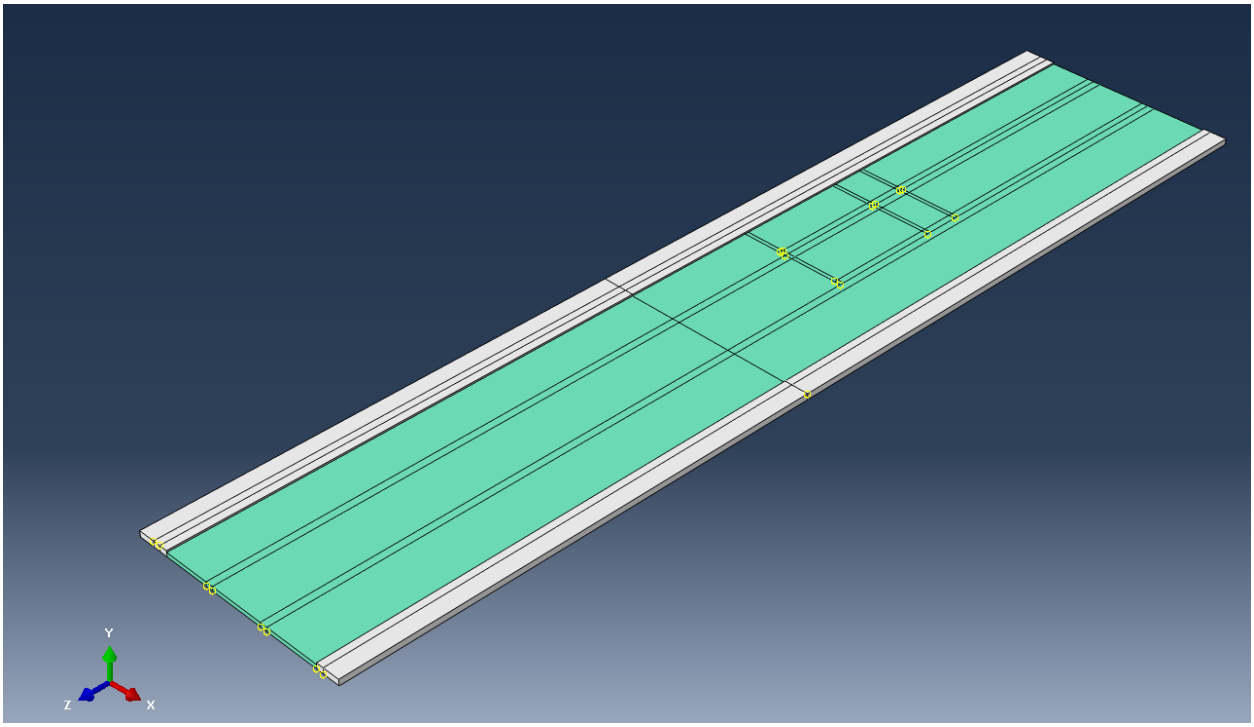

Figure 7- 23 Traffic lanes with reduced stiffness

In the second phase of modeling, the compressive strength of the deck concrete was assumed to be 3 ksi. Based on the equation 7-4, the current compressive strength was assumed as 3.8 ksi for undamaged concrete. Previously, the reduction of concrete stiffness in damaged concrete (traffic lanes) was done. Only, the modulus of elasticity (E_c) of concrete was reduced for damaged concrete to address the reduction of concrete stiffness. In this approach, the damaged concrete was updated using the concrete plasticity model (CDP) with the Python code instead of only the modified E_c. For calibration purposes, a wide range of compressive strengths of concrete (f_c) was considered for damaged concrete (traffic lanes). The compressive strength of concrete was reduced to 1.85 ksi after assuming 40% delamination of concrete.

Albraheemi (2018) found that cohesive properties can replicate the percentage of composite action that resembles field data. Consequently, cohesive interaction properties were incorporated into the model. Though cohesive interaction properties can simulate the percentage of composite action between the concrete deck and steel girder, the shear stiffness coefficient had to be adjusted. A wide range of shear stiffness coefficient (K_{tt} & K_{ss}) was accordingly applied to the model while the normal stiffness coefficient (K_{nn}) was set as a constant (10^9 psi). In the model, shear stiffness

coefficients K_{ss} and K_{tt} were assumed to be equal. The value of K_{tt} and K_{ss} wereconsidered as 500 psi.

The FEM was calibrated using load test data. Strains at the bottom of the girders of Span 3, 25 ft. from Bent 3 of the model, were matched with experimental strain values obtained from the load test. Furthermore, rotations near the bent cap of the girders of the model were compared with rotations during the field test. The final calibrated model obtained after the calibration process was used to compare the experimental results with the modeling results. Figure 7-24 shows the comparison of the strain data between the experiment and the FEM of bottom strain gages. Figure 7-25 then presents the comparison of the rotations between the experiment and the FEM.

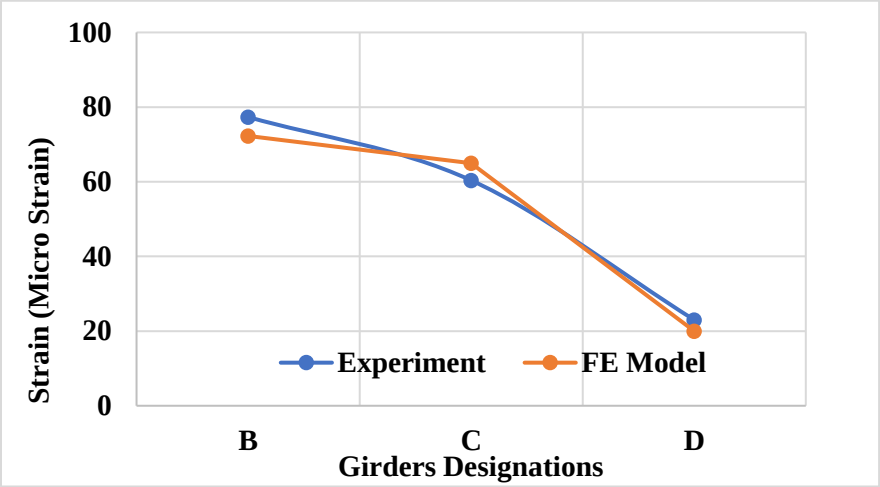

Figure 7- 24 Strain comparison between experimental results and the FE model

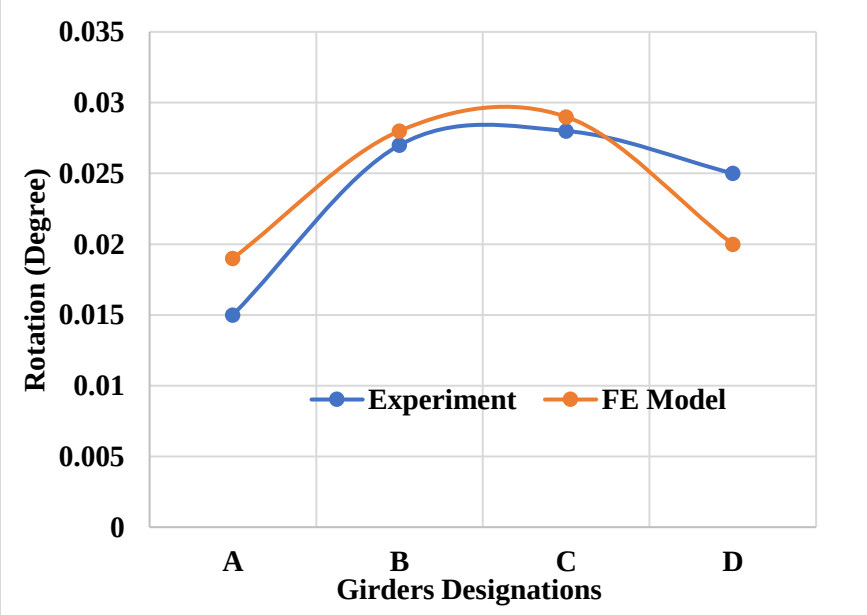

Figure 7- 25 Rotation comparison between experimental result and FE model at bent 4

The experimental and FE model showed a good correlation in the case of both strain data and rotation data. The small deviations could be due to the effects of support fixity, material non-uniformity, or non-uniform delamination.

Chapter 8

BRIDGE RETROFITTING

The objectives of the retrofitting method are to improve the stiffness as well as the load-carrying capacity of the bridge. The approaches described in this chapter have already been used in industry or have been tested by other researchers in the past (in Chapter 2).

The modeling scheme involved: (1) Complete superstructure model of the bridge with all the elements i.e., concrete deck, steel girders, rebars to check strain and deflection responses before and after retrofitting; and (2) Modeling of concrete deck and the steel girders separately to find out their post-retrofitting moment capacity.

8.1 Removal of Deck Top Concrete and Recasting of Concrete (Complete superstructure)

The IE data showed severe delamination in bridge deck. So, to increase the strength and stiffness in the negative moment zone recasting of fresh concrete is a suitable option. Normally, in this case deck top surface is removed and new concrete is placed. In the numerical modeling to replicate the removal of concrete and recasting of fresh concrete, 2.5 in. separate partition was created from the top of the concrete deck. Figure 8-1 shows the partition of new concrete and old concrete. The strength of the new concrete was considered as 4 ksi and 6 ksi. On the top partition of the deck, old concrete properties were replaced with the 4 ksi and 6 ksi concrete properties sequentially. In both of the cases concrete CDP model was used to find tensile and compressive and plastic behavior of concrete. All other properties remained the same as the calibrated model. As the partition was created between the same element (in the deck) so, there was no need for constraint. In the newly placed concrete showed greater stiffness, as there is no delamination. The retrofitted model successfully completed, and the results were compared with calibrated model. Table 8-1 shows a comparison of strain and deflection of the concrete deck top (negative moment zone) for the calibrated and retrofitted model.

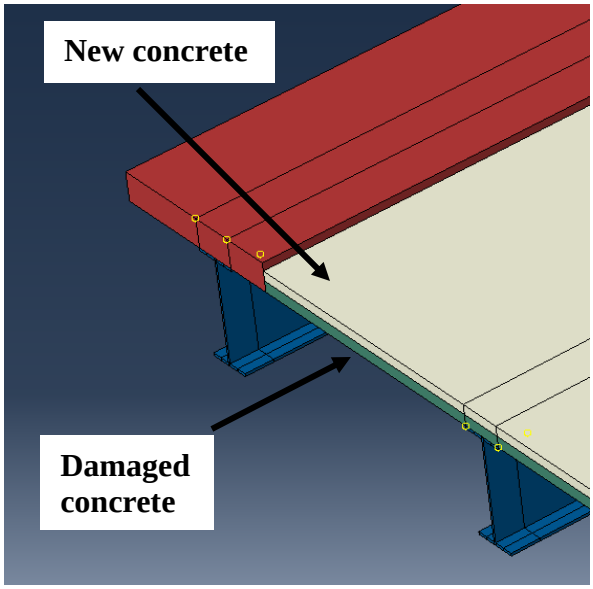

Figure 8- 1 New concrete and damaged concrete in ABAQUS interface

Table 8- 1 Comparison between the calibrated and retrofitted model.

Items	Calibrated Model	Retrofitted Model (4000 psi)	Retrofitted Model (6000 psi)	Remarks
Strain (με)	69	57	46	17% and 33% strain decrement
Deflection (in.)	0.51	0.48	0.47	5% and 7% decrease in deflection

Strain decreased considerably, even though there was no appreciable reduction in deflection on the deck top. 17% and 33% strain were reduced due to application of new concrete for 4 ksi and 6 ksi concrete strength.

8.2 Installation of CFRP strips/laminates underneath the concrete deck (Complete superstructure)

The proposed method is one of the popular methods now a days in concrete industry. For retrofitting of concrete structures CFRP wrapping is widely used all over the world. CFRP has high tensile strength which helps to increase the stiffness and strength of the structure. IE data

revealed that the concrete deck had suffered significant delamination. As the IE device can not specify the depth of delamination, we need to retrofit both positive and negative moment regions. For negative moment regions recasting of concrete was done previously. So, to modify the positive moment regions CFRP laminates were applied in the FE model. In the numerical model, CFRP strips with 75. 5 in. length and 20 in. width were used. CFRP was modeled as shell element. Composite elastic (Engineering Constant) material behavior was assumed. As CFRP sheet is an orthotropic material with high strength and modulus in the woven direction, it is recommended to use engineering constant to specify orthotropic material properties (ABAQUS). To make the model more reliable Hasim Damage properties (He et al. 2014) was also considered. In the model Simpson integration rule with five integration point was assumed. Four layers (0.019in. each) of CFRP was modeled. Composite layup model with conventional shell element type was used (Figure 8-2a). Different rotation angle was considered to stack the layers of CFRP. Though the bonding behavior was not the focus of the study the interaction between the CFRP, and concrete deck was considered as cohesive behavior to reflect the actual epoxy bonding condition. The CFRP strips were applied based on IE contour plots as shown in Figure 8-2b. All through CFRP strips were provided in the severe delaminated zone, whereas 20 in. spacing was used in moderate and no delamination zones to be cost-effective. All other parameters in the model remained the same as they were in the calibrated model.

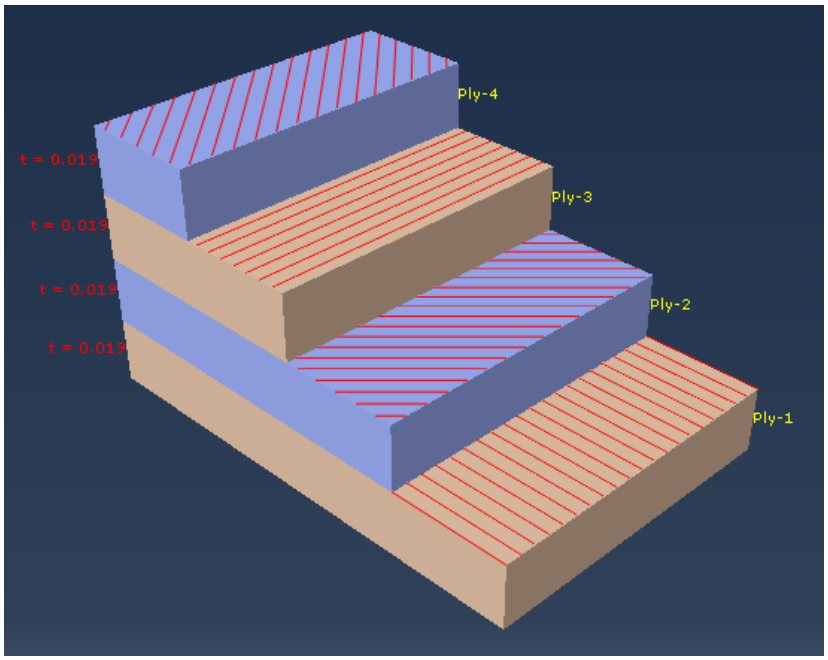

(a)

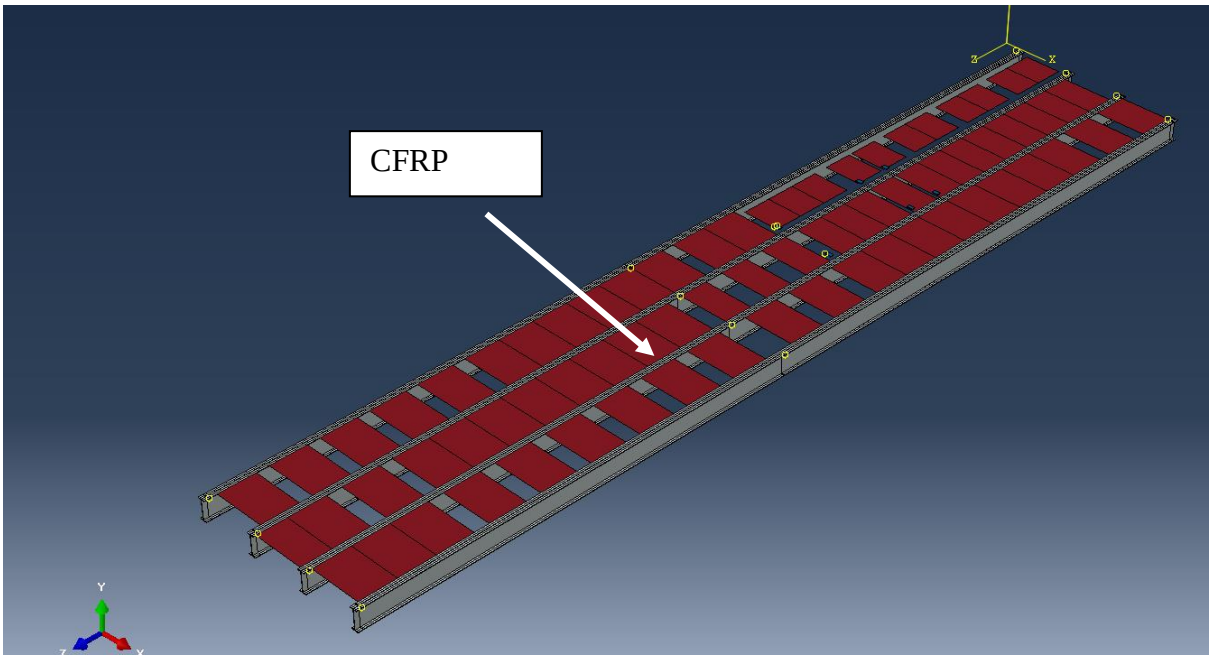

(b)

Figure 8- 2 CFRP laminates: (a) Composite layer stack up; (b) CFRP underneath the deck

The results showed a significant decrease in strain and deflection values compared to the calibrated model. The strain and deflection comparison for the calibrated and retrofitted models in the positive moment region (deck bottom concrete) are presented in Table 8-2.

Table 8- 2 Comparison between the calibrated model and the retrofitted model (CFRP laminate)

Items	**Calibrated Model**	**Retrofitted Model**	**Remarks**
Strain (με)	58	24	57% strain decrement
Deflection (in.)	0.52	0.30	40 % decrease in deflection

CFRP laminates significantly decreased the amount of strain and deflection that developed beneath the concrete. The strain recorded at the bottom of the CFRP was 47 με in the positive moment regions.

8.3 Installation of FRP I beams (Complete superstructure)

The suggested approach included the transverse placement of GFRP I beams beneath the concrete deck. The addition of GFRP I beams beneath the concrete deck increases the section's moment of inertia. The smaller I section is better because of lower dead load. The geometry and materials were considered according to De Waal et al. (2017). Isotropic materials behavior was assumed while modeling the GFRP I beam for simplicity. Isotropic behavior implies that the mechanical and thermal properties in the material are the same in all directions. The length of the GFRP beam was assumed 7 ft. The FRP I beam was modeled as solid element. As the I beam will be anchored with the bolt from the underneath, perfect bonding was considered in the modeling. Tie constraint was considered between the top surface of I beams and bottom surface of concrete. The spacing of the I beam was 30 in. c/c. 4 in. X 7 ft. rectangular area was partitioned underneath to ensure smooth constraint of the modeling. Figure 8-3 shows the application of CFRP I beams underneath the deck in the transverse direction. Due to computer capacity constraint and to reduce simulation time only one span of the model was retrofitted. Table 8-3 shows a comparison of strain and deflection of the deck bottom (positive moment region) concrete for the calibrated and retrofitted model. When compared to the calibrated model, the retrofitted numerical model findings revealed a substantial reduction in strain and deflection values.

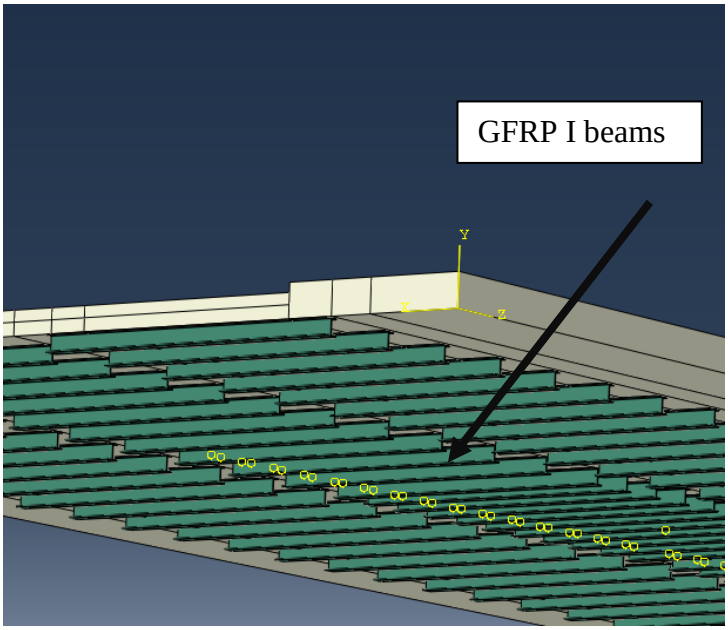

Figure 8- 3 CFRP I beam underneath the deck

Table 8- 3 Comparison of the strain and deflection between the calibrated and retrofitted model.

Items	Calibrated Model	Retrofitted Model	Remarks
Strain (με)	58	24	58 % strain reduction
Deflection (in.)	0.52	0.36	30% decrease in deflection

8.4 Installation of Steel I Joist (Complete superstructure)

Steel joists or steel I beams were placed below the concrete deck in the transverse direction according to the proposed approach. W 6X 8.5 was section was considered as joist. Material characteristics i.e., the modulus of elasticity was assumed 29000 ksi poison ratio (0.3), and yield strength was considered as 60 ksi. All of the modeling processes, including the installation of the steel joist were same as GFRP I beams installation. Steel joist or steel I beams have advantages over GFRP I beams, such as low materials cost, easily available but one major disadvantage is steel joists are corrosive, and heavy weight. The steel joists were anticipated to be 7 ft. in length. Because the joists would be attached with a bolt from below, precise bonding was taken into account during modeling. Between the top surface of I joists and the bottom surface of concrete, a tie constraint was considered. The I beam were spaced 30 in. apart. A rectangular area of 4 in. X 7 ft. was partitioned beneath to ensure seamless simulation of the modeling. Figure 8-4 illustrates the transverse application of steel I beams beneath the deck. Due to computer capacity constraints and a need to shorten simulation time, only one span of the model was retrofitted.

Table 8-4 presents the comparison of calibrated model and retrofitted model in terms of strain and deflection.

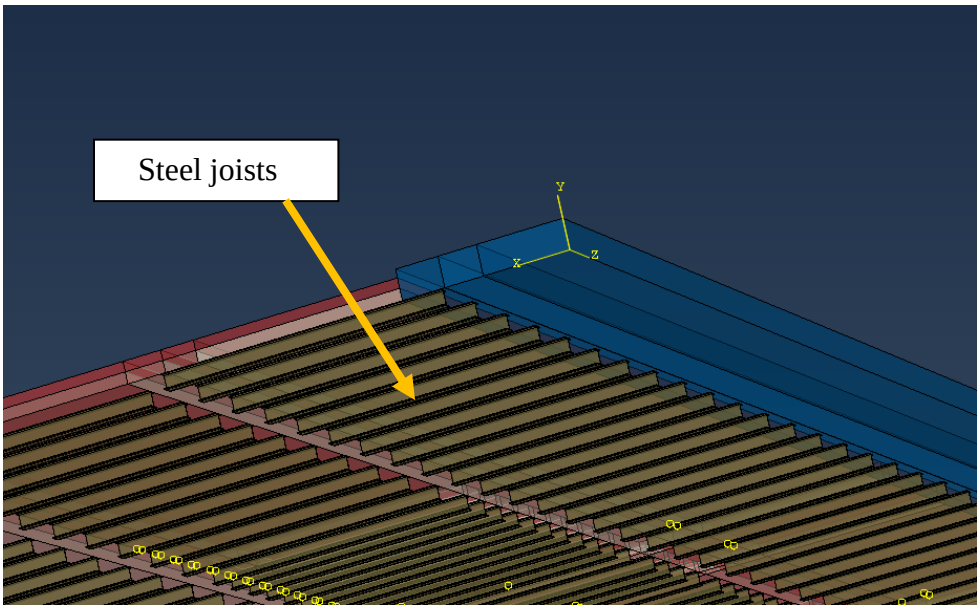

Figure 8- 4 Steel joist underneath the deck

Table 8- 4 Comparison of the strain and deflection between the calibrated and retrofitted model.

Items	Calibrated Model	Retrofitted Model	Remarks
Strain (με)	58	28	51 % strain reduction
Deflection (in.)	0.52	0.43	17% decrease in deflection

8.5 Installation of CFRP laminate on the Girder bottom Flange (Complete superstructure)

As shown by the load rating, girders were also unable to support HS-20 loads. As a result, girders must be retrofitted. One typical way of retrofitting steel girders is to place CFRP laminate on the necessary regions of the girder. Researchers have demonstrated the efficacy of this retrofit approach (as discussed in Chapter 2). CFRP laminate was placed on the bottom surface of the steel girders as well as on the top flange of the girders. The CFRP was modeled using the shell element method. The width of the CFRP was considered equal to girder total width 11.5 in. CFRP was modeled as orthotropic material using engineering constant material behavior (He et al. 2014). Hasim damage model was also assumed in the material properties. The interaction between the

CFRP laminates and steel girder was considered as tie constraint to ensure perfect bonding. Same modeling assumptions and techniques were followed as before i.e., CFRP laminate on concrete deck. This research is not concerned with bonding behavior between the interfaces. All the girders were retrofitted in the same procedure. Figure 8-5 shows the application of CFRP on steel girder. The comparison of calibrated model and retrofitted model is shown in Table 8-5. The values were extracted from bottom flange of the interior girder.

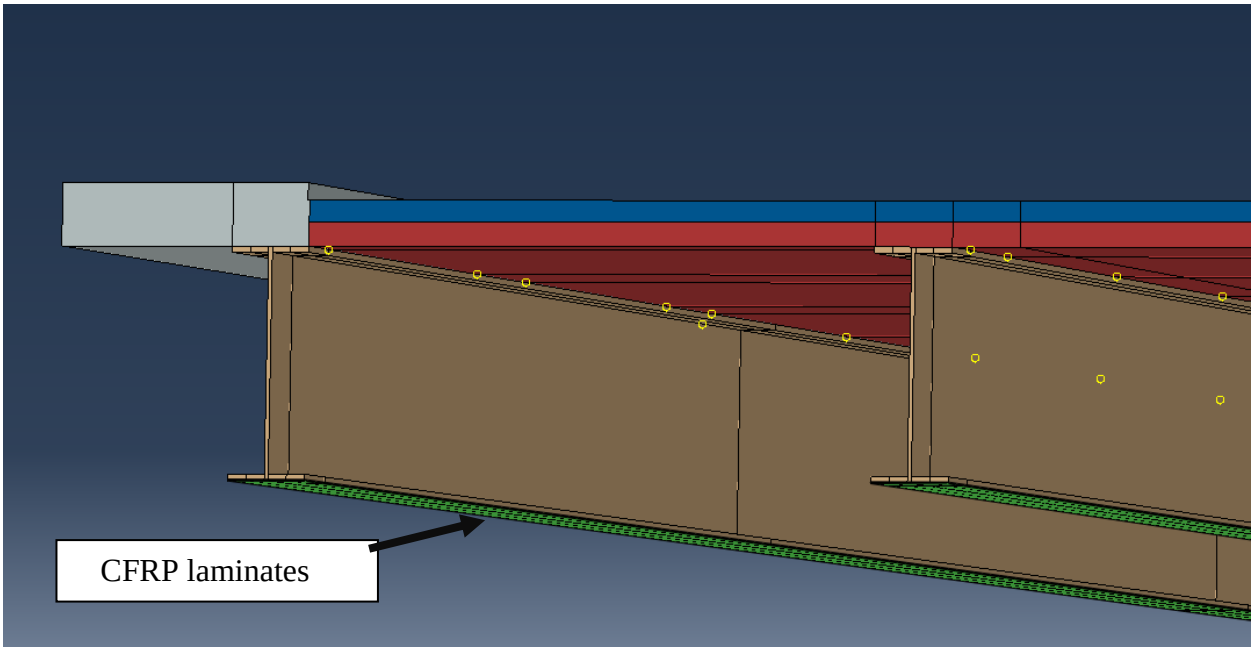

Figure 8- 5 CFRP laminates on the girder bottom flange

Table 8- 5 Comparison of the strain and deflection between the calibrated and retrofitted model.

Items	**Calibrated Model**	**Retrofitted Model**	**Remarks**
Strain (με)	190	151	22 % strain reduction
Deflection (in.)	0.49	0.44	10% decrease in deflection

8.6 Post-Tensioning of Steel Girder Using CFRP Rod (Complete superstructure)

The suggested approach illustrates local post-tensioning of steel girder. The post-tensioning rod is employed in this approach to balance the dead and live loads on the bridge. Although this technique is popular for reinforcing concrete beams, it was previously used on some steel girders bridges (see section 2). In the numerical model for posttensioning CFRP rods were used. Only in the positive moment zone of the girders were retrofitted for simplicity. Four jacking station was used per girder two on both sides to hold back the CFRP rod (Figure 8-6). The bottom of the jacking station was attached to the girder top surface of bottom flange and also tied with the web of the girder. Two ends of CFRP rod were embedded inside the jack station. All the calculations were done prior to modeling and attached in Appendix D. The required post tension stress was modeled using thermal load i.e., initial temperature. The temperature was modeled according to Ren et al. (2015). Thermal loading can be modeled precisely in multiple step modeling. The applied temperature for the required prestress can be obtained from Eq. 8-1.

$$C = -\frac{P}{C.E.A} \quad (8\text{-}1)$$

Where:

P = Prestressing force considering all losses

c = Coefficient of linear expansion

E = Modulus of elasticity of tendons

A = Cross-sectional area of the tendons

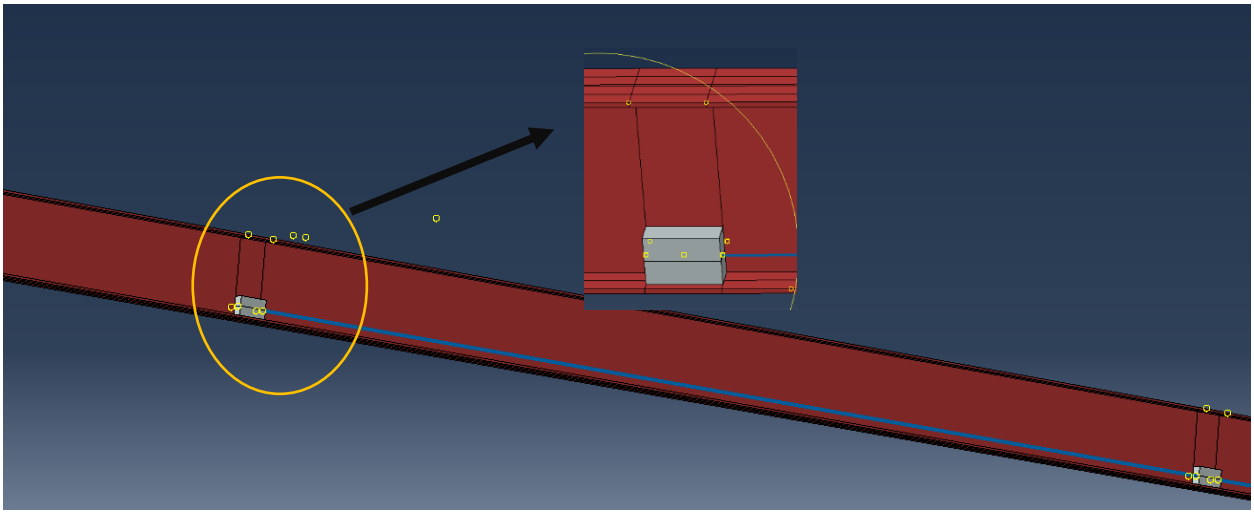

Figure 8- 6 Post-tensioning assembly in the FE model

Multistep modeling was considered in this case. Initially temperature was kept constant in the initial step and on the first step it was incorporated to the required stress corresponding value. For smooth simulation step time was divided in to three parts dead load, live load and post-stress load. Initially dead load was incorporated in the model, then in the next step the structure was post tensioned and finally live load were placed in the model.

Table 8- 6 Comparison of the strain and deflection between the calibrated and retrofitted model.

Items	**Calibrated Model**	**Retrofitted Model**	**Remarks**
Strain (με)	190	153	20 % strain reduction
Deflection (in.)	0.49	0.45	8% decrease in deflection

8.7 Installation of Shear Studs along the Girder Line (Complete superstructure)

One of the most often used methods for retrofitting non-composite bridges is to place shear connectors on the girder line and then recast the girder line concrete with fresh concrete. On the model, shear connector was employed to improve composite action. A solid element was used to simulate the shear connector geometry. The dimension of the round headed shear connector was extracted from studweldprod.com. Prior to modeling, the number of shear connectors necessary to achieve composite action was determined using the ASIC manual. Shear connectors were placed on the top surface of the top flange Shown in Figure 8-7a. Merge techniques were used to convert two different elements to make one element for simple modeling. Using merged technique all the shear connectors and steel girders were made one element assuming shear connectors had well bonding due to welding. Then in the numerical model cut geometry were assigned to make holes into the bridge deck to in the exact size of shear connector (Figure 8-7b).

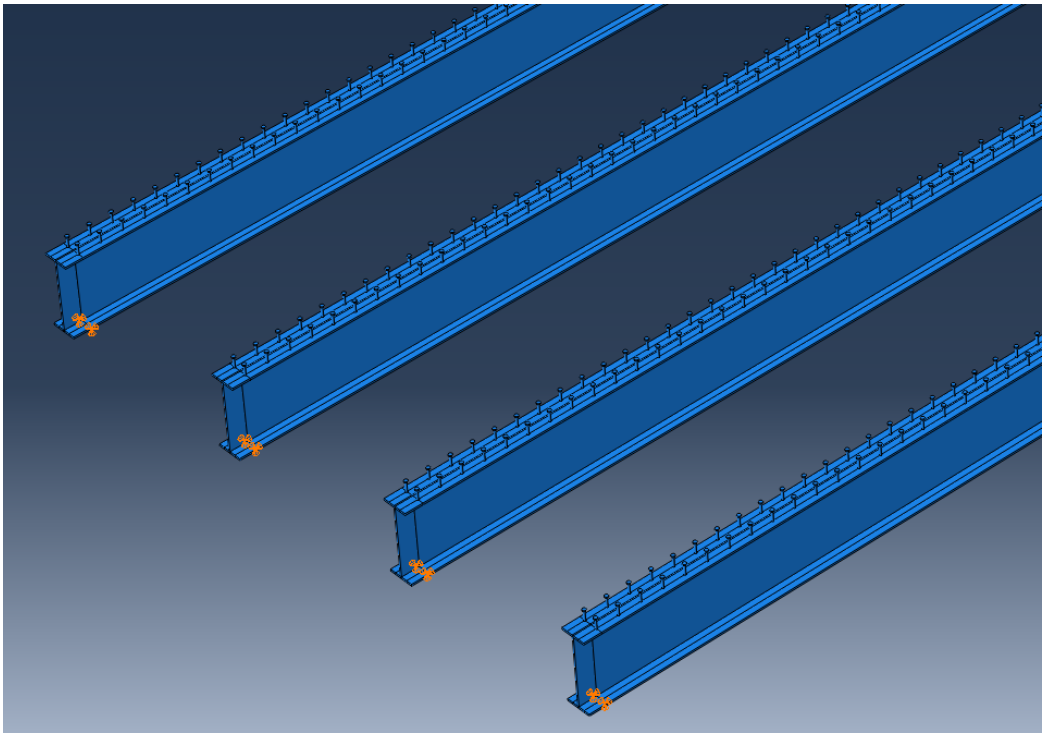

(a)

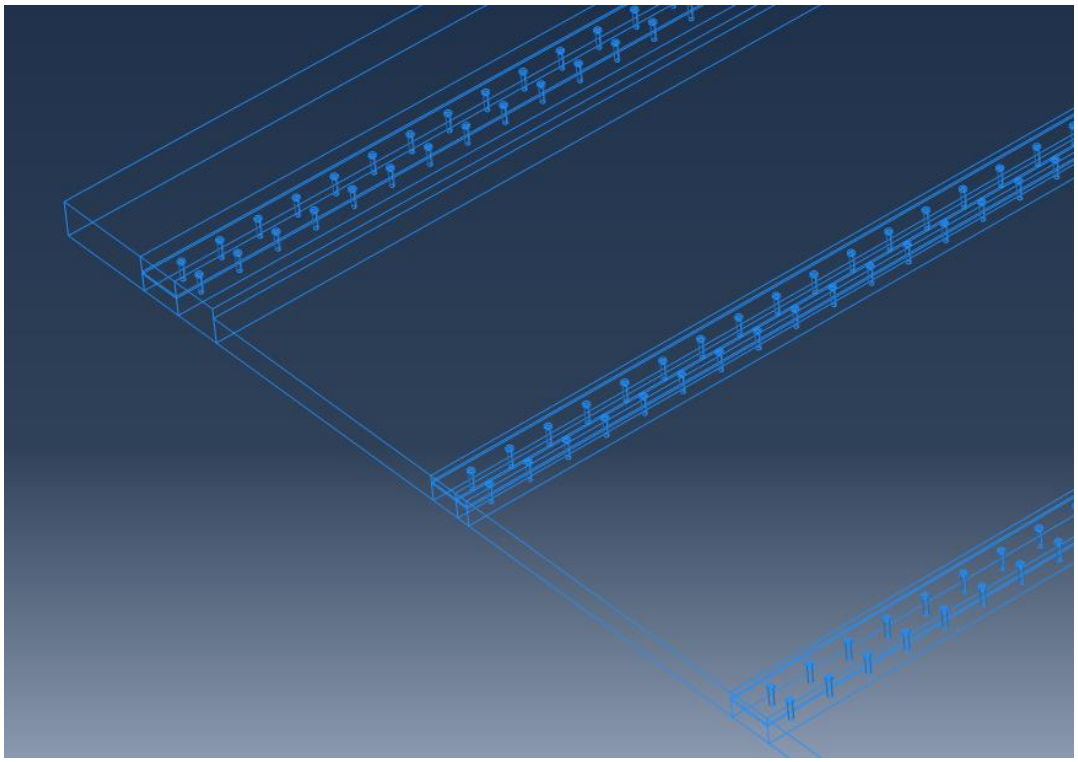

(b)

Figure 8- 7 (a)Shear connector on the girder; (b) holes in the concrete deck

Without merge techniques it was quite difficult to identify the concrete surfaces that was surrounded by whole shear connector. The interaction between the steel girders and concrete deck was assumed cohesive interaction as mentioned earlier. However, tie constrained was considered between the shear connector's whole surface and the portion surrounded by concrete. The concrete deck was partitioned same as the girder width to replace the cracked concrete properties with fresh concrete CDP model. The strength of the fresh concrete was assumed 6 ksi. Other parameters of the model remain same as before. One span of the model was retrofitted for time and technical constraint. As the model got complicated due to too many shear studs and holes in the concrete, different mesh techniques were used this particular case. Swipe mesh control was used to optimize the modeling. The comparison of calibrated model and retrofitted model is shown in Table 8-7.

Table 8- 7 Comparison of the strain and deflection between the calibrated and retrofitted model.

Items	**Calibrated Model**	**Retrofitted Model**	**Remarks**
Strain (με)	190	152	20% strain reduction
Deflection (in.)	0.44	0.32	27% decrease in deflection

8.8 Installation Headed Studs welded to a plate (Complete superstructure)

This technique of retrofitting requires the addition of a plate to the girder's upper flange. The studs are first welded to a separate plate and then attached to the girder's side. In the model initially shear stud were placed on top of the plate (Figure 8-8). After that, the plates were attached to both sides of the girder's top flange. Then same merge technique was used to make it one element. Otherwise, it became hard to identify surfaces. Cut geometry technique was used to create holes in the concrete deck. All the other modeling procedure were same as article 8.7. The comparison of calibrated model and retrofitted model is shown in Table 8-8.

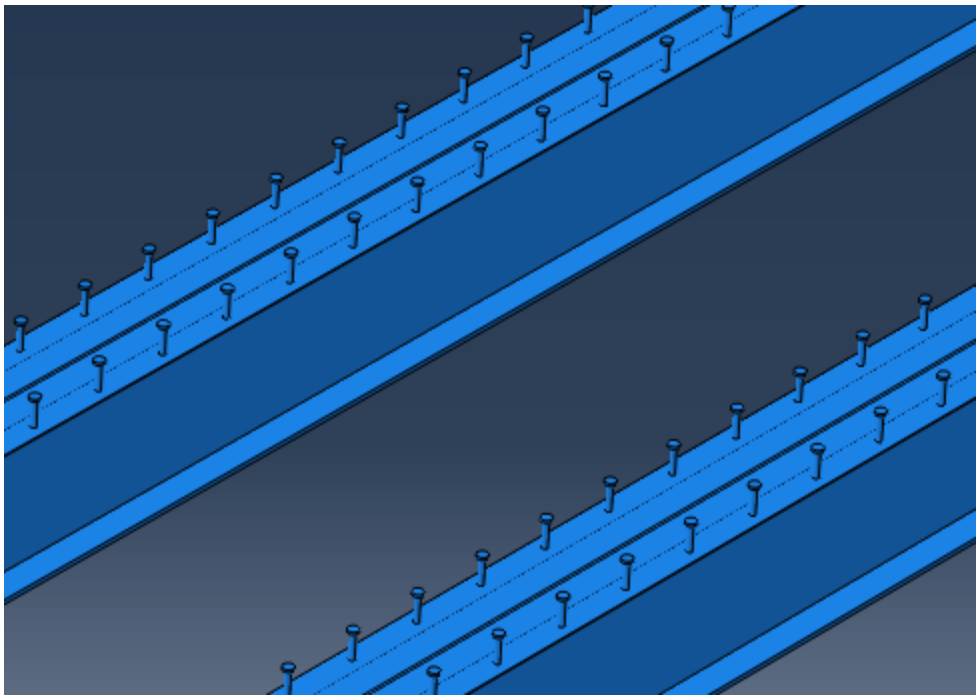

Figure 8- 8 Shear connector on steel plate

Table 8- 8 Comparison of the strain and deflection between the calibrated and retrofitted model.

Items	**Calibrated Model**	**Retrofitted Model**	**Remarks**
Strain (με)	190	154	18 % strain reduction
Deflection (in.)	0.44	0.33	25% decrease in deflection

All retrofits were incorporated to enhance flexural capacity; shear capacity was not taken into account in this investigation.

8.9 Cost Estimation:

One of the major aspects during cost calculation is to consider the cost for traffic closure. Installation of retrofitting options for work zone safety demands traffic control. A complete ramp closure as well as lane closure may be required for a lengthy period of time and/or restricted hours of intermittent stoppage during peak hours depending on retrofitting choices. Few retrofitting options requires lengthy traffic closure like GFRP or Steel joist installation underneath the deck, posttensioning of girder, weld shear connector, chipping of concrete. On the other hand, installation of CFRP laminates requires less time compared to other retrofitting options. Normally, lane closure needs signs, barricades, barriers and guardrail, attenuators, barrier accessories, channelizers (drums, pedestrian channelization devices, bicycle channelization devices), markers and delineators, etc. Table 8-9 shows the requirement of traffic closure during different retrofitting options.

Table 8- 9 Traffic closure remarks for each retrofitting options.

Retrofitting Options	**Remarks**
Chipping old deck concrete	No traffic closure needed for I-30 but for St. Francis Bridge
CFRP underneath the deck	Need to close I-30 but not St. Francis Bridge
GFRP Joist underneath the deck	Need to close I-30 but not St. Francis Bridge
Steel Joist underneath the deck	Need to close I-30 but not St. Francis Bridge
CFRP application on girder	Need to close I-30 but not St. Francis Bridge
Post-Tensioning of steel girder	Need to close I-30 and St. Francis Bridge
Welded Shear Connector	Need to close I-30 and St. Francis Bridge
Welded stud on steel plate	Need to close I-30 and St. Francis Bridge

From engineering point of view the retrofitting options should be effective and economic. Cost estimation is a required tool to make a decision to choose a suitable retrofitting option. For, this study, approximate cost analysis was done for all the retrofitting options. To calculate the repair cost TxDOT Standard Specifications for Construction and Maintenance of Highway, Streets, and Bridges (2014) was followed. As a supplementary materials of current cost TxDOT Average low Bid Unit Prices for the month of September was used. All the cost estimation includes materials cost, transportation cost, labor cost, and traffic closure (Appendix E). As the bridge is symmetric so, only three spans out of four spans were consider during calculation of initial installation cost. Table 8-10 presents the approximate cost for each retrofitting options.

Table 8- 10 Cost of each retrofitting options.

Items	**Retrofitting Options**	**Cost ($) (4 girders, 3 spans)**
Deck Retrofitting	Chipping old deck concrete	**$ 433,860**
	CFRP underneath the deck	**$ 180,880**
	GFRP Joist underneath the deck	**$ 258,840**
	Steel Joist underneath the deck	**$ 435,000**
Girder Retrofitting	CFRP application on girder	**$ 105,200**
	Post-Tensioning of steel girder	**$ 309,875**
Bridge Retrofitting	Welded shear connector	**$ 237,900**
	Welded stud on steel plate	**$ 360,062**

Due to the fact that both the concrete deck and steel girder were unable to support the HS 20 load, they required to be retrofitted. The cost for all the possible combined retrofitting options of the bridge is presented in Table 8-11.

Table 8- 11 Combined retrofitting cost

Combined Retrofitting	Cost
Concrete Chipping +CFRP underneath deck + CFRP under neath girder	$ 719,940
Concrete Chipping +CFRP underneath deck + Posttensioning of girder	$ 924,615
Concrete Chipping +GFRP underneath deck+ CFRP under neath girder	$ 797,900
Concrete Chipping +GFRP underneath deck + Posttensioning of girder	$ 1,002575
Concrete Chipping +Steel joist underneath deck + CFRP under neath girder	$ 974060
Concrete Chipping +Steel joist underneath deck + Posttensioning of girder	$ 1,178735
Concrete Chipping +Welded shear connector	$ 671,760
Concrete Chipping +Welded stud on steel plate	$ 793,922

For combined retrofit alternatives, concrete chipping for the negative moment zone, CFRP beneath the deck for the positive moment region, and CFRP wrap on the girder bottom are all viable possibilities. Additionally, a combination of concrete chipping and shear connectors may be used.

8.10 Load Rating of Retrofitted Deck and Girders

To get the rating factor, the load rating equation requires the capacity of the bridge member. Thus, to determine the capacity after retrofitting the concrete deck and steel girders were modeled independently and separately in ABAQUS.

8.10.1 Deck Modeling:

In theory, 1 ft. (305 mm) strip design is considered to calculate concrete deck capacity. The moment capacity of deck calculated in kip-ft/ft. To replicate the theoretical value, in the numerical model only 1 ft. strip of concrete deck was considered. Only three interior continuous deck spans were considered for simplify the model. The boundary condition was same as when deck sited on the girders. Both longitudinal and transverse rebars were considered. Considering the geometric characteristics, it appears as though a 1 ft strip was removed from the original concrete deck. Figure 8-9 shows the layout of three continuous spans.

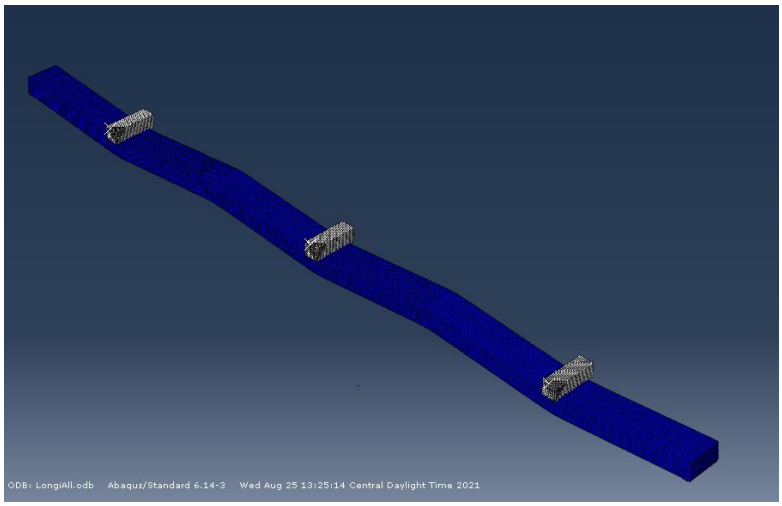

Figure 8- 9 1 ft. strip of concrete deck

All the materials properties of the model considered same as calibrated model. The capacity of the model was extracted from displacement control method. Static general solution was used in the ABAQUS solver. Larger displacement was provided so that materials fail after reaching its limit. A fictious rigid body was assigned on the top mid span of each individual spans. The interaction between rigid body and the concrete top was considered as friction interaction. A reference point was assigned on top of the rigid body. Initial boundary of the rigid body was considered fixed and in the next step it was modified and displacement in downward direction was provided. The downward displacement was provided on the reference point. For uniform displacement in the model smooth step amplitude was assumed. A smooth step helps the model to distribute the provided displacement in a smooth nonlinear way. After that general solution techniques in step 1 were modified to prevent premature failure. Then form the FE model reaction forces in the reference points and support reaction were extracted. Using this extracted values moment capacity was obtained through simple mechanics equations. Then using moment capacities deck load rating was performed.

All the retrofitting schemes were same as before. All the properties of the retrofitted model remain same in this separate deck model. To gain confidence in the modeling the moment capacity of the calibrated model was compared with hand calculation. Both the results showed a good agreement. shows the comparison of hand calculation and calibration model. Table 8-12 presents the comparison of moment capacities in positive and negative regions.

Table 8- 12 Comparison of hand calculation and calibration model.

Moment	Moment Capacity (theoretical)K-ft/ft	ABAQUS (K-ft/ft)
Positive	5.3	6.6
Negative	4.5	7.1

8.10.2 Deck Retrofitting and Rating

2.5 in. concrete chipping and new concrete overlay+ Installation of CFRP laminates:

On the 12 in. deck strip 2.5 in top concrete properties were replaced with 4 ksi concrete and CFRP laminates were attached to the deck bottom. The CFRP properties were used same as complete superstructure model. All the procedure were considered same as before. Figure 8-10 shows the retrofitted scheme of the deck.

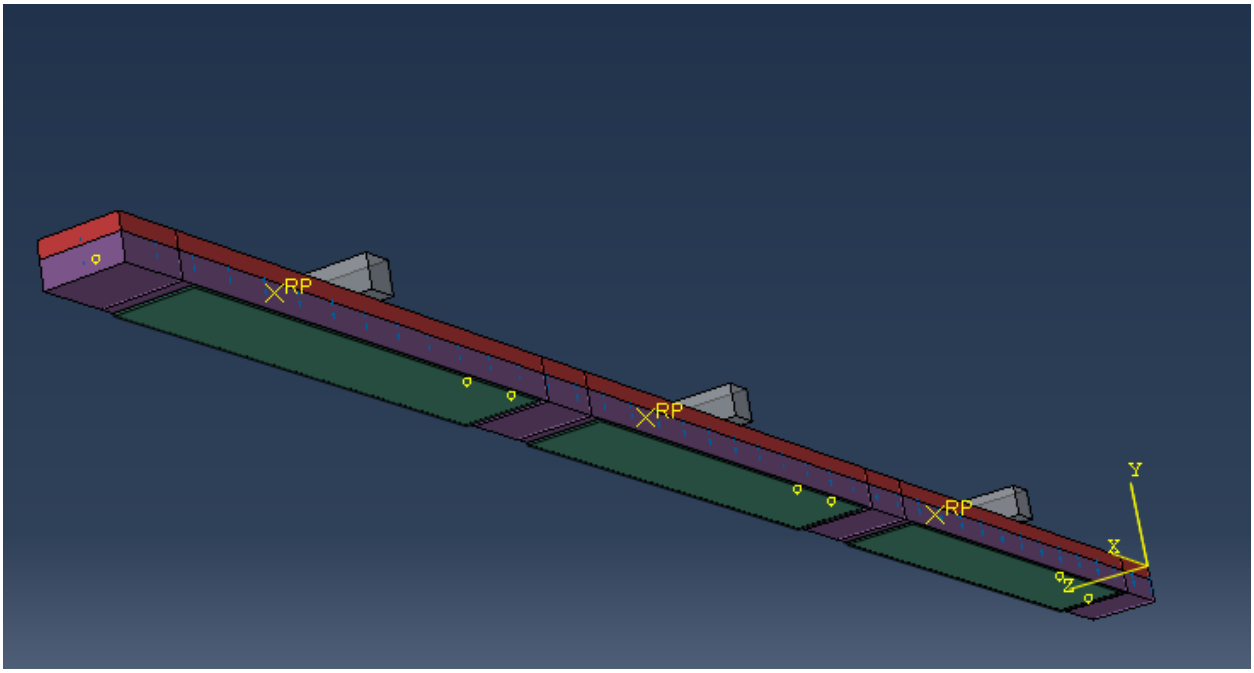

Figure 8- 10 CFRP laminates at deck bottom

2.5 in. concrete chipping and new concrete overlay+ Installation steel Joist:

On the 12 in. deck strip 3 in top concrete properties were replaced with 4 ksi concrete and steel I beams/joists were attached to the deck bottom. The geometric and materials properties of the model was considered same as complete superstructure model. To replicate the replicate bonding between the concrete surface and steel joist tie constraint is considered. The assumption of this model is that there still joists were connected to the bottom of the deck with anchor bolt. In these 12 feet model only one steel joist is considered underneath the deck. The assembly of the model is shown in Figure 8-11.

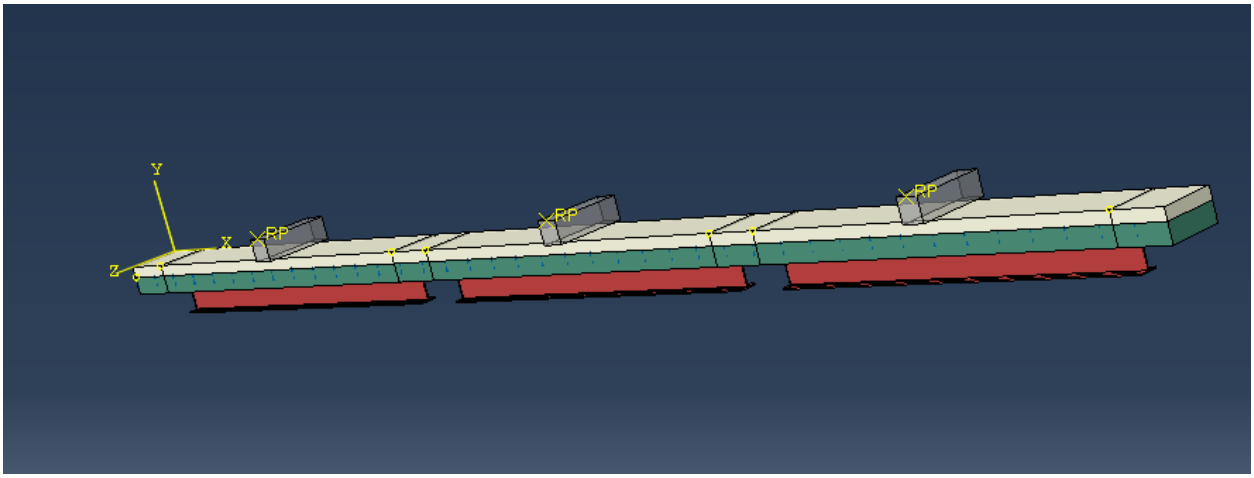

Figure 8- 11 Steel joist underneath the concrete

2.5 in. concrete chipping and new concrete overlay+ Installation of GFRP Joist:

On the 12 in. deck strip 3 in top concrete properties were replaced with 4 ksi concrete and steel I beams/joists were attached to the deck bottom. The geometric and materials properties of the model was considered as previous model. To replicate the replicate bonding between the concrete surface and steel joist tie constraint is considered. The assumption of this model is that there still joists were connected to the bottom of the deck with anchor bolt. In these 12 feet model only one steel joist is considered underneath the deck. The assembly of the model is shown in Figure 8-12

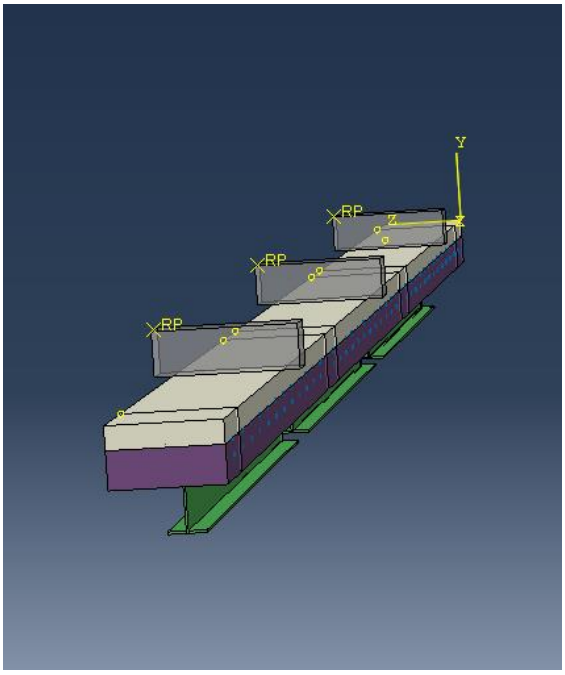

Figure 8- 12 GFRP Joist underneath the deck

The comparison of deck rating with different retrofitting options shown in Table 8-13.

Table 8- 13 Results for retrofitted deck rating

Retrofitting Options	**Rating factor Inventory level**	**Rating factor operating level**
Chipping old deck concrete + CFRP underneath the deck	1.71	2.85
Chipping old deck concrete + Steel Joist underneath the deck	1.92	3.2
Chipping old deck concrete + GFRP Joist underneath the deck	1.8	3.0

In case retrofitting deck rating positive moment rating governs and all the retrofitting options qualified for inventory rating more than 1.

8.10.3 Girder Retrofitting:

Only single girder was model. Two spans of the girders were considered. Geometry and materials properties of the girder was same as the whole bridge model. The boundary condition of the bridge was considered as pinned support. A larger displacement was added to ensure that materials fail when they approach their limit. Each individual span was centered on a fictitious stiff body. Friction interaction was used to describe the interaction between the stiff body and the concrete top. A reference point was chosen on the stiff body to include the displacement. The rigid body's initial boundary was deemed fixed and was changed in the next step to give displacement in the Y direction. A smooth step was also explored in the model's ramp portion. A smooth step enables the model to spread the displacement supplied in a nonlinear manner. Then, using simple mechanics equations, a finite element model based on reaction force and support reaction moment capacity was formed. Figure 8-13 shows the base model of the girder. Table 8-14 shows the comparison of the hand calculation and FE Modeling.

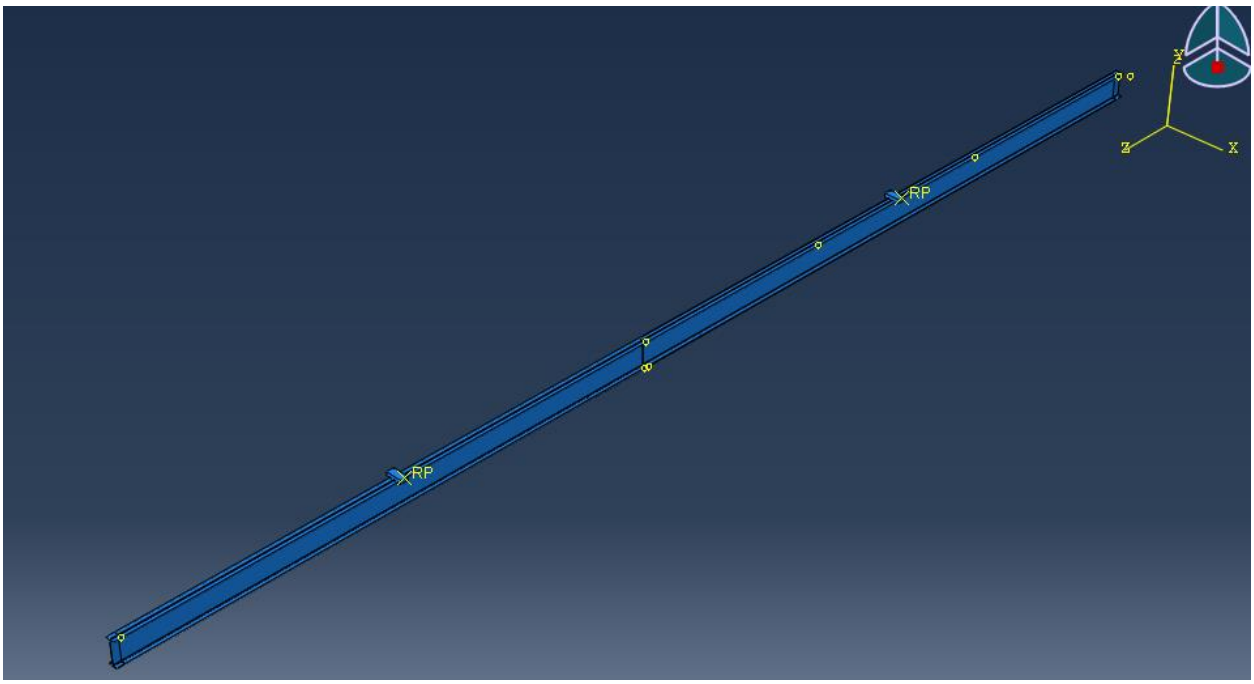

Figure 8- 13 Single girder modeling.

Table 8- 14 Comparison of capacity between theoretical and FE Model

Moment Capacity (theoretical)K-ft	ABAQUS (K-ft/ft)
1285	1393

8.10.4 Girder Retrofitting and Rating

CFRP Application on girder:

In this retrofitting method steel girder was post-tensioned in the positive moment zone to reduce the live load effect. Only positive moment zone was considered because of simplicity and for time efficiency for model running. CFRP was applied underneath the bottom flange. The interaction between the CFRP and steel girder was considered tie constraint. CFRP properties were same as the previous model. Displacement was provided until the failure occurred into the girder. The model assembly was provided in Figure 8-14.

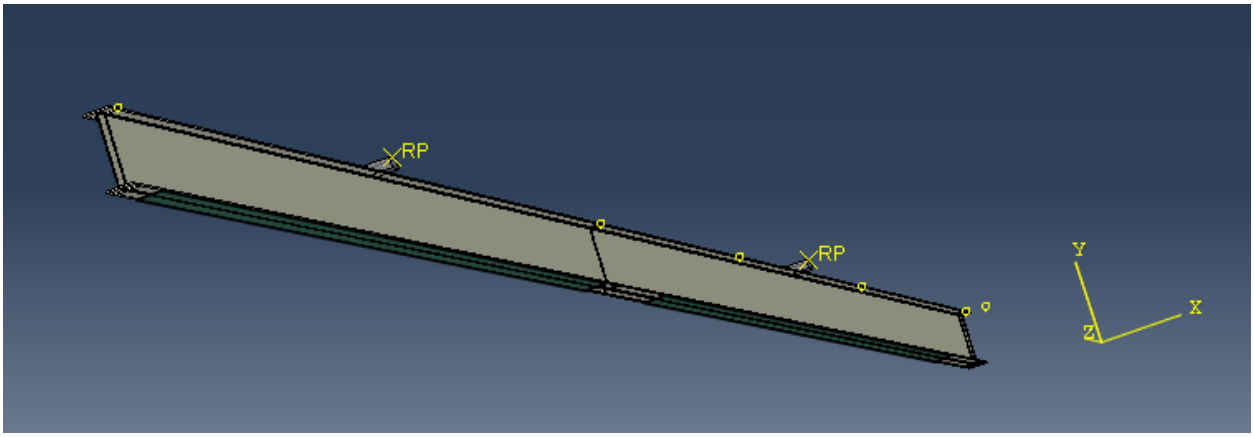

Figure 8- 14 CFRP application underneath the girder.

Local post-tensioning on girder:

This retrofitting method comprised of post-tensioning with CFRP rod along the girder line. CFRP was used over normal steel because CFRP can endure more stress. As CFRP can endure more stress the number of posttensioning rods requires less. The post tensioning force was determining prior to modeling. The prestressing force was applied as form of temperature. Posttensioning station was attached to side of the girder and top of the bottom flange of the girder. The post-tensioning rod was tie to the base station. The station was acting as a jack station. The assembly were shown in Figure 8-16. Table 8-15 shows the results for load rating after the girder was retrofitted.

Table 8- 15 Results for retrofitted girder rating

Retrofitting Options	Rating factor Inventory Level	Rating factor Operating Level
CFRP underneath the deck	1	1.6
Post tensioning of girder	1.1	1.8

8.10.5 Bridge Retrofitting and Rating

Installation of Headed Studs on the Girder Line:

In this part of the modeling only one girder and effective width of the deck (8ft.) was modeled. All the geometry and material properties were same the whole model. Shear connector were modeled as bolt and as solid element. Shear connectors were place on the top flange of the girders. Then bridge deck were punched through in the size of bolts. The number of shear connector required to gain full composite action was calculated prior to modeling according to ASIC manual. The bond between the stud surface and concrete was considered as tie constraint. Other parameters remain same in the model. After that, a rigid body was placed to provide displacement. Model assembly is presented in Figure 8-15.

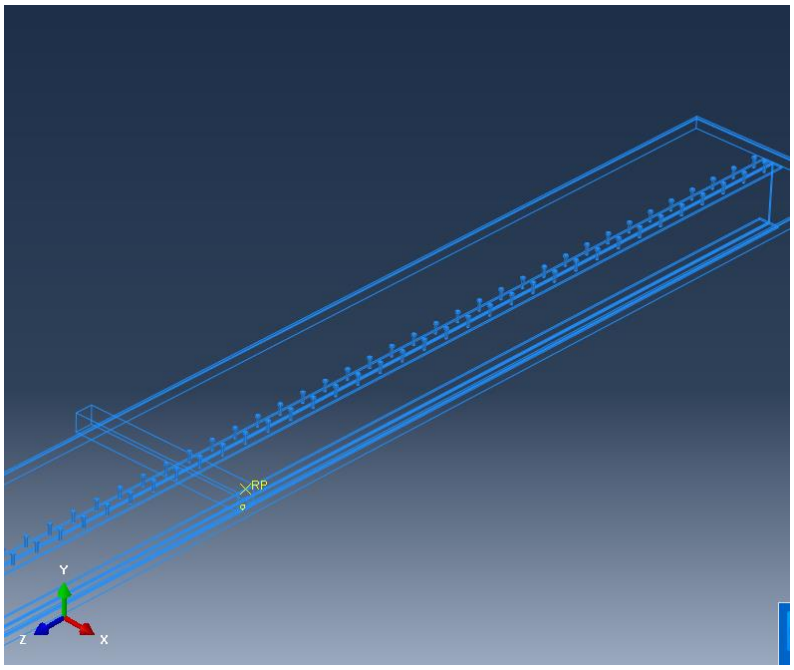

Figure 8- 15 Application of shear connector on girder top

Installation Headed Studs welded to a plate:

This very retrofitted model consisted of installation of extra plate at the top flange of the girder. The studs are welded to a separate plate and then welded to the side of the girder. Similar modeling approach was as mentioned before i.e., one girder and effective width of the deck. The shear connectors were modeled on the top of the plates. Then the plates were attached to the side of the girders. Assembly of the model was shown in Figure 8-16. Only positive moment rating was evaluated in case of bridge retrofitting.

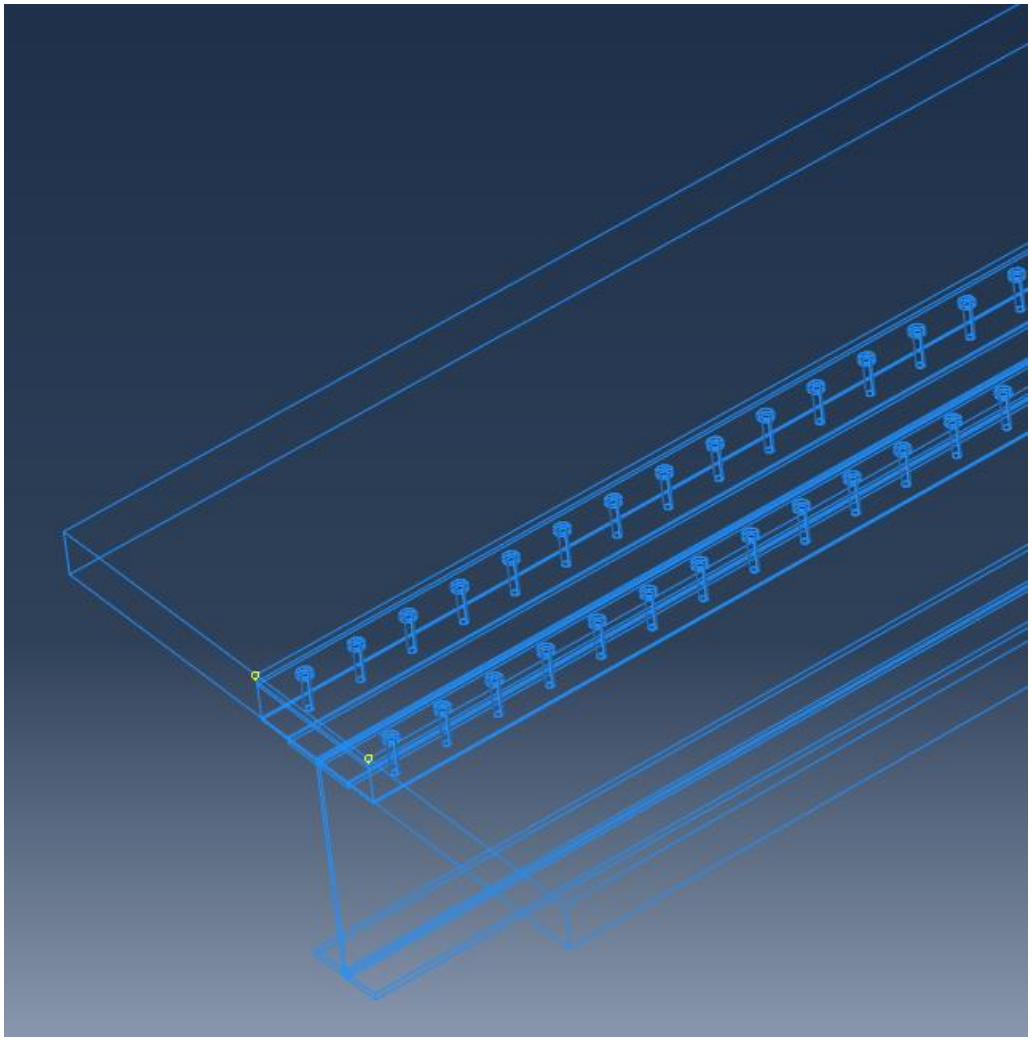

Figure 8- 16 Shear connector on steel plate

Table 8- 16 Bridge load rating after application of shear connector.

Retrofitting Options	Rating factor Inventory Level	Rating factor Operating Level
Welded Shear connector	1	1.66
Welded shear stud on plate	0.96	1.6

8.11 Decision tools for suitable retrofitting options

A temporary benefit-cost analysis was conducted to determine the most appropriate retrofit alternatives. As a benefit, only the inventory rating was evaluated, but as a cost, only the initial installation cost of each retrofit technique was examined. To begin, the load rating to starting cost ratio was computed. After that, the ratios were standardized to get a number between 1 and 10. The larger ratio results in a more appropriate answer. Figure 8-17 shows the plot of benefit/cost index.

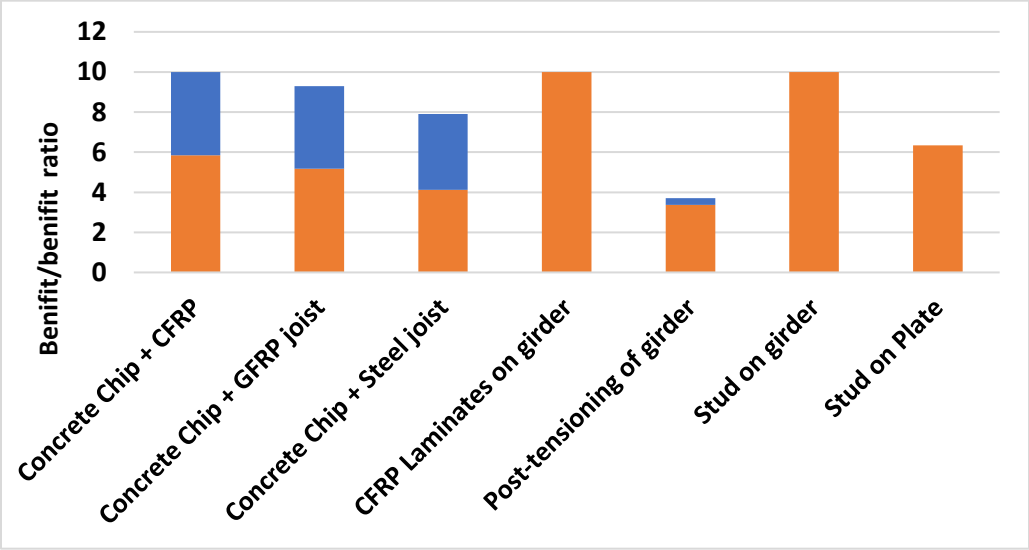

Figure 8- 17 Benefit/cost index

In the case of retrofitting a deck, concrete chip for the negative zone and CFRP for the positive zone achieve the maximum rating of 10, whereas in the case of retrofitting a girder, CFRP

laminates for the girder receive a higher rating of 10, and studs on the girder also receive the highest rating of 10.

The difference in color signifies the optimization of a rating criteria. When the rating factor is 1, the orange color indicates an optimized rating. For example, the rating factor for concrete chipping and CFRP beneath the concrete deck was 1.71 based on the benefit/cost index value 10. However, when the rating factor is 1, the concrete deck is capable of carrying HS-20. Thus, the benefit/index corresponding to RF 1 was 5.8, as indicated by the orange, whereas blue indicates complete retrofit performance.

A decision tree was developed based on inventory and operating levels to determine the most appropriate retrofit solutions. Figures 8-18a, 8-18b showed the conventional rating flow chart according to TxDOT 2020 and decision tree developed to take decision for suitable retrofitting options of posted bridge or to increase the load posting after retrofitting, respectively.

If the inventory rating is less than one but the operational rating is larger than one, this does not always indicate that the retrofit choice was unsuitable. Depending on the state of the bridge, several retrofit options can be used to optimize the bridge's load distribution. A flow chat was proposed to determine the effectiveness of retrofitting options as well as load posting (TxDOT, 2020). Figure 8-18 shows the flow chart for load posting.

Item Description for Flow Chart

According to TxDOT Coding Guide 2020 the items description is presented herein.

Item 58:

Theis item refers to over all condition rating of the deck. For example, concrete decks should be examined for cracks, scales, spalls, leaching, chloride contamination, potholes, delamination, and whole or partial failures. It is important to examine the steel grid decks for damaged welds, fractured grids and missing sections. There should be regular inspections of timber decking for signs of splitting or crushing as well as failure of fasteners or rot.

The condition of the wearing surface/protective system, joints, expansion devices, curbs, sidewalks, parapets, fascias, bridge rails, and scuppers should not be taken into account when evaluating the entire deck. Their condition, on the other hand, should be indicated on the inspection form.

Item 59:

This item specifies the physical state for every structural part. Cracking, degradation, section loss and bearing malfunction and misalignment should be investigated on the structural members.
On bridges where the deck is part of the superstructure, the condition rating of the superstructure may be impacted by the condition of the deck. If the girders have deteriorated or been damaged, the resulting superstructure condition rating may be lower than the deck condition rating.

Item 60

This item demonstrates the physical condition of piers, abutments, piles, fenders, footing or other components. A thorough inspection of all substructure components is necessary to detect indicators of distress, such as signs of cracking and section loss as well as signs of settlement, misalignment, scour and collision damage.

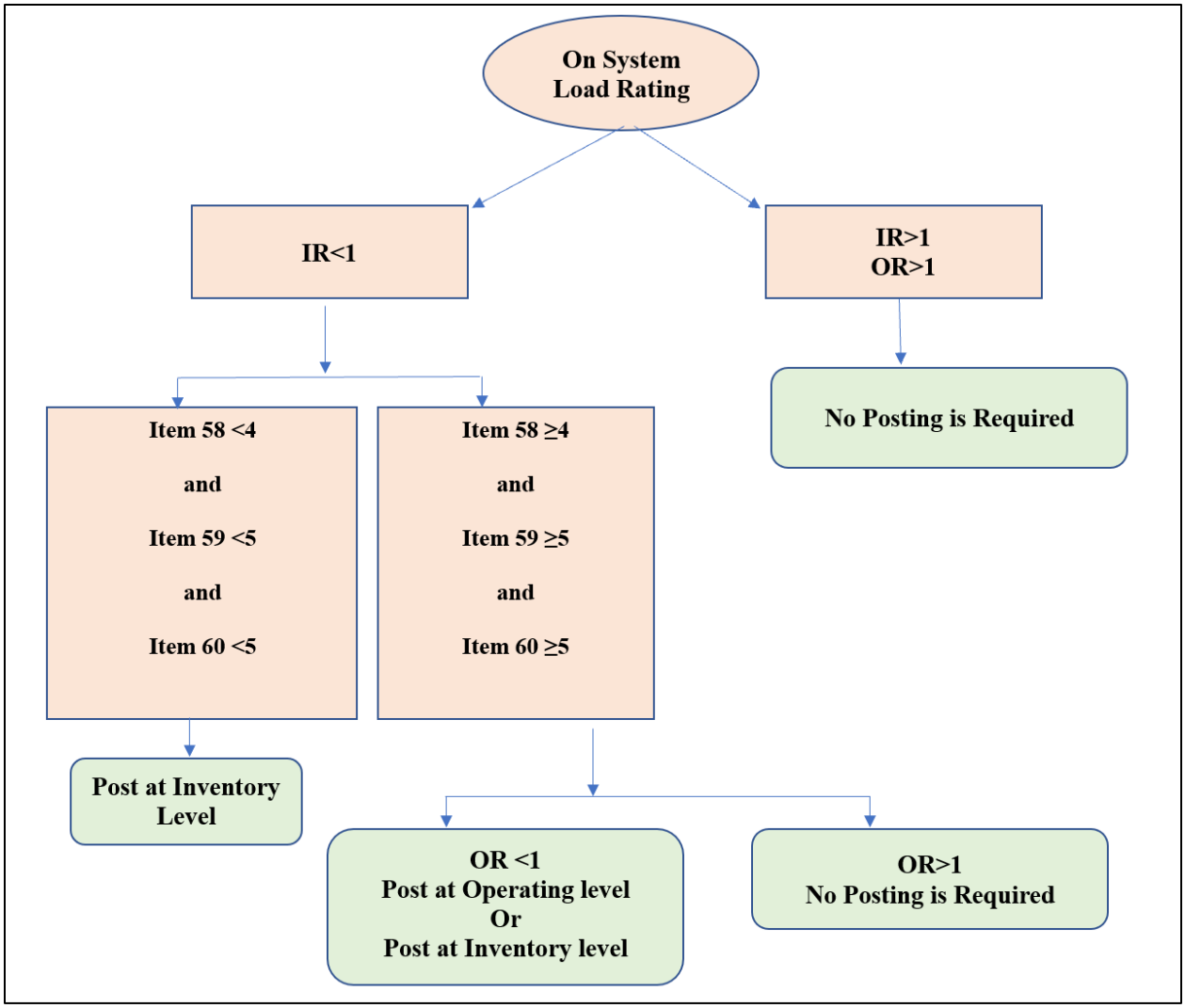
On System Load Rating
IR<1
IR>1 OR>1
Item 58 <4 and Item 59 <5 and Item 60 <5
Item 58 ≥4 and Item 59 ≥5 and Item 60 ≥5
No Posting is Required
Post at Inventory Level
OR <1 Post at Operating level Or Post at Inventory level
OR>1 No Posting is Required

(a)

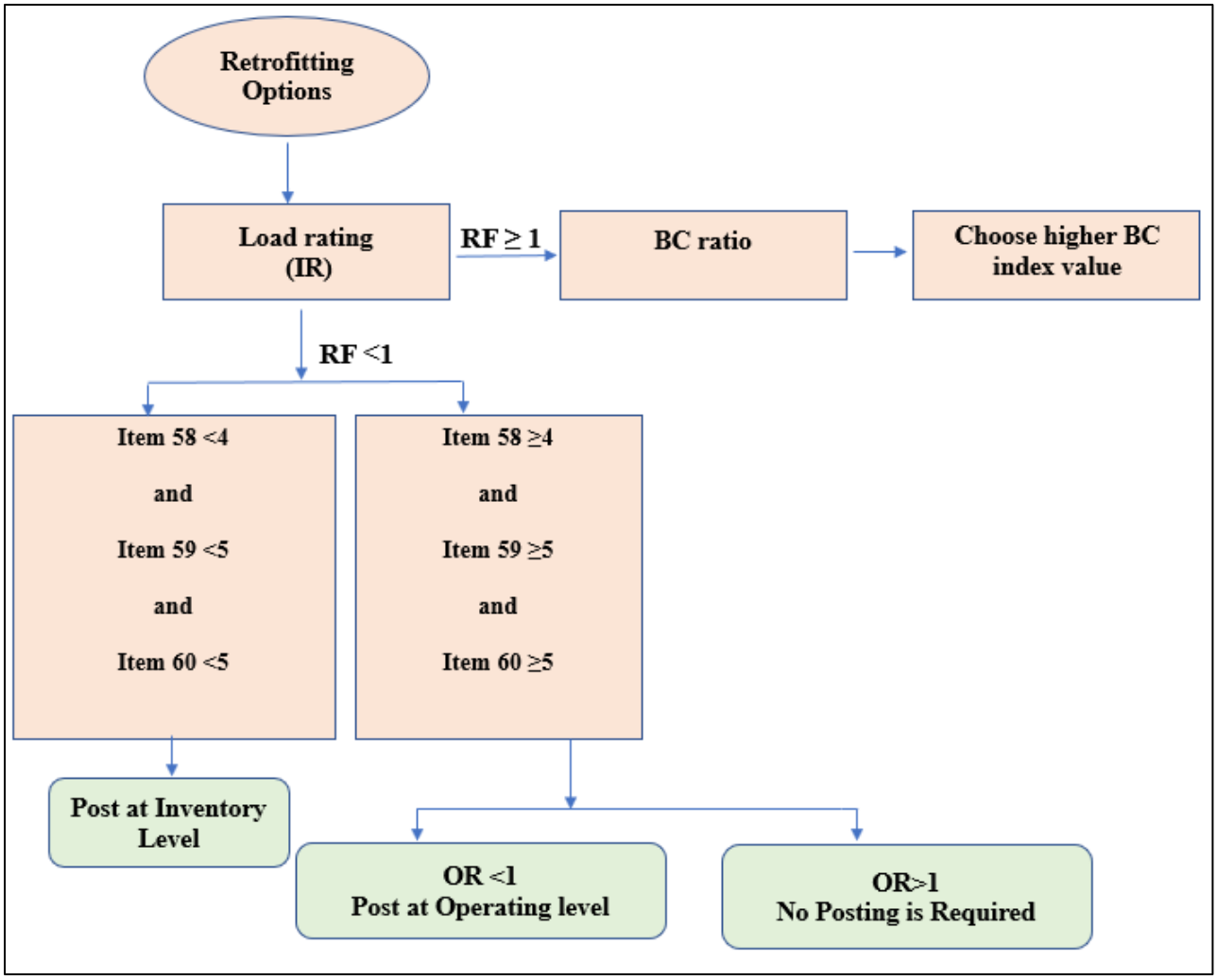

(b)

Figure 8- 18 Flow chart: (a) Conventional rating; (b) suitable retrofitting options and load posting

Chapter 9

CONCLUSION AND RECOMMENDATIONS

9.1 Summary:

St. Francis NB bridge was hit by overweight vehicle. Concrete deck and steel girders were severely damaged. Moreover, as the bridge was built in 1960's there was a lot of delamination and potholes were observed on the concrete deck. The bridge evaluation team at the University of Texas at Arlington was contacted by TxDOT personnel to help with a performance evaluation of the existing bridge. After that starting from a site visit, a comprehensive testing scheme comprising NDE assessment, Diagnostic load testing, Numerical Modeling, model calibration and different retrofitting options was developed and successfully carried out to evaluate performance of the bridge after retrofitting. The bridge's load rating was also assessed after various retrofitting methods were incorporated.

NDE assessment of the bridge was conducted using GPR and IE. Only damage continuous spans were considered for optimization. One day plan was developed to minimize the traffic closure effect. GPR data was used to identify the top rebars spacing of the deck as well as to plot a contour map for top rebars clear cover. On the other hand, IE data was used to plot the delamination contour plot. In addition, a diagnostic load was performed on the selected continuous spans. A detailed instrumentation plan was prepared to get the existing performance of the bridge. Strain gages were used to get live load response of the bridge while rotational tiltmeters were used to get end rotation of the girders during load testing. A novel approach was deported to load rate the existing bridge, different from conventional approach by incorporating NDE data in the load rating procedure.

To assess the bridge's performance at an extensive level, a static numerical model was created using bridge geometry, material properties, and boundary conditions. The model was developed with the help of ABAQUS CAE (ABAQUS 2016) software. Then FE model was calibrated using NDE and load test data. Following calibration, several retrofit methods were modeled, and their efficacy was assessed. Moreover, to find out the capacities of different retrofitting methods separate part instances model was developed. With the help of separate part instances modeling load rating was performed.

Along with load rating a rough approximate cost estimation was performed using TxDOT guidelines. Cost estimation includes material cost, labor cost, transportation cost, handling cost, traffic closure, and road user cost. Additionally, this chapter included recommendations for further research.

9.2 Findings and Conclusion:

After analysis NDE data, load test data, and FE model the following conclusions can be drawn from this study.

- The GPR data indicates that around 82.5% of the scanned deck area has a top cover ranges from 1.5 in-3 in and 71% deck area has top rebar cover more than specified in the as-built drawing. In some cases, this may occur as a result of a construction error or several concrete pours during repair. In light of a greater clear cover than specified, the moment capacity of the deck is compromised.
- IE contour plot demonstrate maximum severe delamination prevailed in the damaged deck section which was as a result of several previous damages. This is an indication that structural integrity and strength have been compromised in the concrete deck.
- Repeated run for each path showed almost identical strain values which indicated the reliability of the load test. Strain valve stated to increase from zero but did not return back to zero due to unintentional elastic slip of the strain gages. Span continuity was observed during the load test, making it necessary to use continuous behavior during live load calculation.
- AASHTO distribution factor were conservative compared to field load test. Damaged girder exhibit lower distribution factor.
- The average location of the N.A of the girders from load tests was on the web, which indicates a non-composite behavior between the girder and deck. The damaged section of the girder displayed NA behavior significantly lower, but the undamaged portion did not have any effect of the impact damage.
- Based on the GPR and IE results, an identical method was used to determine the rating of the bridge deck. Rebar spacing and top rebar cover used to determine the capacity of the deck were extracted from GPR data. The deck's capacity was reduced by applying average percentage delamination obtained from IE data. The concrete deck was unable to carry HS-

20 load in both inventory and operating level.

- Girder rating was calculated using moment distribution obtained from load tests. Damaged girder showed higher rating and able to carry HS-20 load due to lower distribution factor. As the damaged girder was replaced the capacity of the girder remain intact. Other girders B, C, and D were unable to carry HS-20 load in inventory level. In the case of operating level girder C and D were able to carry HS-20 while girders B was unable to carry.
- As the bridge rating is controlled by the lowest member rating of the bridge components, in this study the bridge rating was governed by deck rating (operating level) which was 23,760 lb. The operating is considered because during rating calculation the capacity was reduced in a very conservative way.
- There is no prior study that has been conducted to determine the load rating of a non-composite bridge. In this field, this study can be a milestone.
- Numerical model was calibrated by changing damage concrete strength and stiffness in the interface between steel girder and concrete interface. The strain values at the girder bottom and rotation values at the girders end showed a good correlation.
- The accuracy of the FEM models was verified by stability check using the residual energy method. Furthermore, mesh sensitivity analysis was performed to obtained accurate results.
- Concrete chipping can minimize strain in the negative moment zone by up to 33%. On the other hand, retrofitting options in the positive moment zone can result in a reduction of up to 57%. Additionally, girder retrofit solutions can lower girder strain by up to 22% at the bottom of the girder.
- The use of shear connectors can reduce strain by up to 22%. Additionally, all retrofit methods can greatly minimize deflection significantly.
- Unique load rating procedure was introduced after retrofitting to load rate bridge members.
- The deck rating after retrofitting was greater than one in both inventory and operating level, indicating that all retrofit solutions are applicable in different circumstances, however, CFRP laminates were a cost-effective choice based on cost analysis.
- Additionally, the load rating of the repaired girder was greater than one at both the inventory and operational levels. Both techniques were satisfactory, but cost analysis indicated that CFRP laminates were the most economical option.

- After applying the shear connector, the load rating was less than one for inventory level but more than one for operational level. Shear studs on the top flange of the girder is a cost-effective solution.
- Due to the inability of the deck and girders to support HS-20, both must be retrofitted. To improve the moment capacity in the negative zone, concrete chipping is the only choice, whereas CFRP beneath the deck was a good alternative for positive zone reinforcement. Additionally, girders must be reinforced using CFRP laminates.
- Another suitable option is to chip delaminated concrete and the concrete along the girder line, install a shear stud on the girder, and recast with fresh concrete.
- A decision tool was developed to assist in selecting the most cost-effective retrofit solution.

9.3 Further Research:

- In load rating procedure the capacity of the bridge was considered assuming full composite action but there is no prior research on capacity calculation partial composite action in case of steel girder bridge. So, capacity of the bridge can be calculated assuming partial composite action.
- Live load can apply in the model as a moving load instead of patch load to get more reliable and accurate responses.
- Fracture and fatigue analysis during FEM can be considered.
- The efficacy and expense of replacing all girders with 65 ksi steel while maintaining the same height of steel beam 33 X130 can be explored.
- The contribution of lateral support in the event of a collision can be investigated.
- In case of some retrofitting options only one span was modeled due to capacity and model run time constrain. Further study can be to retrofit the whole bridge.
- Parametric studies can be performed to find the optimum spacing during deck retrofitting using steel joists and GFRP I beam.
- Load rating can be performed using other FRP materials and effectiveness can be compared.

- A comprehensive benefit/cost analysis may be conducted, taking into account all relevant elements, such as maintenance, inspection, constructability, environmental, equity, and transportation consequences.

Appendix A

Deck capacity calculation from GPR and Impact Eco data

Positive Moment Capacity:

Design $12''$ strip, #5 @ $6.5''$ O.C (obtained from GPR data)

$$A_s = 0.572\ in^2, in\ 12''$$

$$F_y = 40\ ksi, \qquad f'_c = 3ksi$$

$$cover = 1 \cdot 5''(bottom\ cover, from\ drawing)$$

$$a = \frac{A_s F_y}{0.85 f'_c b} = \frac{0.572 \times 40}{0.85 \times 3 \times 12} = 0.75''$$

$$d = 6.5'' - 1.5'' = 5''$$

$$M_n{}^+ = A_s F_y \left(d - \frac{a}{2}\right) = 0.572 \times 40 \times \left(5 - \frac{0.75}{2}\right)$$

$$= 106\ k - in$$

$$= 8.82\ k - ft.$$

$$\rho_{max} = 0.85 \times \beta_1 \times \frac{f'_c}{f_y} \frac{0.003}{0.003 + \epsilon_t}$$

$$= 0.85 \times 0.85 \times \frac{3}{36} \times \frac{0.003}{0.003 + 0.005}$$

$$= 0.023$$

$$\rho = \frac{A_s}{bd} = \frac{0.572}{12 \times 5} = 0.009$$

Since, $< \rho_{max}$, tension controlled

$$\emptyset = 0.9$$

$$\emptyset M_n{}^+ = 0.9 \times 8.82$$

$$= 7.94\ k - ft.$$

From, Impact Eco, average % delamination is 40%. Modified moment capacity from IE →

$$\emptyset M_n{}^+ = 7.94 \times (100 - 45)\%$$

$$= 4.8\ k - ft.$$

Negative Moment Capacity:

From GPR data, top cover $= 2''$

$$d = 6.5 - 2 - \frac{5}{8 \times 2} = 4.2''$$

$$[80\%\ cover\ is\ 2''at\ negative\ moment\ zone]$$

$$M_n{}^{-} = A_s F_y \left(d - \frac{a}{2}\right)$$

$$= 0.572 \times 40 \times \left(4.2 - \frac{0.75}{2}\right)$$

$$= 87.52\ k - in$$

$$= 7.3\ k - ft.$$

$$\emptyset M_n{}^{-} = 6.57\ k - ft.$$

From Impact Eco, average % delamination is 40%. Modified moment capacity from IE →

$$\emptyset M_n{}^{-} = 6.57X(100 - 40)\%\ k - ft.$$

$$= 3.94\ k - ft.$$

Appendix B

Deck Rating:

$$DL = 0.1 * \left(\frac{6.5}{12} * 1' * 0.15\right) * 8^2$$

$$= 0.52\ k - ft$$

$$LL = 0.8 * \left(\frac{S+2}{32}\right) * P$$

$$= 0.8 * \left(\frac{8+2}{32}\right) * 16$$

$$= 4\ k - ft$$

LL equation is for continuous slab, P=16 kip for HS-20.

$$LL + IM = 1.3 * 4\ {}^{k-ft}/_{ft}$$

$$= 5.2\ k - ft$$

Positive Moment Rating

R.F. For HS-20 (Inventory level): **(Include 40% delamination and $\emptyset = 0.9$)**

$$RF = \frac{C - A1\ X\ DL}{A2\ X\ (LL + IM)}$$

$$= \frac{4.8 - 1.3 * 0.52}{2.17 * 5.2}$$

$$= 0.36$$

Bridge Member rating = 36*0.36

= 12.96 tons

=25920 lb.

R.F. For HS-20 (Inventory level): **(Include only 40% delamination)**

$$RF = \frac{C - A1\ X\ DL}{A2\ X\ (LL + IM)}$$

$$= \frac{8.82 * 0.6 - 1.3 * 0.52}{2.17 * 5.2}$$

$$= 0.41$$

Bridge Member rating = 36*0.41

= 14.76 tons

=29520 lb.

R.F. For HS-20 (operating level): **(Include 40% delamination and $\emptyset = \mathbf{0.9}$)**

$$RF = \frac{C - A1\ X\ DL}{A2\ X\ (LL + IM)}$$

$$= \frac{4.8 - 1.3 * 0.52}{1.3 * 5.2}$$

$$= 0.61$$

Bridge Member rating = 36*0.61

= 21.96 tons

=43920 lb.

R.F. For HS-20 (operating level): **(Include 40% delamination)**

$$RF = \frac{C - A1\ X\ DL}{A2\ X\ (LL + IM)}$$

$$= \frac{8.82 * 0.6 - 1.3 * 0.52}{1.3 * 5.2}$$

$$= 0.68$$

Bridge Member rating = 36*0.68

= 24.48 tons

=48960 lb.

Negative Moment Rating:

R.F. For HS-20 (Inventory level): **(Include 40% delamination and $\emptyset = \mathbf{0.9}$)**

$$RF = \frac{C - A1\ X\ DL}{A2\ X\ (LL + IM)}$$

$$= \frac{3.94 - 1.3 * 0.52}{2.17 * 5.2}$$

$$= 0.3$$

Bridge Member rating = 36*0.3

= 10.8 tons

=21600 lb.

R.F. For HS-20 (Inventory level): **(Include only 40% delamination)**

$$RF = \frac{C - A1\ X\ DL}{A2\ X\ (LL + IM)}$$

$$= \frac{7.3 * 0.6 - 1.3 * 0.52}{2.17 * 5.2}$$

$$= 0.33$$

Bridge Member rating = 36*0.33

= 11.88 tons

=23760 lb.

R.F. For HS-20 (operating level): **(Include 40% delamination and $\emptyset = 0.9$)**

$$RF = \frac{C - A1\ X\ DL}{A2\ X\ (LL + IM)}$$

$$= \frac{4.8 - 1.3 * 0.52}{1.3 * 5.2}$$

$$= 0.48$$

Bridge Member rating = 36*0.48

= 17.28 tons

=34560 lb.

R.F. For HS-20 (operating level): **(Include 40% delamination)**

$$RF = \frac{C - A1\ X\ DL}{A2\ X\ (LL + IM)}$$

$$= \frac{7.3 * .6 - 1.3 * 0.52}{1.3 * 5.2}$$

$$= 0.55$$

Bridge Member rating = 36*0.55

= 19.8 tons

=39600 lb.

Appendix C

Load rating (LFR)

Dead load calculation:

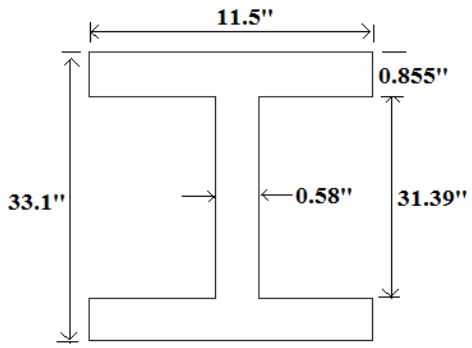

• Deck self-wt. = $8' \times \frac{6.5}{12} \times 0.150 = 0.65 \frac{k}{ft.}$

• Girder self-wt. = $0.130 \times 1.06 = 0.14 \frac{k}{ft.}$

• Bottom plate = $\frac{0.625 \times 10 \times \frac{0.49}{144} \times 14}{70} = 0.0043 \ \frac{k}{ft.}$

• Parapet = $\frac{32}{12} \times \frac{19}{12} \times 0.15 \times \frac{1}{4} = 0.16 \ \frac{k}{ft.}$

• Curbs = $3.3' \times \frac{4}{12} \times 0.15 \times \frac{2curbs}{4beams} = 0.083 \ \frac{k}{ft.}$

• Diaphragms = $\frac{0.05 \times 5 \times 8 \times 1.06}{70} = 0.03 \ \frac{k}{ft.}$

• Railings = $0.02 \times \frac{1}{4} = 0.005 \ \frac{k}{ft.}$

• Haunch = $0.03 \frac{k}{ft.}$ [assume]

Total Dead Load = $1.1 \frac{k}{ft.}$

Dead load moment = $\frac{1}{14}(1.1) \times 70^2$

$= 385$ k-ft. and From SAP analysis = 411.29 k-ft

Compute Nominal flexural Resistance of section:

Capacity C=Mu= Fy X Z =33 ksi * 467= 1285 k-ft

Live Load Analysis: (Conventional Method)

Live load distribution factor:

Two or more land loaded → (Interior girder)

$$g_{m_1} = \frac{S}{5.5}$$

$$= \frac{8}{5.5}$$

$$= 1.45 \text{ wheels}$$

Two or more land loaded → (Exterior girder)

8.0/8.0 P + 2.0/8.0 P = 1.25 wheels

Impact Factor:

$$I = \frac{50}{L+125} <= 0.3$$

$$= \frac{50}{70 + 125}$$

$$= 0.26$$

Live load for HS-20 (70 ft) for interior girder = 788*1.26*1.45*.5=720 k-ft

Live load for HS-20 (70 ft) for exterior girder = 788*1.26*1.25*.5=621 k-ft

Girder Rating (Conventional Method)

R.F. For HS-20 (Inventory level): **(Interior girder)**

$$RF = \frac{C - A1XDL}{A2X(LL + IM)}$$

$$= \frac{1285 - 1.3 * 411.29}{2.17 * 720}$$

$$= 0..48$$

Bridge Member rating = 36*0.48

= 17.28 tons

= 34560 lb.

R.F. For HS-20 (Inventory level): **(Exterior girder)**

$$RF = \frac{C - A1XDL}{A2X(LL + IM)}$$

$$= \frac{1285 - 1.3 * 411.29}{2.17 * 621}$$

$$= 0.55$$

Bridge Member rating = 36*0.55

= 19.8 tons

=39600lb.

R.F. For HS-20 (Operating level): **(Interior girder)**

$$RF = \frac{C - A1XDL}{A2X(LL + IM)}$$

$$= \frac{1285 - 1.3 * 411.29}{1.3 * 720}$$

$$= 0.8$$

Bridge Member rating = 36*0.8

= 28.8 tons

=57600 lb.

R.F. For HS-20 (Operating level): **(Exterior girder)**

$$RF = \frac{C - A1XDL}{A2X(LL + IM)}$$

$$= \frac{1285 - 1.3 * 411.29}{1.3 * 621}$$

$$= 0..92$$

Bridge Member rating = 36*0.92

= 33.12 tons

=66240 lb.

Live load moment calculations for girders:

Girder A = 788 *1.26*0.12= 120 k-ft

Girder B= 788 *1.26*0.61= 606 k-ft

Girder C = 788 *1.26*0.4= 397 k-ft

Girder D = 788 *1.26*0.43= 427 k-ft

Girder Rating (Modified Method)

R.F. For HS-20 (Inventory level): **(Exterior girder-A)**

$$RF = \frac{C - A1XDL}{A2X(LL + IM)}$$

$$= \frac{1285 - 1.3 * 411.29}{2.17 * 120}$$

$$= 2.88$$

Bridge Member rating = 36*2.88

= 103.6 tons

= 207,360 lb.

R.F. For HS-20 (Operating level): **(Exterior girder-A)**

$$RF = \frac{C - A1XDL}{A2X(LL + IM)}$$

$$= \frac{1285 - 1.3 * 411.29}{1.3 * 120}$$

$$= 4.8$$

Bridge Member rating = 36*4.8

= 28.8 tons

=345,600lb.

R.F. For HS-20 (Inventory level): **(Interior girder-B)**

$$RF = \frac{C - A1XDL}{A2X(LL + IM)}$$

$$= \frac{1285 - 1.3 * 411.29}{2.17 * 606}$$

$$= 0.57$$

Bridge Member rating = 36*0.57

= 20.52 tons

= 41,040 lb.

R.F. For HS-20 (Operating level): **(Interior girder-B)**

$$RF = \frac{C - A1XDL}{A2X(LL + IM)}$$

$$= \frac{1285 - 1.3 * 411.29}{1.3 * 606}$$

$$= 0.95$$

Bridge Member rating = 36*0.95

= 28.8 tons

=68,400 lb.

R.F. For HS-20 (Inventory level): **(Interior girder-C)**

$$RF = \frac{C - A1XDL}{A2X(LL + IM)}$$

$$= \frac{1285 - 1.3 * 411.29}{2.17 * 397}$$

$$= 0.87$$

Bridge Member rating = 36*0.87

= 31.32 tons

= 62,640 lb.

R.F. For HS-20 (Operating level): **(Interior girder-C)**

$$RF = \frac{C - A1XDL}{A2X(LL + IM)}$$

$$= \frac{1285 - 1.3 * 411.29}{1.3 * 397}$$

$$= 1.45$$

Bridge Member rating = 36*1.45

= 52.2 tons

=104,400 lb.

R.F. For HS-20 (Inventory level): **(Exterior girder-D)**

$$RF = \frac{C - A1XDL}{A2X(LL + IM)}$$

$$= \frac{1285 - 1.3 * 411.29}{2.17 * 427}$$

$$= 0.81$$

Bridge Member rating = 36*0.81

= 29.16 tons

= 58,320 lb.

R.F. For HS-20 (Operating level): **(Exterior girder-D)**

$$RF = \frac{C - A1XDL}{A2X(LL + IM)}$$

$$= \frac{1285 - 1.3 * 411.29}{1.3 * 427}$$

$$= 1.35$$

Bridge Member rating = 36*1.35

= 48.6 tons

=97,200 lb.

Appendix D

Prestress force calculation

DL = 332 k-ft.

LL = 690.37 k-ft.

Allowable tensile stress at steel F_t = 0.55*33 = 18 ksi

Allowable compressive stress at steel F_b = 0.55*33 = 18 ksi

Stress at the bottom of the girder

$\sigma = \frac{Mc}{I} = \frac{(332+690)*12*16.5}{6710}$ = 30 ksi

Over stress at positive zone, σ_{over} = 30 – 18 = 12 ksi

$\sigma_b = \frac{P_e}{A} + \frac{P_e*e*y}{I}$

$12 = \frac{P_e}{38.3} + \frac{P_e*12.65*16.5}{6170}$

P_e = 205 k

With 8% prestress loss P_e = 205*1.08 = 220 k

Normal prestress 220 k

0.5 inch dia

$\frac{220}{0.153}$ = 1437 ksi

$\frac{1437}{220}$(after loss) = 7

0.6 inch dia

$\frac{220}{0.217}$ = 1013 ksi

$\frac{1013}{220}$ = 5

CFCC

$\frac{220}{1.17}$ = 188 ksi

$\frac{188}{205}$ = 0.9 [2]

Appendix E

Cost Analysis for Different Retrofitting Options:

All these expenses are based on the Texas Department of Transportation's Average Low Bid Unit Prices as of September 2021, as well as TxDOT's Standard Specifications for the Construction and Maintenance of Highways, Streets, and Bridges, 2014.)

Deck Retrofitting

i) Removing of 2.5 in. concrete and replacement with fresh concrete:

According to Item 429 **"Concrete Structure Repair"** includes remove and repair of unsound, delaminated or spalled concrete. Materials specifications, construction methods are discussed in the TxDOT, 2014. The measurement of the repair is square foot in place in case of bridge deck repair.

"*This price is full compensation for furnishing, placing, and curing all repair materials; removing concrete; saw-cutting; cleaning reinforcing steel; supplying and installing replacement or supplemental reinforcing steel, drive pins, studs, or expansion bolts; and equipment, labor, and incidentals."*

Item Cost: Statewide Maximum: $118/SF. (Average low bid Price Excel)

For St. Francis NB Bridge (Spans 1, 2, and 3 only):

Total amount of concrete to be removed = (160*22) SF

= 3520 SF =392 SY

Gross Cost = (3520*118) = **$ 4,15,360**

Traffic Closure Cost:

Cost= $ 500/hour (Include freeway + normal lane closure)

Removing concrete pavement= 2000 SY/day

Concrete overlay= 300 SY/day

Number of days for removing concrete= 392/2000= 0.2 day= 5 hours

Number of days for overlay casting= 392/300= 1.3 days= 32 hours

Total number of hours= 37 hours

Total cost for lane closure= 37*500 = $18,500

Total Cost=$ 4,15,360 + $ 18,500 = $ 4,33,860

ii) CFRP Underneath the concrete

According to Item 786 "Carbon Fiber Reinforced Polymer (CFRP)" includes furnish and installation of CFRP in case of protecting or strengthening concrete member. Materials, work method are provided in TxDOT, 2014.

"This price is full compensation for all materials, labor, equipment, pull-off testing (including repair of test sites), manufacturer's supervision, and related work necessary to prepare the surface of the concrete, to install the CFRP system as detailed on the plans and apply the protective appearance coat."

Item Cost: Statewide Maximum: $ 45/SF.

For St. Francis NB Bridge (Spans 1, 2, and 3 only):

Total amount of concrete to be removed = (160*22) SF

= 3520 SF =392 SY

Assuming 70% of the deck area will be retrofitted.

Gross Cost = (0.7*3520*45) = **$ 1,10,880**

Traffic Closure Cost:

Cost= $ 1000/hour (Include freeway + normal lane closure)

Time to install CFRP= 70 hrs

Total cost for lane closure= 70*1000= $70000

Total Cost=$ 1,10,880+ $ 70000 = $ 180,880

iii) Installation of steel joist:

According to Item 442 “Metal for structures” includes structural steel, high-strength bolt, or other metals used in structures. Materials specification, work method/procedure are provided in TxDOT, 2014.

“The work performed and materials furnished in accordance with this Item and measured as provided under “Measurement” will be paid for at the unit price bid for “Structural Steel” of the type (Rolled Beam, Plate Girder, Tub Girder, Box Girder, Railroad Through-Girder, Railroad Deck-Girder, Miscellaneous Bridge, Miscellaneous Non-Bridge) specified. This price is full compensation for materials, fabrication, transportation, erection, paint, painting, galvanizing, equipment, tools, labor, and incidental.”

Item Cost: Statewide Maximum: $ 25/lb

Total Wt. of steel required=12000 lb

Cost= 12000*25 = **$3,00,000**

Joist installation labor cost:

Labor cost: 120 hr *125 (from net)**= $ 15000**

Traffic Closure Cost:

Cost= $ 1000/hour (Include freeway + normal lane closure)

Time to install CFRP= 120 hrs

Total cost for lane closure= 120*1000 = $120,000

Total Cost=$ 3,00,000+ $ 120,000+ $ 15000= $ 435,000

iv) Installation of FRP joist

Item 442 “Metal for structures” was followed to determine the Cost.

Item Cost: Statewide Maximum: $ 30/lb

Total Wt. of steel required=4128 lb

Cost= 4128*28 = **$1,23,840**

(Include all the weight of bolts and steel joist)

Joist installation labor cost:

Labor cost: 120 hr *125 (from net)**= $ 15000**

Traffic Closure Cost:

Cost= $ 1000/hour (Include freeway + normal lane closure)

Time to install CFRP= 120 hrs

Total cost for lane closure= 120*1000 = $120000

Total Cost=$ 123,840+ $ 120,000+ $ 15000 = $ 258,840

Girder Retrofitting

i) Installation of CFRP laminate underneath Girder

According to Item 786 “Carbon Fiber Reinforced Polymer (CFRP)” includes furnish and installation of CFRP in case of protecting or strengthening concrete member. Materials, work method are provided in TxDOT, 2014.

“This price is full compensation for all materials, labor, equipment, pull-off testing (including repair of test sites), manufacturer’s supervision, and related work necessary to prepare the surface of the concrete, to install the CFRP system as detailed on the plans and apply the protective appearance coat.”

Item Cost: Statewide Maximum: $ 45/SF.

For St. Francis NB Bridge (Spans 1, 2, and 3 only):

Total amount = 160*4*(11.5/12)*2 SF

= 1226 SF

Gross Cost = (1226*45) = **$ 55,200**

Traffic Closure Cost:

Cost= $ 1000/hour (Include freeway + normal lane closure)

Time to install CFRP= 40 hrs

Total cost for lane closure= 50*1000 = $50,000

Total Cost=$ 55,200+ $ 50,000 = $ 105,200

ii) Post-tensioning of steel girders:

Incase of posttensioning of girders approximate cost assumed based on FHWA/IN/JTRP Final report (2000).

Posttensioning tendon= **$ 6000**

Jacking Station = 5000*8= **$40000**

Structural steel = 250 lb* 28=**$7000**

Welding station labour **=** 15 hr*125 **=$ 1875**

Jacking Labor = 33 *150 = **$ 5000**

Traffic Clouser: (All four Lane 10,000/hr)

Total Cost: 25 hr *10000 =**$ 250000**

Total Cost = **$ 6000+$40000 +$7000 +$ 5000+$ 1875+ $ 250000= $309875**

Bridge Retrofitting:

i) Shear connector on the girder line and recasting of concrete:

According to Item 429 **"Concrete Structure Repair"** includes remove and repair of unsound, delaminated or spalled concrete. Materials specifications, construction methods are discussed in the TxDOT, 2014. The measurement of the repair is square foot in place in case of bridge deck repair.

"*This price is full compensation for furnishing, placing, and curing all repair materials; removing concrete; saw-cutting; cleaning reinforcing steel; supplying and installing replacement or supplemental reinforcing steel, drive pins, studs, or expansion bolts; and equipment, labor, and incidentals."*

Item Cost: Statewide Maximum: $118/SF. (Average low bid Price Excel)

For St. Francis NB Bridge (Spans 1, 2, and 3 only):

Total amount of concrete to be removed = (160*11.5/12*4) SF

= 520 SF =58SY

Gross Cost = (58*118) = **$ 6844**

Total amount of steel required: 1514 lb

Steel cost =1514*4/lb= **$ 6056**

Labor cost: 200 hr *125 (from net)**= $ 25000**

Traffic closure:

Cost= $ 500/hour (Include freeway + normal lane closure)

Time to install connector and concrete layout= 250 hrs

Total cost for lane closure= 250*800 = **$200000**

Total cost= **$ 6844 + $ 6056 +$ 25000 +$200000 = $ 237,900**

ii) Shear connector on the plate and weld the plate to line and recasting of concrete:

According to Item 429 **"Concrete Structure Repair"** includes remove and repair of unsound, delaminated or spalled concrete. Materials specifications, construction methods are discussed in the TxDOT, 2014. The measurement of the repair is square foot in place in case of bridge deck repair.

"*This price is full compensation for furnishing, placing, and curing all repair materials; removing concrete; saw-cutting; cleaning reinforcing steel; supplying and installing replacement or supplemental reinforcing steel, drive pins, studs, or expansion bolts; and equipment, labor, and incidentals."*

Item Cost: Statewide Maximum: $118/SF. (Average low bid Price Excel)

For St. Francis NB Bridge (Spans 1, 2, and 3 only):

Total amount of concrete to be removed = (160*24/12*4) SF

= 12801 SF =142SY

Gross Cost = (142*118) = **$ 16756**

Total amount of steel required: 1514 lb +1500 lb

Steel cost =3014*4/lb= **$ 12056**

Labor cost: 250 hr *125 (from net)**= $ 31250**

Traffic closure:

Above St. Francis:

Cost= $ 400/hour (Include freeway + normal lane closure)

Time to install connector and concrete layout= 250 hrs

Total cost for lane closure= 250*800 = **$200000**

Below St Francis:

Cost= $ 1000/hour

Total hr for welding: 150

Total Cost: 100*1000 = **$ 100000**

Total cost= **$ 16756+ $ 12056$ + 31250+$200000 +$ 100000 = $ 360062**

References

1. AASHTO (2014). “AASHTO LRFD bridge design specification.” American Association of State Highway Transportation Officials.
2. ABAQUS (2014). “ABAQUS standard user’s manual. Version 6.14, vol. I–III.” Pawtucket(America): Hibbitt, Karlsson & Sorensen, Inc.
3. Agrawal, A. K., Xu, X., and Chen, Z. (2011). “Bridge-Vehicle Impact Assessment”, Report on Project # C-07-10, University Transportation Research Center – Region 2/New York State Department of Transportation.
4. Albraheemi, M., (2018). “Evaluation of Non-Composite Steel Girder Bridges Using Field Load Testing and a Calibrated Finite- Element Model.” M.S. Thesis., The University of Maine.
5. American Association of State Highway and Transportation Officials. (2016a). “Manual for Bridge Evaluation, 2nd Edition, with 2011, 2013, 2014, 2015, and 2016 Interim Revisions.” C3, Washington, DC.
6. American Association of State Highway and Transportation Officials. (2016a). “Manual for Bridge Evaluation, 2nd Edition, with 2011, 2013, 2014, 2015, and 2016 Interim Revisions.” C3, Washington, DC.
7. Angel, C. M., and Casas, J. R. (2000). “Testing of externally prestressed concrete beams.” Engineering Structures.
8. Arockiasamy, M., Sowrirajan, R., Shahawy, M., and Beitelman, T. E. (1995). “Repair of damaged pre-tensioned solid slab using CFRP laminates.” Nonmetallic (FRP) reinforcement for concrete structures, E & FN Spon, London, 492–500.

9. Bachiri. T., Khamlichi. A., and Bezzazi. M., (2107). “Detection of Rebar Corrosion in Bridge Deck using GPR.” METEC Web of Conferences, NDECS 2017.
10. Bagheri, A., Alipour, M., Osman, E. O., and Harris, K. D., (2018). “A Nondestructive Method for Load Rating of Bridges without Structural Properties and Plan.” Engg. Strictures 171 (2018) 545-556.
11. Barr, P. J., Eberhard, M. O., & Stanton, J. F. (2001). “Live-load distribution factors in prestressed concrete girder bridges.” Journal of Bridge Engineering, 6(5), 298-306.
12. Bradberry, T. E., & Wallace, S. (2003). FRP reinforced concrete in Texas
13. Breña, S. F., Jeffrey, A. E., and Civjan, S. A. (2012). Evaluation of a Non-composite Steel Girder Bridge through Live-load Field Testing. Journal of Bridge Engineering, 18(7), 690-699.
14. Carino, N. J. (2001). “The Impact-Echo Method: An Overview.” Structures Congress & Exposition 2001, Washington, D.C.: American Society of Civil Engineers.
15. Chajes, M. J. (2005). Using diagnostic load tests for accurate load rating of typical bridges. Bridge Structures, 2(1), 13-23.
16. Chajes, M. J., Mertz, D. R., and Commander, B. (1997). “Experimental load rating of a posted bridge.” Journal of Bridge Engineering, 2(1), 1-10.
17. Chung, W., and Sotelino, E. D. (2006). “Three-dimensional finite element modeling of composite girder bridges.” Eng. Struct., 28(1), 63–71.
18. Clark, M. R., McCann, D. M., and Forde, M. C. (2003). “Application of infrared thermography to the non-destructive testing of concrete and masonry bridges.” Ndt & E International, 36(4), 265-275.
19. Coding Guide, TxDOT, 2020.

20. Collin, P., Häggström, J. & Hällmark, R., 2015. International Workshop on Strengthening of Steel/Composite bridges, Lulea: Lulea University of Technology.
21. Concrete Bridges. Special Publication, 277, 39-57.
22. Cousins, E.T., and Harris, K. D. (2009). “Use of a sandwich plate system in a Virginia bridge.” Contract Report.
23. DeWolf, J. T. (2009). “History of Connecticut’s short-term strain program for evaluation of steel bridges.” Rep. No. CT-2251-F-09-6, Connecticut DOT, Hartford, CT
24. Dicleli, M. and Erhan, S. (2009). “Live load distribution formulas for single-span prestressed concrete integral abutment bridge girders.” J. Bridge Eng., 14(6), 472–486 31.
25. Durgesh C. Rai., Srinaganjaneyulu, K., and Tripti, P. (2013) “Strengthening of Slab Action in Transverse Direction of Damaged Deck of Prestressed Box Girder Bridge.” ASCE
26. Erki, M. A., and Heffernan, P. J. (1995). “Reinforced concrete slabs externally strengthened with fiber-reinforced plastic materials.” Nonmetallic (FRP) reinforcement for concrete structures, E & FN Spon, London, 509–516.
27. FHWA (Federal Highway Administration). (2012). Bridge inspector’s reference manual, Washington, DC
28. Freitas, S. T. D., Kolstein, H., and Bijlaard, F. (2-10).” Sandwich system for renovation of orthotropic steel bridge decks.” Journal of Sandwich Structures and Materials.
29. Gheitasi, A., & Harris, D. K. (2014). “Overload flexural distribution behavior of composite steel girder bridges.” Journal of Bridge Engineering, 20(5), 04014076.

30. Gucunski, N., Slabaugh, G. G., Wang, Z., Fang, T., and Maher, A. (2008). “Impact echo data from bridge deck testing: Visualization and interpretation. Transportation Research Record (2050).”, pp. 111-121. doi: 10.3141/2050-11.
31. Guthrie. W. S., Larsen. L. J., Baxter. S. J., and Mazzeo. A. Brian., (2019). “Automated Air Coupled Impact echo Testing of a concrete Bridge Deck from a continuously Moving Platform.” Journal of Nondestructive Evaluation.
32. Hasan, M. I., Yazdani, N. (2014). “Ground Penetrating Radar Utilization In Exploring Inadequate Concrete Covers In A New Bridge Deck.” Case Studies in Construction Materials, Elsevier. DOI: http://dx.doi.org/doi:10.1016/j.cscm.2014.04.003, Reference: CSCM 8.
33. Hasan, M. I., Yazdani, N. (2015). “Experimental Study for Quantitative Estimation of rebar Corrosion in Concrete Using Ground Penetrating Radar.” Hindawi Publishing Corporation, Journal of Engineering, Volume 2016, Article ID 8536850
34. Hodson, D., Barr, P., and Halling, M. (2012). “Live-load analysis of post-tensioned box girder bridges.” J. Bridge Eng., 17(4), 644–651
35. He, Y. L., Zhang, G. P., and Xue, J. P. (2014). “Finite element analysis on drilling of unidirectional carbon fiber reinforced plastic(CFRP).” Applied Mechanics and Materials, 455, 228–231.
36. Hugenschmidt, J., & Mastrangelo, R. (2006). “GPR inspection of concrete bridges.” Cement and Concrete Composites, 28(4), 384-392.
37. Ichimasu, H., Maruyama, M., Watanbe, H., and Hirose, T. (1993). “RC slabs strengthened by bonded carbon FRP plates: Part 1 Laboratory study.” Fiber-Reinforced-

Plastic Reinforcement for Concrete Construction: International Symposium, American Concrete Institute, Detroit,

38. Infrastructure Report Card, American Society for Civil Engineers (ASCE), 2017
39. Kee, S. H., Oh, T., Popvics, J. S., Arndt, R. W., Zhu, J. (2012). "Nondestructive Bridge Deck Testing with Air-Coupled Impact-Echo and Infrared Thermography." Journal of Bridge Engineering, 17 (6): 928-939, ASCE, DOI: 10.1061/(ASCE) BE.1943-5592.000350.
40. Krauser, L.(2006). Repair, modification, and strengthening with post-tensioning. PTI journal, 4(1), 24-40.
41. Kwon, G., Engelhardt, M. D. & Klingner, R. E., 2009. Implementation Project: Strengthening of a Bridge near Hondo, Texas using Post-Installed Shear Connectors, Austin, Texas: The University of Texas at Austin
42. Lichtenstein, G. A., (1994). "Bridge Rating Through Nondestructive Load Testing." NCHRP 12-28 (13) A, Transportation Research Board (TRB)
43. Mertz, D., and Gillespie, J., "Rehabilitation of steel bridges through the application of advanced composite materials", NCHRP 93-ID 11, TRB, Washington, D.C.
44. Miller, C. T., and Chajes, M. J. (2001)." Strengthening of a Steel Bridge Girder Using CFRP Plates." Journal of bridge engineering.
45. Moore, M., Phares, B. M., Graybeal, B., Rolander, D., & Washer, G. (2001). "Reliability of visual inspection for highway bridges," volume I (No. FHWA-RD-01-020,).
46. Mosallam, A. S., and Mosalam, K. M. _2003_. "Strengthening of two-way concrete slabs with FRP composite laminates." Construction and building materials, Vol. 17, Elsevier Science Ltd., Amsterdam, The Netherlands, 43–54.

47. Nanni, A. (1995). “Concrete repair with externally bonded FRP reinforcement.” Concr. Int., 17(6), 22–26.
48. Omar. T., Nehdi. L. M., and Zayed. T., (2017). “Rational Condition Assessment of RC Bridge Decks Subjected to Corrosion-Induced Delamination.” Journal of Materials in Civil Engineering, ASCE.
49. P, Joy., (2008). “Finite Element Analysis of Carbon FiberComposite Ripping Using ABAQUS.” M. S., Thesis paper, Clemson University.
50. Petrou. F. M., Parlker. D., Harries. A. Kent., and Rizos. C. D. (2008). “Strengthening of Reinforced Concrete Bridge Decks Using Carbon Fiber-Reinforced Polymer Composite Materials.” Journal of Bridge Engineering, ASCE, Vol-13, No-5
51. Post-Tensioned Box Girder Design Manual, Federal Highway Administration, U.S. Department of Transportation, 2016.
52. Raju, R. K., Hasan, I., Yazdani, N. (2018). “Quantitative Relationship Involving Reinforcing Bar Corrosion and Ground-Penetrating Radar Amplitude.” ACI Materials Journal 115 (3), DOI: 10.14359/51702187.
53. Reed, M. W., Barnes, R. W., Schindler, A. K., and Lee, H. (2005). Fiber Reinforced Polymer Strengthening of Concrete Bridges that Remain Open to Traffic. ACI Structural Journal, vol. 102, no. 6, pp. 823-831.
54. Salama, T., and Meguid, A. A. (2010). “Strengthening Steel Bridge Girders Using CFRP.” A report presented by the University Transportation Center for Alabama.
55. Sanayei, M., Reiff, J. A., Brenner, R. B., and Imbaro, R. G., (2015). “Load Rating of a Fully Instrumented Bridge: Comparison of LRFR Approaches.” Journal of performance constriction and facilities, ASCE.

56. Sanayei, M., Phelps, J., Sipple, J., Bell, E., and Brenner, B. (2012). “Instrumentation, nondestructive testing, and finite-element model up-dating for bridge evaluation using strain measurements.” J. Bridge Eng., 10.1061/(ASCE)BE.1943-5592.0000228
57. Schiebel, S., Parretti, R., Nanni, A., and Huck, M. (2002). “Strengthening and load testing of three bridges in Boone County, Missouri.” Pract. Period. Struct. Des. Constr., 10.1061/(ASCE)1084-0680(2002)7: 4(156), 156–163.
58. Scherr, J. F., and Grosse, C. U. (2020). “Delamination detection on a concrete bridge deck using impact echo scanning.” Structural Concrete, (October), 1–7.
59. Schulz, J. L. (1993). “In search of better load ratings.” Civil Engineering, 63(9), 62.
60. Seim, W., Horman, M., Karbhari, V., and Seible, F. (2001). “External FRP post strengthening of scaled concrete slabs.” J. Compos. Constr., 5(2), 67–75.
61. Sen, R., Liby, L., and Mullins, G. (2001) “Strengthening steel bridge sections using CFRP laminates.” Composites Part B: Engineering, Elsevier publisher, UK, 32(4), 309-322.
62. Shaat, A., Schnerch, D., Fam, A., and Rizkalla, S. (2004), “Retrofit of steel structures using Fiber-Reinforced Polymers (FRP): State-of-the-art.” Transportation Research Board (TRB) Annual Meeting, Washington, CD-ROM (04-4063).
63. Sheikh, S. A. (2002). “Performance of concrete structures retrofitted with fiber reinforced polymers.” Engineering structures, Vol. 24, Elsevier Science Ltd., Amsterdam, The Netherlands, 869–879.
64. Stallings, J. M., & Yoo, C. H. (1993). Tests and ratings of short-span steel bridges. Journal of Structural Engineering, 119(7), 2150-2168

65. Standard Specifications for Construction and Maintenance of Highways, Streets, and Bridges, TxDOT, 2014.
66. Taoum, A., and Jiao, H. (2015). "Damien Holloway Upgrading steel I-beams using local post-tensioning." Journal of Constructional Steel Research, (113), 127-134, Elsevier Science Ltd.
67. Tavakkolizadeh, M., and Saasatmanesh, H. (2003). "Strengthening of steel-concrete composite girders using carbon fiber reinforced polymer sheets", Journal of Structural Engineering, ASTM.
68. Terry J. Wipf, Brent M. Phares, F. Wayne Klaiber, and Yoon-Si Lee. (2003). " Evaluation of Post-tension Strengthened Steel Girder Bridge Using FRP Bars. CTRE Project 01-99, Iowa State University.
69. TxDOT Bridge Inspection Manual (2020)
70. Transportation past, present, future. Special Publication, 215, 3-36.
71. Use of Ultra-High-Performance Concrete for Bridge Deck Overlays. Final Report 2018, Bridge engineering center.
72. Waal D. L., Cork. R., Foote, J., Nguyen, V. T., and Fernando, D. (2017). " FRP strengthening of 60 Years Old Pre-Stressed Concrete Bridge Deck Units." Engineering Structures (143), 346-357, Elsevier Science Ltd.
73. Wiwatrojanagul, P., Sahamitmongkol, R., Tangtermsirikul, S., and Khamsemanan, N. (2017). "A new method to determine locations of rebars and estimate cover thickness of RC structures using GPR data." Construction and Building Materials, Elsevier Ltd, 140, 257–273.
74. Yang, D., Merrill, B. D., & Bradberry, T. E. (2011). Texas' Use of CFRP to Repair

75. Yost, J. R., Schulz, J. L., & Commander, B. C. (2005). “Using NDT data for finite element model calibration and load rating of bridges.” In Structures Congress 2005: Metropolis and Beyond (pp. 1-9).

76. Yost, J. R., Schulz, J. L., & Commander, B. C. (2005). “Using NDT data for finite element model calibration and load rating of bridges.” In Structures Congress 2005: Metropolis and Beyond (pp.1-9).

77. Yousif, Z., & Hindi, R. (2007). “AASHTO-LRFD live load distribution for beam-and-slab bridges: Limitations and applicability.” Journal of Bridge Engineering, 12(6), 765-773.

78. Zaki, A., Johari, M. A. M., Hussin, W. M. A. W., Jusman, Y. (2018). “Experimental Assessment of Rebar Corrosion in Concrete Using Ground Penetrating Radar (GPR).” Hindawi, International Journal of Corrosion, Volume 2018, Article ID 5389829.

79. Zhang, Z., & Aktan, A. E. (1997). “Different levels of modeling for the purpose of bridge evaluation.” Applied Acoustics, 50(3), 189-204.